BIOCHEMICAL AND STRUCTURAL STUDIES OF BECLIN2 IN AUTOPHAGY REGULATION AND GPCR SIGNALING

QIU XIANXIU

Ph.D

THE HONG KONG POLYTECHNIC UNIVERSITY

2017

The Hong Kong Polytechnic University

Department of Applied Biology and Chemical Technology

Biochemical and Structural Studies of Beclin2 in Autophagy Regulation and GPCR Signaling

Qiu Xianxiu

A thesis submitted in partial fulfilment of the requirements

for the degree of

Doctor of Philosophy

Nov. 2017

CERTIFICATE OF ORIGINALITY

I hereby declare that this thesis is my own work and that, to the best of my knowledge and belief, it reproduces no material previously published or written, nor material that has been accepted for the award of any other degree or diploma, except where due acknowledgement has been made in the text.

_____ (Signed)

QIU Xianxiu (Name of student)

Abstract

Autophagy is an evolutionarily conserved cellular catabolic process that plays a critical role in maintaining cellular homeostasis through lysosomal degradation of aged or dysfunctional cytoplasmic materials. A recent study reveals that Beclin2, a novel homolog of Beclin1 in mammals, plays a dual role in autophagy modulation and lysosomal sorting of GPCR. Similar to Beclin1, Beclin2 acts as an essential autophagy regulator by interacting with a variety of autophagy-related proteins such as Atg14L and UVRAG. Additionally, via its interaction with GASP1, Beclin2 modulates the lysosomal degradation of a subset of GPCRs in an ubiquitination-independent pathway. However, the molecular mechanism underlying this dual action of Beclin2 in autophagy modulation and GPCR degradation remains unclear.

In this study, recombinant human Beclin2 was cloned from the human cDNA library, and expressed in *Esherichia coli*. We conducted biochemical characterization to confirm that the coiled coil domain of Beclin2 is a metastable homodimer and functionally inactive. In a similar manner to Beclin1, Beclin2 homodimer can bind to autophagy enhancers like Atg14L or UVRAG via their respective coiled coil domains and convert to the more stable and functionally active Beclin2-Atg14L or Beclin2-UVRAG heterodimer.

We determined the structure of Beclin2 coiled coil domain at 2.2 Å resolution

by x-ray crystallography. The structure reveals an anti-parallel coiled coil homodimer with multiple “perfect” hydrophobic pairings at the dimer interface to stabilize the dimeric structure. However, there are also several “imperfect” pairings at the dimer interface involving polar or charged residues. Similar to Beclin1, these “imperfect” pairings render the Beclin2 coiled coil homodimer metastable.

Comparison between Beclin1 and Beclin2 coiled coil regions for Atg14L/UVRAG bindings reveals that Atg14L is the preferred binding partner for Beclin2 while UVRAG is preferred by Beclin1. The structure of Beclin2-Atg14L complex was solved at 2.5 Å resolution via x-ray crystallography, which reveals a parallel coiled coil heterodimer. This heterodimer retains the canonical hydrophobic pairings and gains additional stabilizing interactions at the interface, thus render it notably stable compared with Beclin2 homodimer. In addition, structure-based mutations were generated to further delineate molecular determinants involved in Beclin2-Atg14L complex formation.

Furthermore, we also evaluate the potency of Beclin2 in modulating the endosomal trafficking of D2 dopamine receptor (D2R). Recombinant human Beclin2 N-terminus and GASP1 C-terminus were purified individually, followed by interaction investigation by a variety of assays. Our current *in vitro* data did not observe direct association between Beclin2 and GASP1, however, we indeed find that Beclin2 variants, and Beclin2-targeting peptides, exert a functional role in mediating D2R

degradation. Further work is required to investigate its underlying molecular machinery.

In summary, by focusing on biochemical and structural studies of Beclin2 coiled coil domain and Beclin2-Atg14L assembly, these findings presented in this thesis provide valuable clues to elucidate the molecular mechanism underlying the role of Beclin2 in autophagy regulation. In addition, the biochemical studies on Beclin2-GASP1 interactions also provide insights to understand the dual action of Beclin2 in autophagy and GPCR trafficking.

Acknowledgements

I would like to express my sincere thankfulness to my supervisor Prof. Zhao Yanxiang. Without her guidance and help, the work involved in this thesis would not be possible. I also thank her for offering such a great opportunity for developing this career, for teaching and trusting me in work, and for positively encouraging me whenever difficulties occurred.

I would also thank all examiners and research committee members, Prof. Hao Quan and Dr. Yue Jianbo in particular, for their kind assistance, support and constructive suggestions.

I thank all lab members in Prof. Zhao's group, for their support and help. Ph.D life is never easy, but they certainly bring a lot of fun in it. Thanks Dr. Li Xiaohua, who welcome me into the laboratory, guided me the protein biochemical and crystallographic studies. Her work also laid the foundation for this thesis. Thanks Dr. Pan Xuehua for being generous in sharing his experience and knowledge of crystallographic theory and data processing; I would also thanks Dr. He Yunjiao, whose work is complementary to my own, and made a contribution to this work; thanks Dr. Wu Shuai for the collaboration work on stapled peptides project, and his help in cell biology studies; I received much assistance and supports from Miss Li Na, Miss Zhang Xiaozhe, and Miss Yang Xian throughout these years. I am very grateful

for their efforts. I would also like to express my thankfulness to all the former members in the lab.

I must express my appreciation to Dr. He Congcong in Northwestern University, for being extremely generous with her time and knowledge, supplying us cell lines and plasmids, and sharing valuable experience and information. I also thank Dr. Altea Rocchi and Dr. Soh Yamamoto for their advice on cell biology experiments.

I also thank the Shanghai Synchrotron Radiation Facility (SSRF) for crystallographic data collection, and CCP4 Crystallography School and Workshop (Guangzhou, 2017) for providing constructive advice for structure solution.

I would like to thank my dear late father, a wonderful daddy and an amazing role model, who gave me strength and offered opportunity for me to walk through doors and pursue my dream. I must thank profusely my lovely family members, my dear mother, sisters and brother, for their endless support and encouragement throughout these years. I must also express my deepest gratitude to my husband, Mr. Li Tao, who always inspires and fully supports me to realize my goals and aspirations.

Table of Contents

Certificate of originality I

Abstract II

Acknowledgements V

Abbreviations ..... - 1 -

List of Figures ..... - 3 -

List of Tables ..... - 11 -

Chapter One: Introduction ..... - 12 -

1.1 Autophagy: Molecular Machinery and Physiological Functions ..... - 12 -

1.1.1 Autophagy in physiology and pathophysiology ..... - 12 -

1.1.2 The regulatory molecular machinery of autophagy ..... - 15 -

1.2 The Beclin1-Vps34 Complexes in Autophagy Regulation ..... - 22 -

1.2.1 Differential regulation of autophagic activity by distinct Beclin1-Vps34 complexes ..... - 22 -

1.2.2 Atg14L and UVRAG: two mutually exclusive subunits of Beclin1-Vps34 complexes ..... - 25 -

1.2.3 Architecture and flexibility of Beclin1-Vps34 complexes ..... - 27 -

1.3 Beclin2 is A Newly Identified Beclin1 Homolog ..... - 30 -

1.3.1 Beclin2 is a homolog of Beclin1 with notable distinctions .. - 30 -

1.3.2 Beclin2 is an autophagy modulator by forming Beclin2-Vps34 complexes ..... - 32 -

1.3.3 Beclin2 participates in the endolysosomal degradation process - 33 -

1.3.4 Beclin2 regulates GPCR degradation via interaction with GASP1 ..... - 34 -

1.4 The Objectives of This Study ..... - 38 -

Chapter Two: Methodology ..... - 40 -

2.1 Gene Cloning and Recombinant Protein Expression ..... - 40 -

2.1.1 Total RNA extraction ..... - 40 -

2.1.2 First strand cDNA synthesis ..... - 41 -

2.1.3 Plasmid construction ..... - 42 -

2.1.4 Transformation ..... - 45 -

2.1.5 Mutants or variants generation ..... - 45 -

2.1.6 Over-expression of recombinant proteins in E.coli ..... - 45 -

2.1.7 Selenomethionine substituted protein for phase determination

..... - 47 -

2.2 Purification ..... - 49 -

2.2.1 Affinity chromatography ..... - 49 -

2.2.2 Protease digestion ..... - 49 -

2.2.3 Poly-histidine tag and fusion partner removal ..... - 50 -

2.2.4 Size Exclusion chromatography ..... - 50 -

2.2.5 Concentration determination ..... - 50 -

2.2.6 Protein storage ..... - 51 -

2.3 Biophysical and Biochemical Analysis ..... - 52 -

2.3.1 Mass spectroscopy ..... - 52 -

2.3.2 Light scattering ..... - 52 -

2.3.3 Circular dichroism spectroscopy ..... - 53 -

2.3.4 Isothermal titration calorimetry ..... - 54 -

2.3.5 Peptide array chip ..... - 56 -

2.4 Cell-based Experiments ..... - 57 -

2.4.1 Cell culturing ..... - 57 -

2.4.2 Immunoprecipitation ..... - 57 -

2.4.3 Mass spectrometry-based interactome analysis ..... - 58 -

2.4.4 Biotin protection degradation assay ..... - 58 -

2.5 Structure Determination by X-ray Crystallography ..... - 60 -

2.5.1 Crystallization trials ..... - 60 -

2.5.2 Data screening and dataset collection ..... - 61 -

2.5.3 Data processing ..... - 61 -

2.5.4 Phasing ..... - 62 -

2.5.5 Model building and refinement ..... - 63 -

2.6 The Overall Workflow of This Study ..... - 65 -

Chapter Three: Biochemical and Structural Studies of Beclin2 Coiled coil domain - 66 -

3.1 Overview ..... - 66 -

3.2 Experimental Results ..... - 67 -

3.2.1 Recombinant plasmid construction and expression of Beclin2 .. - 67 -

3.2.1.1 Gene cloning and construct engineering ..... - 67 -

3.2.1.2 Expression of Beclin2 CC domain ..... - 68 -

3.2.2 Purification of Beclin2 CC domain ..... - 68 -

3.2.3 Biochemical characterization of Beclin2 CC domain ..... - 70 -

3.2.3.1 Mass Spectrometric analysis ..... - 70 -

3.2.3.2 Beclin2 self-associates in vivo and the CC domain forms a homodimer ..... - 71 -

3.2.3.3 Beclin2 CC homodimer is metastable ..... - 73 -

3.2.4 Crystallization initial screening of Beclin2-CC ..... - 75 -

3.2.5 Optimization of Beclin2 CC constructs ..... - 78 -

3.2.6 Crystallographic studies of Beclin2 CC domain ..... - 81 -

3.2.7 Phase determination ..... - 81 -

3.2.8 Beclin2 coiled coil domain structure ..... - 88 -

3.2.9 Biochemical distinction between Beclin1 and Beclin2 coiled coil domain structures ..... - 93 -

Chapter Four: Biochemical Analysis of Beclin2-Atg14L Interaction ..... - 97 -

4.1 Overview ..... - 97 -

4.2 Experimental Results ..... - 99 -

4.2.1 Purification of Beclin1, Atg14L and UVRAG coiled coil regions .. - 99 -

4.2.2 Beclin2 interacts with Atg14L and UVRAG via coiled coil domain

.....- 100 -

4.2.3 Atg14L and UVRAG are two mutually exclusive binding partners of Beclin2.....- 104 -

4.2.4 The Beclin2-Atg14L interaction is the strongest among Beclin1/2-Atg14L/UVRAG interacting pairs.....- 106 -

4.2.5 Structural modeling of Beclin2-UVRAG coiled coil assembly.....- 109 -

4.2.6 Mapping the coiled coil segments most critical for the Beclin2-Atg14L interaction .....- 112 -

Chapter Five: Structural Investigation of the Beclin2-Atg14L Complex.....- 117 -

5.1 Overview .....- 117 -

5.2 Experimental Results .....- 119 -

5.2.1 Preliminary crystallization trials of Beclin2-Atg14L complex- 119 -

5.2.2 Construction of Beclin2 monomer mutant to circumvent the precipitation problem .....- 121 -

5.2.3 Optimization of Beclin2-CC1 and Atg14L complex for crystallization.....- 122 -

5.2.4 Incorporation of Atg14L mutants to stabilize the Beclin2-Atg14L assembly.....- 126 -

5.2.5 Crystallization of Beclin2-Atg14L complex ..... - 127 -

5.2.6 Beclin2 interacts with Atg14L to form a parallel coiled coil dimer ..... - 130 -

5.2.7 Structure-based mutations to delineate the molecular determinants that drive the formation of a Beclin2-Atg14L complex . - 137 -

Chapter Six: Biochemical and Functional Studies of Beclin2 in GPCR Signaling . - 142 -

6.1 Overview ..... - 142 -

6.2 Experimental Results ..... - 144 -

6.2.1 Expression and purification of GASP1 C-terminus ..... - 144 -

6.2.2 Optimization of GASP1 C-terminal construct..... - 145 -

6.2.3 Characterization of Beclin2-GASP1 interaction..... - 147 -

6.2.4 Mass spectrometry-based interactome analysis of Beclin2 N-terminus ..... - 150 -

6.2.5 Functional roles of Beclin2 in GPCR degradation..... - 152 -

6.2.6 Designed stapled peptides enhance endolysosomal degradation of GPCR..... - 155 -

Chapter Seven: Discussion and Future Studies..... - 163 -

Reference ..... - 170 -

Abbreviations

Atg	Autophagy-related gene
Atg14L	Atg14-like protein
β-ME	β-Mercaptoethanol
CCP4	Collaborative computational project, number 4
CD	Circular Dichroism
cDNA	Complementary DNA
Co-IP	Co-immunoprecipitation
bp	Base pair
D2R	Dopamine receptor D2
DLS	Dynamic light scattering
DTT	DL-Dithiothreitol
E. coli	*Esherichia coli*
GPCR	G-protein-coupled receptors
GST	Glutathione-S-transferase
HEK293	Human Embryonic Kidney 293 cell line
His_6	Hexahistidine
IPTG	Isopropyl-β-D thio- galactopyranoside
ITC	Isothermal Titration Calorimetry
KD/ KDa	Kilo Daltons

LB	Lysogeny broth
LC3	Microtubule-associated protein 1A/1B-light chain 3
LS	Light scattering
MALS	Multi-angle light scattering
mTOR	Mammalian target of rapamycin
Mw	Molecular weight
PCR	Polymerase chain reaction
PEG	Polyethylene glycol
PI3KC3	Class Ⅲ phosphatidylinositol 3-kinase
PMSF	Phenylmethanesulfonyl fluoride
SAD	Single-wavelength anomalous diffraction
SDS-PAGE	Sodium dodecyl sulfate polyacrylamide gel electrophoresis
SEC	Size exclusion chromatography
Sumo	Small ubiquitin-like modifier
Tris	Tris (hydroxymethyl) aminomethane
Trx	Thioredoxin
UV	Ultraviolet
UVRAG	UV radiation resistance associated gene
WT	Wild type

List of Figures

Figure 1.1 The autophagy process and its regulatory complexes.

Figure 1.2 The “primary” or “secondary” interactors of Beclin1-Vps34 complex.

Figure 1.3 Schematic model of the constitution and architecture of the PI3KC3 complexes.

Figure 1.4 The schematic diagrams of domain structures of Beclin1 and Beclin2.

Figure 1.5 Multiple sequence alignment of Beclin2 and Beclin1 using Clustal.

Figure 1.6 Schematic illustrating the dual action of Beclin2 in mediating autophagy and the lysosomal sorting of GPCRs.

Figure 2.1 Illustration of the result of a typical ITC experiment.

Figure 2.2 A schematic diagram of the peptide array chip scanning through Beclin2 residues 1-105.

Figure 2.3 The schematic of the biotin protection degradation assay used to assess trafficking of flag-D2R in endosomes.

Figure 2.4 A schematic diagram of the workflow.

Figure 3.1 Total RNA extraction and PCR amplification of Beclin2 CC.

Figure 3.2 The purification and analysis of Beclin2 CC.

Figure 3.3 Mass spectrometric analysis of Beclin2 CC.

Figure 3.4 Co-immunoprecipitation and immunoblot analysis of protein lysates in Hela cells to detect Beclin2 self-association.

Figure 3.5 Molecular weight distributions of Beclin2 CC as determined in SEC-MALS.

Figure 3.6 Circular Dichroism (CD) spectra of the Beclin2 CC domain at different temperatures.

Figure 3.7 Determination of the Beclin2 CC self-dissociation by ITC assay.

Figure 3.8 Crystals of Beclin2 CC protein and their corresponding x-ray diffraction images.

Figure 3.9 SDS-PAGE of novel Beclin2 CC protein (residues 157-248) and its mutants.

Figure 3.10 Crystal of Beclin2 R243L protein and its corresponding x-ray diffraction image in Shanghai synchrotron.

Figure 3.11 SDS-PAGE of selenomethionyl Beclin2 CC mutants.

Figure 3.12 Crystals of selenomethionyl Beclin2 CC L236M mutant after initial crystallization screening.

Figure 3.13 Crystals of selenomethionyl Beclin2 L236M mutant and their diffraction patterns in Shanghai synchrotron.

Figure 3.14 The crystal structure of Beclin2 CC domain.

Figure 3.15 Helical wheel presentation of the 13 heptad repeats in Beclin2 coiled coil domain.

Figure 3.16 Atomic details of 13 a-d' pairings at the interface of Beclin2 homodimer.

Figure 3.17 Close-up view of the canonical and imperfect a - d' pairings in Beclin2 CC.

Figure 3.18 Determination of the mutual cross-association between Beclin1 CC and Beclin2 CC by ITC experiments.

Figure 3.19 Determination of the mutual cross-association between Beclin1 and Beclin2 by immunoprecipitation.

Figure 3.20 Comparison of the coiled coil interfaces of Beclin1 homodimer, Beclin2 homodimer and modelled Beclin1- Beclin2 heterodimer.

Figure 4.1 SDS-PAGE analysis for coiled coil fragments of Beclin1, Atg14L and UVRAG.

Figure 4.2 Determination of the interaction between Beclin2 CC and Atg14Ls2/UVRAG.

Figure 4.3 The interaction of Beclin2-Atg14L/UVRAG under high-salt conditions.

Figure 4.4 Competitive binding of Atg14Ls2 and UVRAG to Beclin2 CC.

Figure 4.5 Competitive binding of Beclin1 CC and Beclin2 CC to Atg14Ls2.

Figure 4.6 Competitive binding of Beclin1 CC and Beclin2 CC to UVRAG.

Figure 4.7 Helical wheels presentation of the heptad repeats in Beclin1-UVRAG complex.

Figure 4.8 The structural model of Beclin2-UVRAG complex and its close-up atomic details.

Figure 4.9 SDS-PAGE analysis of Atg14Ls2 protein degradation at different time intervals.

Figure 4.10 Schematic depicting Atg14L variants designed for examination of Beclin2 interaction.

Figure 4.11 The ITC profiles of Beclin2 CC titrated to Atg14L variants.

Figure 4.12 Competitive binding of Beclin1-3A and Beclin2 CC to Atg14L EGKVEKK.

Figure 5.1 Crystals obtained from the optimized crystallization conditions of Beclin2 CC and EGKVEKK mixture.

Figure 5.2 Purification, oligomer state, and interaction characterization of Beclin2-L225AL229A mutant.

Figure 5.3 Constructs designed to map the core region of Beclin2 CC domain responsible for Atg14L/UVRAG interaction.

Figure 5.4 ITC profiles for measuring the interactions between Atg14L and Beclin2 CC1-CC4.

Figure 5.5 ITC profiles for measuring the interactions between UVRAG and Beclin2 CC1-CC4.

Figure 5.6 ITC profiles for measuring the interactions of Atg14L EGKNSE and three Beclin2 CC1 fragments.

Figure 5.7 Schematic depicting Beclin2 CC1 and Atg14L complex constructs linked via GSx10 linker or cleavable protease 3C linker.

Figure 5.8 ITC profiles for measuring the interactions between Atg14L mutants and Beclin2 CC after imperfect residues at position “a” or “d” are replaced by leucine.

Figure 5.9 Mass spectrometric analysis of the Beclin2-Atg14L crystal sample.

Figure 5.10 Crystal of Beclin2-CC1 and Atg14L-EGKYSR-S116LG130L complex and its x-ray diffraction profile by in-house x-ray machine.

Figure 5.11 Crystal of Beclin2-CC1 and Atg14L-EGKYSR-S116LG130L complex and its x-ray diffraction profile in Shanghai synchrotron.

Figure 5.12 The crystal structure of Beclin2-Atg14L coiled coil assembly.

Figure 5.13 Close-up view of the hydrophobic and electrostatic pairings of Beclin2-Atg14L complex structure.

Figure 5.14 Comparison analysis of the dimeric interfaces of Beclin2 homodimer with the Beclin2-Atg14L and Beclin2-UVRAG heterodimers.

Figure 5.15 Schematic illustrating the mutation design within Beclin2 or Atg14L sequence.

Figure 5.16 ITC profiles for measuring the interactions between Beclin2 CC mutants and Atg14L.

Figure 5.17 ITC profiles for measuring the interactions between Atg14L mutants and Beclin2 CC.

Figure 5.18 Co-IP and immunoblot analysis to characterize the association between Beclin2 mutants and Atg14L in Hela cells.

Figure 5.19 Co-IP and immunoblot analysis to characterize the association between Atg14L mutants and Beclin2 in Hela cells.

Figure 6.1 SDS-PAGE analysis of the GASP1 (1000-1395) expression and purification.

Figure 6.2 Protein aggregate analysis of GASP1 (1000-1395) by SEC-MALS.

Figure 6.3 Characterization of GASP1-F1170K by SDS-PAGE and SEC-MALS analysis.

Figure 6.4 Determination of the interaction between Beclin2 NTF and GASP1-F1170K.

Figure 6.5 SDS-PAGE analysis of samples from pull-down assay.

Figure 6.6 Immunoblotting analysis of Beclin2 peptide array chip.

Figure 6.7 Coomassie-stained polyacrylamide gel of flag-Beclin2 wild type or flag-Beclin2-Δ69-88 deletion mutant immunoprecipitated samples.

Figure 6.8 Effects of indicated Beclin2 NTm plasmids transfection on biotin-mediated protection of flag-D2R after siRNA knockdown endogenous Beclin2 in HEK-D2R cells.

Figure 6.9 The computational model of SP4 binding to Beclin1.

Figure 6.10 Determination of the interaction between Tat-SP4 and Beclin2 CC.

Figure 6.11 Co-immunoprecipitation and immunoblot analysis of Beclin2 self-

association.

Figure 6.12 Effects of the indicated peptides on flag-D2R degradation in HEK-D2R cells.

Figure 6.13 Determination of the interaction between stapled peptides and Beclin2 CC.

Figure 6.14 Effects of the indicated peptides on flag-D2R degradation in HEK-D2R cells.

Figure 6.15 Effects of the indicated peptides with different concentration on flag-D2R degradation in HEK-D2R cells.

List of Tables

Table 3.1 Summary of the screened crystallization conditions for Beclin2 CC

Table 3.2 Summary of the new constructs design and rationale

Table 3.3 Crystallographic data processing and refinement statistics for Beclin2 CC

Table 4.1 Summary of Beclin1 CC, Atg14Ls2 and UVRAG constructs information.

Table 5.1 Trials towards the rational design of Beclin2-Atg14L constructs for crystallization.

Table 5.2 Crystallographic data processing and refinement statistics for Beclin2-Atg14L.

Table 6.1 Summary of the designed stapled peptides.

Chapter One: Introduction

1.1 Autophagy: Molecular Machinery and Physiological Functions

1.1.1 Autophagy in physiology and pathophysiology

Autophagy, derived from the Greek term for “self-eating”, is an evolutionarily conserved process that degrades cytoplasmic constituents by lysosome, and promotes survival against metabolic stresses in eukaryotic cells. There are three types of autophagic pathways in mammals, classified based on their distinct mechanisms on cargo sequestration. Chaperone-mediated autophagy (CMA) refers to a chaperone-dependent selective delivery pathway that cytosolic protein substrates are translocated cross the lysosomal membrane directly for degradation. Macroautophagy involves the formation of double-membrane vesicle termed autophagosome that engulfs cytosolic cargos for lysosomal degradation, while microautophagy delivers cytoplasmic constituents to lysosome by direct invagination of the lysosomal membrane (Galluzzi et al., 2017; Ohsumi, 2014). Among them, macroautophagy is the most prevailing type and also the most extensively studied. This thesis will mainly focus on macroautophagy, which is simply referred to as autophagy hereafter.

Autophagy has been implicated in a whole host of physiological and pathological cellular processes (Choi et al., 2013; Yang and Klionsky, 2010), ranging from metabolism and innate immunity to neurodegeneration and tumorigenesis suppression. Under homeostatic conditions, autophagy typically operates at low levels in cells and exerts housekeeping functions to remove long-lived proteins and damaged organelles. Under stress conditions such as hypoxia, nutrient deprivation, and pathogens infection, a portion of dysfunctional cytoplasmic components, or intracellular pathogens, are engulfed into the double-membrane autophagosome, and subsequently transported to lysosome for degradation. The resulting degraded products like amino acids are then recycled to sustain cellular metabolism (Mizushima and Komatsu, 2011). Through this process, autophagy plays important roles in protein and organelle quality control, whereas its dysfunction is associated with a wide range of pathophysiological processes such as aging, infection, neurodegenerative disorder and tumor (Levine and Kroemer, 2008).

Autophagy, as an essential homeostatic process, can be either beneficial or detrimental to human health. Such dual-natured role of autophagy is best manifested by the sophisticated roles autophagy play in cancer. At early stage, autophagy is generally regarded as a tumor suppressor mechanism because it helps to maintain cellular homeostasis and prevent malignant transformation. At late stage, autophagy can become beneficial for tumor growth and metastasis by enabling

efficient recycling of cellular nutrients to sustain cancer cell proliferation or to survive external stress such as oxygen and nutrient deprivation, chemotherapy, and radiotherapy (Cheng et al., 2013). Nonetheless, there is intense interest to target autophagy and autophagy-related proteins for potential treatment of diseases like diabetes, neurodegeneration and cancer. For example, hydroxychloroquine (HCQ), an autophagy inhibitor, is now undergoing several clinical trials to test its efficacy in cancer treatment (Manic et al., 2014). For majority of trials, HCQ is used in combination with existing therapies to treat refractory tumors. Clinical data are yet to be reported for these trials to testify the efficacy of this approach. In the cases of neurologic disorders or infection, autophagy activators have been shown to protect cells from the toxic impairment of aggregate-prone mutant proteins or pathogens through improving their clearance (Levine and Kroemer, 2008; Sarkar and Rubinsztein, 2008). These studies offer hope that autophagy may be a drug target for the almost intractable neurodegenerative diseases.

Although both *in vitro* cell models and *in vivo* animal models reveal that many autophagy modulators exert protective or detrimental effects on the pathogenesis of diseases, there are limited data of clinical studies. In addition, a number of key hurdles remain to be cleared before the application of autophagy regulators as therapeutics for diseases. First of all, the precise role of autophagy in physiological and pathological processes, and how the functional role of autophagy varies during

the progression of disease remain to be elucidated. Secondly, small molecules modulators that target autophagy with specificity and potency but cause little side effects or toxicity are not yet clinically available. Most currently developing autophagy modulators in clinical show neither directly nor specifically regulatory effects. For instance, chloroquine and hydroxychloroquine are actually lysosome inhibitors that negatively regulate autophagy by preventing the lysosome from degrading and recycling the enclosed cellular contents in the autophagosome (Chude and Amaravadi, 2017). While autophagy activators rapamycin and its analogues suppress mTOR function to positively modulate autophagy, they also induce alterations in various cellular processes that may cause potential side effects (Petibone et al., 2017). Furthermore, there is always the challenge to balance between the beneficial and detrimental effects of autophagy (promoting and impeding disease development). Therefore, further studies are urgently needed, especially mechanistic studies that may not only lead to more comprehensive understanding of the autophagy process, but also pave the way for the development of more specific and potent autophagy activators and inhibitors.

1.1.2 The regulatory molecular machinery of autophagy

Autophagy is a complicated, multiple-step process that operates in a tightly controlled and well-coordinated manner. This includes stress-induced signal transduction to regulatory proteins and lipids, the double-membrane

autophagosome assembly, the bulk cytoplasmic cargos sequestration, membrane expansion and fusion, and lysosomal degradation. For the purpose of discussion, the process can be roughly divided into five main phases: initiation, elongation, autophagosome completion, fusion and degradation. Each phase is controlled by specific autophagic regulatory factors.

As shown in Figure 1.1, autophagy initiates with an isolation membrane fragment termed phagophore. It is likely that autophagy is initiated at multiple phagophore assembly sites (PAS) in mammalian cells, which would form and dissolve when necessary (Hurley and Schulman, 2014). It is still unclear which regulatory factors constrain the phagophore size and shape. The exact source of the phagophore membrane is also unclear, although it is believed that various potential sources contribute in different phases (Ge et al., 2014; Suzuki and Ohsumi, 2010). Along with the phagophore expansion, impaired organelles, protein aggregates and invaded pathogens are sequestered in a relatively nonselective way. Subsequently, the closure of the growing edges of the phagophore forms a double-membrane autophagosome, followed by the fusion with lysosome for captured components digestion. There is also the possibility that an autophagosome fuses with an endosome before its docking with the lysosome (Mizushima and Komatsu, 2011). After lysosomal fusion, either directly or via endosomes, the content of autophagosomes is degraded by lysosomal enzymes. The resulting products like

nucleotides and amino acids are released back to cytoplasm for biosynthesis.

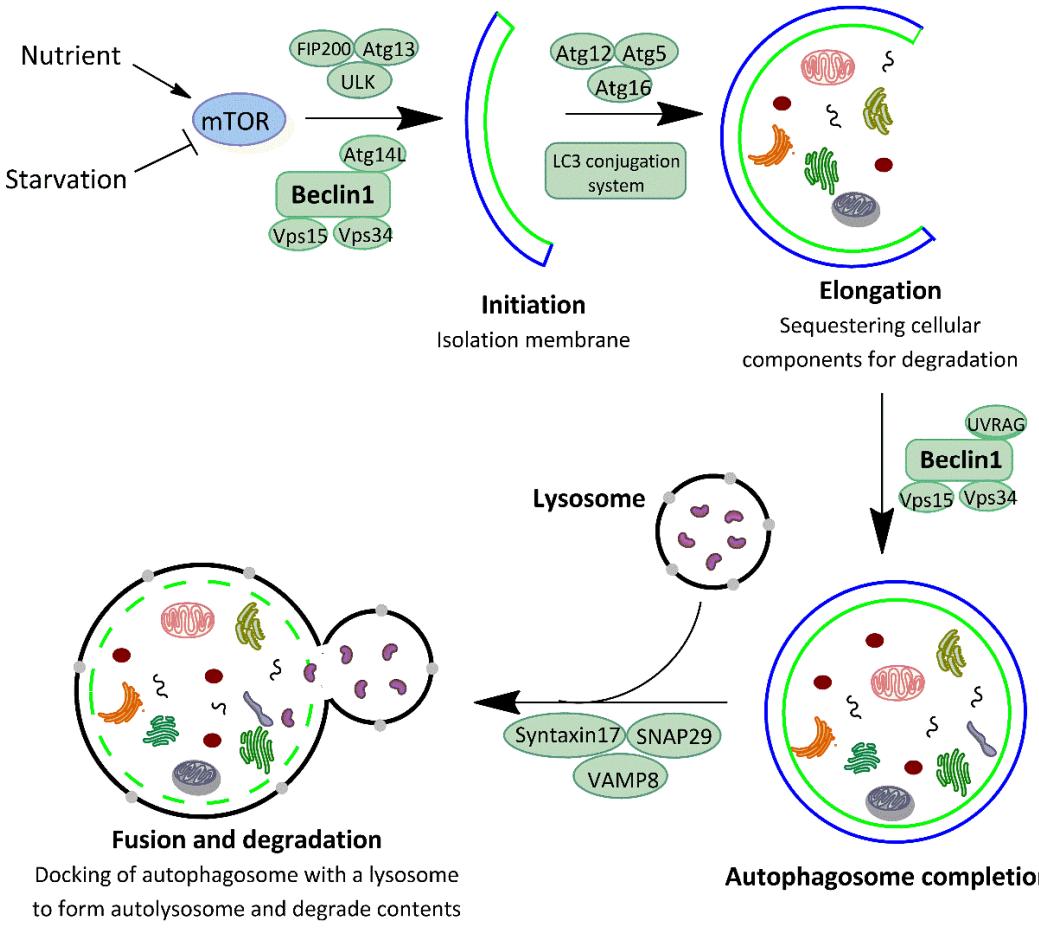

Figure 1.1 The autophagy process and its regulatory complexes. Briefly, autophagy is initiated with an isolation membrane and followed by the nucleation and expansion to form the autophagosome. Then the outer membrane of autophagosome docks with a lysosome to generate an autolysosome. This leads to digestion of the sequestered materials in the autophagosomes. mTOR: mammalian target of rapamycin; FIP200: focal adhesion kinase interacting protein of 200 kD; ULK1: Unc-51-Like Kinase 1; Atg: autophagy-related protein; Vps15, Vps34: vacuolar protein sorting 15 and 34; SNAP29: Synaptosomal-associated protein 29; VAMP8: vesicle-associated membrane protein 8.

Although the exact mechanism remains to be fully elucidated, our knowledge of the basic molecular machinery involved in autophagy has increased dramatically in these several decades. The core autophagy machinery relies on a number of autophagy-related proteins (Atgs) to precisely mediate successive steps of the autophagy process. To date, at least thirty-seven autophagy-related genes (ATGs) have been identified in yeast, and many of them are conserved in mammals (Ohsumi, 2014). In addition, extensive studies have been carried out to study the interaction or relationship among these proteins, and how they modulate the autophagy process. These studies have been summarized in several excellent review articles (Behrends et al., 2010; Feng et al., 2014; Mizushima et al., 2011).

The execution and regulation of autophagy is carried out by the large number of autophagy-related genes (ATGs) as well as other regulatory factors. These proteins usually form several functionally distinct complexes to promote the autophagic signaling cascade. Specifically, five regulatory complexes have been found to function in the autophagy process: the ULK1 complex containing the protein kinase ULK1 (Atg1 ortholog in mammals) and accessory subunits Atg13, Atg101, and FIP200 for the induction stage; the class Ⅲ phosphatidylinositol 3-kinase complex Ⅰ (PI3KC3-Ⅰ) containing the lipid kinase Vps34 and subunits Beclin1, Vps15, and Atg14L (Autophagy-related protein 14-like protein); two ubiquitin-like protein conjugation systems (Atg12-Atg5-Atg16 complex and Atg8/LC3 conjugation system), Atg9

transmembrane multi-protein complex, and the autophagic SNARE (soluble N-ethylmaleimide-sensitive factor attachment protein receptor) complex including Syntaxin 17, SNAP29, and VAMP8 (Antonioli et al., 2017).

The ULK1 complex is the most upstream signaling module in the autophagy process. It is directly activated by autophagy triggers such as stress signals at the phagophore assembly sites. This complex functions as the scaffold to recruit and phosphorylate downstream Atg assemblies for autophagy initiation (Karanasios et al., 2013). Then the Beclin1-Vps34 multiprotein complex is recruited to the phagophore assembly site to generate phosphatidylinositol 3-phosphates (PtdIns3P or PI3P) for double-membrane phagophore nucleation (Itakura and Mizushima, 2010; Matsunaga et al., 2010).

Two Atg conjugation systems are involved in the elongation of phagophore. The ubiquitin-like protein Atg12 is conjugated to its substrate Atg5 by Atg7 and Atg10, which acts like an E1 and E2 ubiquitin-activating enzyme, respectively. The resulting Atg12-Atg5 complex then binds with Atg16L non-covalently, forming a multimeric complex. The LC3 protein (mammalian Atg8 homolog), on the other hand, is conjugated to phosphotidylethanolamine (PE) located on the membrane, through the action of ATG7 and E2-like enzyme Atg3. The Atg12-Atg5-Atg16L complex then acts as an E3-like protein which facilitates the lipidation of LC3. Before lipidation, the cytosolic form of LC3 (referred as LC3-Ⅰ) is cleaved by the cysteine protease Atg4

(Slobodkin and Elazar, 2013). A conventional view is that these early Atg proteins, including the Atg12-Atg5-Atg16 ternary complex, would be released to cytosol when autophagosome is fully formed, while the lapidated LC3 (LC3-Ⅱ) persists on the membrane of autophagosome. Therefore, LC3-Ⅱ is well applied as a marker for autophagy studies.

The subsequent fusion between the mature autophagosomes and lysosomes depend on the SNARE complex. At this step, Syntaxin 17 on the outer membrane of mature autophagosomes interacts with SNAP29, and further mediates the fusion with lysosome by forming a ternary complex with VAMP8, a membrane protein located on lysosomes (Guo et al., 2014; Itakura et al., 2012). It is recently reported that Atg14L also functions in, beyond autophagosome biogenesis, the SNARE-mediated fusion of autophagosomes with lysosomes. Atg14L self-oligomerizes through its N-terminal cysteine rich segment, which is essential for its interaction with Syntaxin17-SNAP29 binary complex on the autophagosome, and further promotes membrane fusion of autophagosomes and lysosomes (Diao et al., 2015). This fusion-promoting effect of Atg14L is specific to autophagic SNAREs, and is Beclin1-Vps34 activity independent (Diao et al., 2015). It is also revealed that Atg14L directly binding to the helical structure of Syntaxin17 via its coiled coil domain, which is also responsible for Beclin1 interaction in forming the PI3KC3 complex Ⅰ. These data suggest Atg14L is involved in dynamic interactions with different binding

partners, generating distinct complexes to drive the autophagy process. However, the underlying molecular mechanism remains to be elucidated, and further biochemical and structural studies are required.

1.2 The Beclin1-Vps34 Complexes in Autophagy Regulation

1.2.1 Differential regulation of autophagic activity by distinct Beclin1-Vps34 complexes

Our lab has investigated the biochemical and structural properties of the mammalian Beclin1-Vps34 multiprotein complexes for many years. Identified as key players in the vacuolar protein sorting pathway firstly, Vps34 and Vps15 are also found to be essential for autophagy. Vps15 is a serine/threonine protein kinase that phosphorylates Vps34 and facilitates translocation of Vps34 to membranes. While Vps34 is a class Ⅲ phosphatidylinositol 3-kinase that synthesizes PI3Ps from phosphatidylinositol (PI) at the pre-autophagosomal structure (PAS), and further recruits Atg proteins for the phagophore expansion and subsequent autophagosome formation (Suzuki and Ohsumi, 2010). Emerging evidence suggests that the lipid kinase activity of Vps34 is one of the most essential elements for autophagosome biogenesis, and is regulated by several factors to modulate autophagic activity at various stages (Funderburk et al., 2010). This complex includes the core components Beclin1, Vps34, and Vps15, and is usually found in two biochemically and functionally distinct forms. The PI3KC3 complex Ⅰ refers to the subpopulation that contains Atg14L, the autophagy enhancer that binds to Beclin1 and is essential for autophagosome biogenesis. The PI3KC3 complex II, on the other hand, refers to the subpopulation that contains Beclin1-binding UVRAG instead of Atg14L. Complex II

plays critical roles in autophagosome maturation and endosomal pathway (Itakura et al., 2008; Thoresen et al., 2010).

Beclin1, an Atg6 ortholog in mammals, was firstly identified in 1998 from a yeast two-hybrid screening study to search for Bcl-2 binding partners (Liang et al., 1998). Initially defined as a tumor suppressor, Beclin1 acts as an important convergence point of autophagy and apoptosis (Liang et al., 1999). Biochemical and structural studies reveal that Beclin1 contains several distinct domains, including the disordered N-terminal region (NTR), a Bcl-2 homology-3 (BH3) domain, a flexible helical (FH) region, a coiled coil (CC) domain and the C-terminal β-sheet-α-helix repeated autophagy-specific (BARA) domain. All these fragments, the BH3 and CC domains in particular, interact with a host of regulatory molecules to modulate Vps34 activity and autophagy process. Specifically, previous studies have showed that its BH3 helix segment located on the N-terminal is essential for the interaction of Bcl-2 family members, which act as autophagy inhibitors by down-regulating the activity of the associated Beclin1-Vps34 complex (Sinha and Levine, 2008). BH3-only proteins or small molecule BH3 domain mimetics are able to compete with Beclin1 for binding to Bcl-2/ Bcl-XL, thereby liberating Beclin1 from Beclin1-Bcl-2/Bcl-XL complexes (Maiuri et al., 2007). Consequently, the autophagy pathway is activated by releasing Beclin1. The BARA domain on the C-terminal is evolutionary conserved and involved in lipid membrane binding (Huang et al., 2012). In terms of the CC domain, it is found

to be essential for the formation of two distinct PI3KC3 complexes through interactions with Atg14L and UVRAG (Itakura and Mizushima, 2009; Sun et al., 2009).

In addition to Atg14 and UVRAG, there are a variety of Beclin1-interacting Vps34 modulators (Figure 1.2). Conceptually, they could be regarded as “primary” or “secondary” interactors depending on the potency and specificity of their respective binding with Beclin1. Atg14 and UVRAG are classified as “primary” interactors due to their stable association with Beclin1 under physiological conditions. “Secondary” interactors, however, usually bind with the Beclin1-Vps34 complex in dynamic or transient manner (He and Levine, 2010). Some of them even depend on “primary” interactors to exert their modulatory effect. A plethora of recent studies have uncovered a variety of “secondary” modulators that collectively exert sophisticated regulation of the Beclin1-Vps34 complex in response to various cellular signals (Funderburk et al., 2010; He and Levine, 2010). For instance, Ambra1 (activating molecule in Beclin1-regulated autophagy) acts as a positive regulator of autophagy by switching its binding partner from Bcl-2 to the Atg14L-containing Beclin1-Vps34 complex to assist autophagy induction (Decuypere et al., 2012; Fimia et al., 2011; Matsunaga et al., 2009). Rubicon (RUN domain Beclin-1-interacting cysteine-rich-containing), on the contrary, exerts negative effect on autophagy and endolysosomal trafficking by associating with UVRAG to down-regulate the activity of UVRAG containing Beclin1-Vps34 complex (Matsunaga et al., 2009; Sun et al., 2010; Zhong

et al., 2009). In addition, a recently identified protein Pacer (protein associated with UVRAG as autophagy enhancer), is reported to interact with UVRAG, and antagonize Rubicon to activate autophagic pathway(Cheng et al., 2017). These various Beclin1-Vps34 multiprotein complexes are involved in autophagosome biogenesis, maturation, and membrane-associated processes crucial for autophagic pathway. Structural and functional defects in these Beclin1-Vps34 complexes disrupt cellular homeostasis, and have been reported to associate with diseases like cancer, neurodegeneration and infection (Morris et al., 2015). Therefore, understanding the molecular architecture of these protein complexes, including the structure of the whole complex or part of the components, as well as how these components assemble and disassemble, is critical for elucidating the molecular mechanisms of autophagy pathway.

1.2.2 Atg14L and UVRAG: two mutually exclusive subunits of Beclin1-Vps34 complexes

Atg14L and UVRAG are two positive effectors of Vps34, forming two mutually exclusive PI3KC3 complexes that direct the core Beclin1-Vps34-Vps15 assembly to diverse cellular processes (Itakura et al., 2008; Sun et al., 2008). The Atg14L-containing PI3KC3 complex Ⅰ functions at the downstream of the ULK1 complex, and plays a role in the early step of autophagosome formation (Noda et al., 2011). On the other hand, the UVRAG-containing PI3KC3 complex II acts as a regulator in

autophagosome maturation and endocytic traffic (Funderburk et al., 2010; Thoresen et al., 2010). Additionally, UVRAG stimulates Rab7 GTPase activity via interaction with class C Vps complex, thereby promotes the fusion of autophagosomes with late endosomes/lysosomes (Liang et al., 2008). Although the functional roles of these PI3KC3 complexes have been described largely by a variety of studies, molecular details controlling how are they assembled together spatially and temporally still unclear.

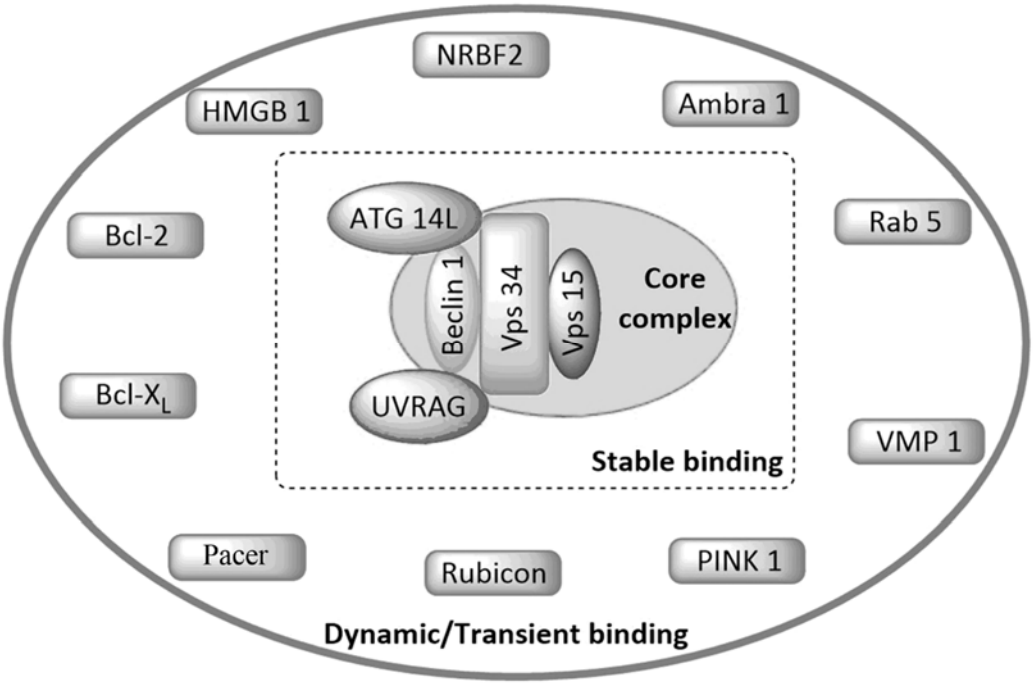

Figure 1.2 The "primary" or "secondary" interactors of Beclin1-Vps34 complex. HMGB1: high-mobility group box 1; NRBF2: nuclear receptor binding factor 2; PINK1: PTEN-induced putative kinase 1; VMP1: vacuole membrane protein 1.

Many lines of evidence from our lab and other research groups have emphasized the fact that coiled-coil domain of Beclin1 is essential for the interaction with Atg14L and UVRAG (He and Levine, 2010; Li et al., 2012). The structure of Beclin1 CC domain published by our lab reveals an anti-parallel homodimer, in which three leucine pairs “zipper” the coils together to form an “imperfect” dimer interface. This homodimer is metastable because of an array of polar or charged residues located on the dimer interface, and considered to be the inactive state of Beclin1. Both Atg14L and UVRAG also contain coiled-coil domains that are responsible for binding with Beclin1. Our biochemical data reveal that the Beclin1 coiled coil homodimer readily converts to stable Beclin1-Atg14L/UVRAG heterodimer, probably driven by more favorable pairings formed between Beclin1 and Atg14L or UVRAG (Li et al., 2012). Recently, our lab also determined the Beclin1-UVRAG coiled-coil complex that confirmed additional favorable pairings at the Beclin1-UVRAG coiled coil interface to strengthen this heterodimeric assembly (PDB code 4KA1, manuscript to be submitted). However, the mechanism how Atg14L forms stable interaction with Beclin1 is still unclear.

1.2.3 Architecture and flexibility of Beclin1-Vps34 complexes

Our understanding of the molecular architecture of these PI3KC3 complexes has greatly improved in recent years, as revealed by multiple studies using electron microscopy, crystallography, hydrogen deuterium exchange mass spectrometry, and

other structural and biochemical approaches.

A recent published paper by Hurley's group in University of California, Berkeley, provides the first view of the overall architectures of both Atg14L-containing complex Ⅰ and UVRAG-containing complex Ⅱ (Baskaran et al., 2014). These structures are obtained at 28 Å resolution via the combination of single-particle electron microscopy and hydrogen deuterium exchange studies, showing almost identical V-shaped architectures except UVRAG taking the place of Atg14L in the complex Ⅱ (Figure 1.3). In this model, the CC assemblies and the C-terminal domains of Beclin1-Atg14L/UVRAG constitute the long left-hand arm of the V shape, while the right-hand arm includes the helical and catalytic domain of Vps34, and the kinase domain (WD40 repeat domain) of Vps15. The N-terminal C2 domain of Vps34 together with the HEAT repeat domain of Vps15 locate at the junction of the V architecture. The N-terminal sequences of Beclin1 and Atg14L/UVRAG position together near the junction, suggesting that the coiled coils of Beclin1 and Atg14L/UVRAG are parallel to each other, distinct from the anti-parallel pattern of Beclin1 homodimer.

Shortly afterwards, another paper reported the crystal structure of the yeast homolog of the UVRAG-containing complex Ⅱ solved at 4.4 Å resolution, which reveals a similar Y-shaped architecture (Rostislavleva et al., 2015). Likely, Vps34 and Vps15 subunits form the catalytic arm on the right-hand side, while the parallel heterodimeric Atg30 and Atg38 (homologs of Beclin1 and UVRAG) form the

regulatory arm on the left. It is also suggested that both arms of the structure work together to properly associate with target membranes, and that the conformational flexibility of the structure would enable opening of the arms to suit different membrane curvatures (Rostislavleva et al., 2015).

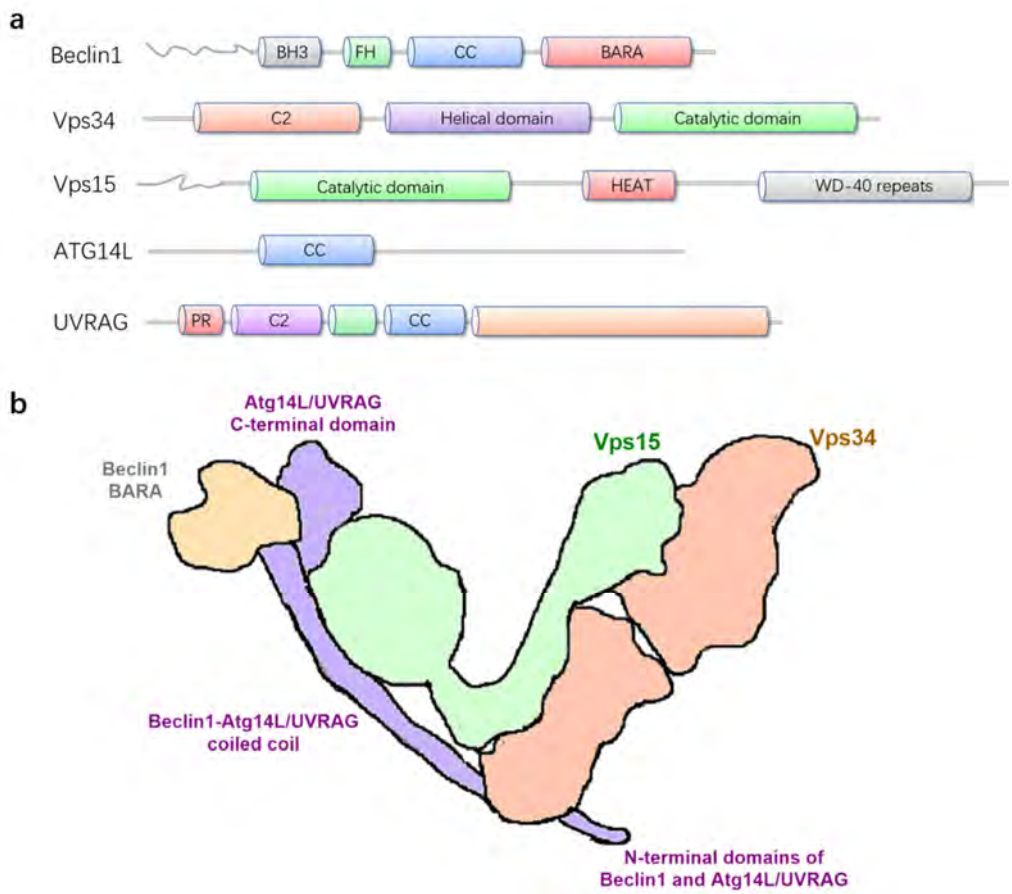

Figure 1.3 Schematic model of the constitution and architecture of the PI3KC3 complexes. **a**, the diagram illustrating domain structures of Beclin1-Vps34 complex subunits. **b**, the overall structure of the PI3KC3 complexes, modified form the crystal structure of yeast PI3KC3 complex II (Rostislavleva et al., 2015). The positions of each domain of Beclin1, Atg14L and UVRAG are labelled.

1.3 Beclin2 is A Newly Identified Beclin1 Homolog

1.3.1 Beclin2 is a homolog of Beclin1 with notable distinctions

Beclin2, the focus of this project, is a novel autophagy-related protein that was recently identified as a homolog of Beclin1 (He et al., 2013). Identified only in mammalian so far, Beclin2 also comprises the same BH3, FH, CC and BARA domains as Beclin1 (Figure 1.4). According to the protein sequence alignment result in Figure 1.5, Beclin2 shares high sequence identity with Beclin1 in CC domain (54%) and BARA domain (65%), but with great divergence at N terminus.

In addition, notable distinction between these two orthologs can be found in their genetic organization and tissue expression profiles. Beclin2 gene is localized at the human chromosomal subregion 1q43, which is frequently implicated in the metabolic hemostasis and is associated with obesity and diabetes-related quantitative traits (Aissani et al., 2006; Aissani et al., 2013). Messenger RNA (mRNA) and protein expression analysis reveal that Beclin2 is mainly expressed in several tissues such as brain, skeletal muscle and uterus, but weakly expressed in liver and stomach.

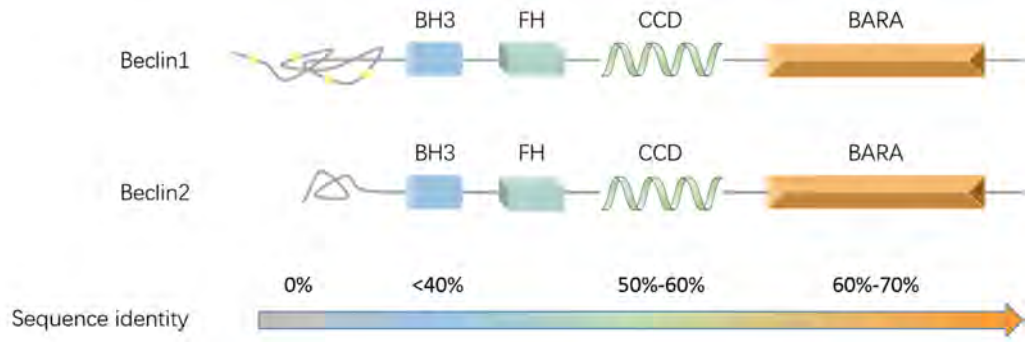

Figure 1.4 The schematic diagrams of domain structures of Beclin1 and Beclin2 (not proportional). The bottom shows the sequence identity percentage between Beclin1 and Beclin2.

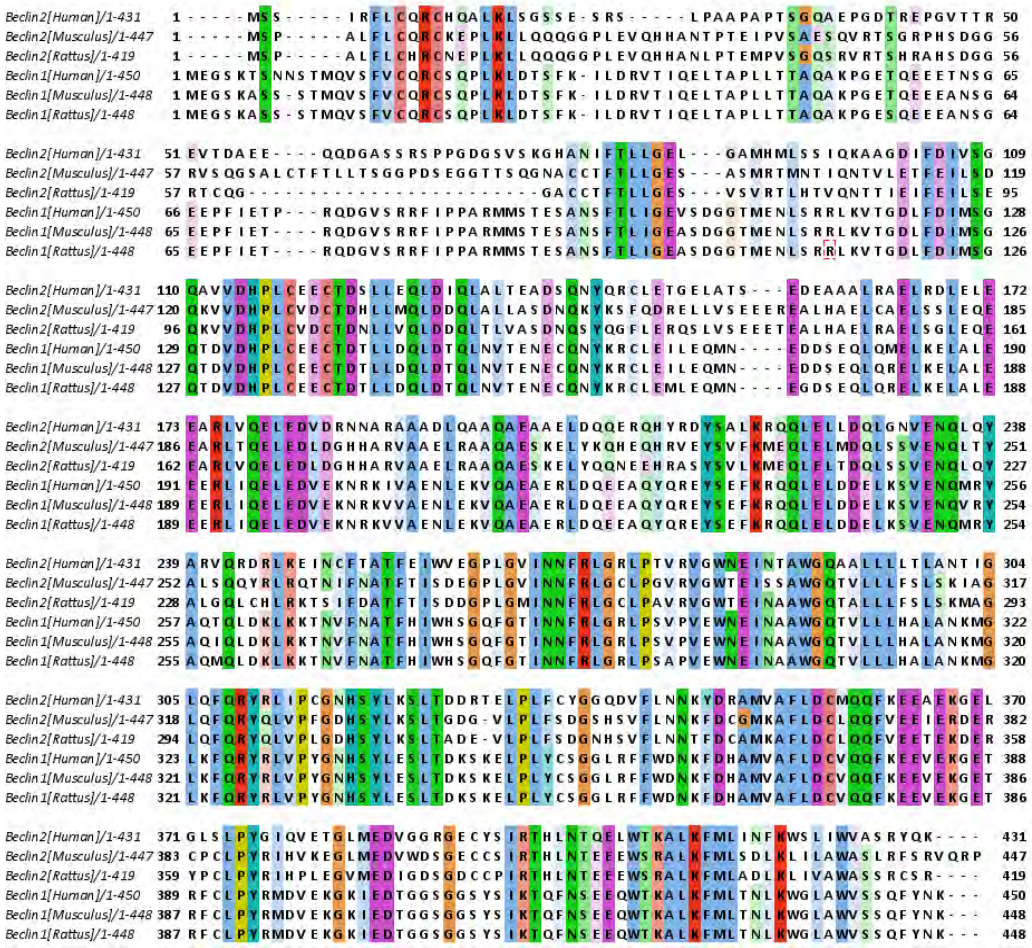

Figure 1.5 Multiple sequence alignment of Beclin2 and Beclin1 using Clustal (http://www.ebi.ac.uk/Tools/msa/clustalo/).

1.3.2 Beclin2 is an autophagy modulator by forming Beclin2-Vps34 complexes

Given the high sequence similarity between Beclin1 and Beclin2 (roughly 57% in human and 44% in mouse), it is reasonable to assume that Beclin2 may interact with some binding partners of Beclin1. In fact, several autophagy-related proteins in Beclin1 interactive network, including Bcl-2, Atg14L, UVRAG and Ambra1, were identified to interact with Beclin2 by the coimmunoprecipitation assay, implying the potential of Beclin2 in autophagy regulation (He et al., 2013). By forming the homologous Beclin2-Vps34 complex via the above Vps34 modulators, it is likely that Beclin2 plays a similar role as Beclin1 in Vps34-dependent autophagy and endolysosomal trafficking.

However, the interactome of Beclin1 and Beclin2 is not exactly overlapping, for example, Rubicon, another autophagy regulator, interacts with Beclin1 but not Beclin2 (He et al., 2013). On the other hand, although interacting with same binding partners, Beclin2 differs from Beclin1 with regard to the binding affinity and regulatory mechanism. The coimmunoprecipitation assay reveals that the association of Ambra1 with Beclin2 is stronger than with Beclin1. Moreover, unlike Beclin1, the Beclin2-Bcl-2 interaction was not disrupted upon starvation (He et al., 2013).

Collectively, the discovery of Beclin2 has provided several lines of evidence showing that mammalian cells have at least two Beclin family proteins in autophagy regulation. The reasons why two Beclin isoforms are needed, rather than only one in invertebrate organisms, deserve further investigation. Considering the common binding partners and the shared function mentioned above, it is worth to examine whether there is a complementary mechanism between two Beclin isoforms. From another perspective, it is also possible that Beclin2 develops some unique characteristics different from Beclin1 that may regulate autophagy separately or by different mechanisms. This possibility could be supported by the distinct properties of Beclin2 in interacting with various Vps34 modulators, and by the high expression level of Beclin2 in specific tissues including brain and uterus.

1.3.3 Beclin2 participates in the endolysosomal degradation process

Apart from formation of Beclin2-Vps34 complexes, it is recently reported that Beclin2 participates in the modulation of ligand-induced EGFR lysosomal degradation. Treatment with Beclin2 siRNA in A549 cells reveals inhibitory effect in agonist-induced EGFR degradation, whereas treatment with Beclin1 or Atg14L siRNA shows minimal effect on EGFR degradation(Zhang and He, 2014). Given the crosstalk between the autophagy machinery and endolysosomal sorting pathways, it is worthwhile to investigate whether Beclin2 promote the endolysosomal degradation of EGFR in a Vps34-dependent manner, and whether other mechanisms such as

ubiquitination involved.

Additionally, it is reported that EGFR negatively regulates autophagy through Beclin1 phosphorylation, which blocks the Beclin1-Atg14L interaction by stabilizing the Beclin1 homodimer (Wei et al., 2013). The potency of Beclin2 in enhancing EGFR degradation, may probably lead to autophagy restoration by downregulating EGFR signaling. Yet, whether Beclin2 regulates EGFR degradation through direct association is still unknown, nor the sequence regions responsible for such regulation. Further studies addressing these questions and revealing the molecular mechanism of Beclin2 are required, which may facilitate a complete understanding in autophagy modulation that is previously unappreciated.

1.3.4 Beclin2 regulates GPCR degradation via interaction with GASP1

Despite the homologous features at central and C-terminal regions, Beclin2 and Beclin1 display great sequence difference at the N-terminus. This distinct sequence implies that unique interacting partners and functions might be presented. Applied an 88 amino acids protein fragment at the N terminus of human Beclin2 as a bait, G protein-coupled receptor associated sorting protein 1 (GASP1) was discovered in the yeast two-hybrid screening as an interacting partner of Beclin2. However, no interaction existed between Beclin1 and GASP1 as detected by the similar analysis, suggesting that such interaction with GASP1 is unique to Beclin2 (He et al., 2013).

The published data also suggests the C-terminal armadillo repeats domain of GASP1 is responsible for its interaction with the N-terminal tail of Beclin2 (He et al., 2013). This interaction is specific for GASP1, even though significant sequence similarity in the C-terminal region is present in all GASP family members (Abu-Helo and Simonin, 2010). GASP1 is a large cytoplasmic protein that contains 1395 amino acids. Thus far, at least 30 G protein-coupled receptors (GPCRs) are reported to interact with GASP1 through their C-terminal tails (Heydorn et al., 2004). However, GASP1 could only efficiently regulate the post-endocytic sorting of several GPCRs, including D2 dopamine receptors (D2R)(Bartlett et al., 2005), δ-opioid receptor (DOR)(Whistler et al., 2002), type 1 cannabinoid receptor (CB1R)(Martini et al., 2007), and G protein-coupled receptor 55 (GPR55) (Dores and Trejo, 2014).

GPCR represent a super protein family of transmembrane receptors involved in the cellular signals transduction. Each GPCR protein is characterized by its seven transmembrane domains, with an extracellular N-terminal tail and a cytoplasmic C-terminus. This hepta-helical structure allows GPCRs to sense extracellular agonists and transduce the cellular signaling. Upon activation, GPCRs undergo conformational alterations and transduce signals into cytoplasm, followed by the rapid desensitization through phosphorylation and β-arrestin binding (Marchese et al., 2008). Subsequently, GPCRs are internalized in endosomes where two distinct eventual results would happen (Dores and Trejo, 2014). For one, GPCRs are

dephosphorylated within endosome and released back to the plasma membrane. For the other, GPCRs are sorted to lysosomes and degraded typically through the ubiquitin-dependent ESCRT (Endosomal Sorting Complex Required for Transport) machinery (Marchese et al., 2008) or ubiquitination-independent GASP1 pathway (Abu-Helo and Simonin, 2010; Whistler et al., 2002). The GPCR signaling plays a critical role in maintaining cellular homeostasis, while its dysfunction could result in a variety of physiologic disorders, such as cardiovascular and metabolic diseases. In fact, therapeutic agents targeting GPCRs have contributed to more than one third of currently used drugs (Eglen et al., 2007).

The interaction between GASP1 and Beclin2 leads to an autophagy-independent function of Beclin2 in regulating GPCRs endolysosomal degradation. This is supported by the evidence that elevated expression of GASP1 substrates, DOR and CB1R, are found in Beclin2 knockout mice (He et al., 2013). Additionally, Beclin2 is found to predominantly express in brain, which agrees with the finding that high expression level of GASP1 in central nervous system (Simonin et al., 2004). Taken together, the GASP1 C-terminal tail appears to mediate interactions with both GPCRs C-terminus and Beclin2 N-terminus, while little is known about the structural mechanisms and the biological functions of these interactions. Future studies are required for better understanding of the molecular mechanism of Beclin2-GASP1 interaction.

In summary, as implied by their respective binding partners, both Beclin1 and Beclin2 exert functional roles in autophagy regulation, but with notable distinctions. In addition, they serve distinct functions beyond autophagy. For example, Beclin1 is involved in apoptosis while Beclin2 plays a role in GPCR degradation. Besides, Beclin2 possesses a characteristic function of binding with GASP1, which results in the modulation of specific GPCR signaling. However, the molecular mechanism by which Beclin2 coordinates the dual functions of autophagy and GPCR degradation is not fully understood.

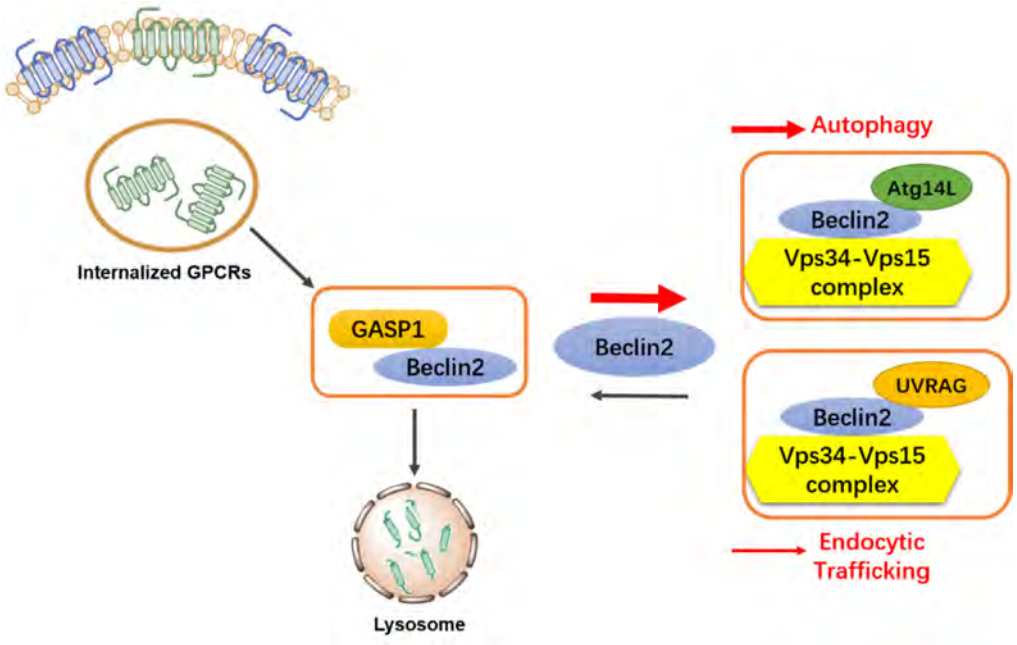

Figure 1.6 Schematic illustrating the dual action of Beclin2 in mediating autophagy and the lysosomal sorting of GPCRs.

1.4 The Objectives of This Study

In this thesis, we propose to conduct biochemical and structural study to understand the functional role of Beclin2 in autophagy and GPCR trafficking. Specifically, we aim to investigate three objectives.

The first objective is to investigate, for Beclin2's role in mediating autophagy, how the Beclin2-Vps34 complex is biochemically and functionally distinct from the homologous Beclin1-Vps34 complex. For this objective, we plan to first carry out biochemical studies of the Beclin2-Atg14L/UVRAG interaction and investigate whether the binding affinities of Beclin2 to these two autophagy enhances show different pattern as compared to that for Beclin1. We also plan to determine the crystal structure of the Beclin2 coiled coil domain and to confirm if Beclin2 possesses similar "imperfect" and metastable dimer interface like Beclin1 to facilitate its interaction with Atg14L and UVRAG. Lastly, we plan to determine the structure of the Beclin2-Atg14L/UVRAG coiled coil complex to delineate molecular determinants that favor this heterodimeric assembly over Beclin2 homodimer to promote the eventual formation of Beclin2-Vps34 complex for autophagy activity.

For the second objective, we would like to identify the molecular determinants that enable GASP1's specific binding to Beclin2, but not to Beclin1, which is critical for Beclin2-mediated trafficking of GASP1-associated GPCRs. We plan to first use

proteomic analysis to confirm direct interaction between GASP1 and Beclin2. Then we aim to biochemically map the Beclin2 peptide that binds to the C-terminal armadillo Repeat domain of GASP1, so that the molecular determinants for this specific Beclin2-GASP1 interaction can be derived.

For the third objective, we aim to investigate if Beclin2-mediated GPCR can be targeted by designed peptides to modulate GPCR signaling. Our lab's on-going study has led to the rational design of stapled peptides that can promote autophagy by specifically targeting the Beclin1 coiled coil domain. We plan to test if these small molecule compounds can target Beclin2 and promote GASP1-associated GPCR trafficking. Given that GASP1-associated GPCRs like δ opioid receptor (DOR), cannabinoid 1 receptor (CB1R) and dopamine D2 receptor (D2R) play critical roles in regulating food intake and analgesic response, these designed molecules may be of potential interest to drug discovery effect for diabetes and antipsychotic treatment.

Chapter Two: Methodology

2.1 Gene Cloning and Recombinant Protein Expression

2.1.1 Total RNA extraction

Total RNA was isolated from HEK293 cells using Trizol reagent (Life technologies) according to the manufacturer's manual. Before RNA isolation, attaching HEK293 cells were grown in monolayer reaching roughly 80% confluence. After removal of media, cells were rinsed with ice-cold PBS. 1ml Trizol reagent was then pipetted into the cell culture dish, and the cell lysate was scraped and transferred to a clean centrifuge tube. 200 µl chloroform was then added to the tube and mixed vigorously by vortex for 15 sec, incubated at room temperature for 3 min. Followed by the centrifugation at 4℃, 12000 X g for 15 min, and then the upper aqueous phase was pipetted carefully to a fresh tube. 500 µl isopropanol was then added and incubated at room temperature for 10 min. After centrifugation at 4℃, 12000 X g for 10 min, the supernatant was removed completely and the RNA pellet was washed with 1 ml 75% pre-cool ethanol. Centrifugation was performed at 4℃, 7500 X g for 5 min, and the supernatant was pipetted out. The RNA pellet was then air-dried for 5 min and dissolved in DEPC-treated water. Total RNA concentration was determined by spectrophotometry. RNA integrity was determined by assessing the total quantity of 18S/ 28S RNA. RNA was stored at -80℃ until any further process.

2.1.2 First strand cDNA synthesis

Around 20 μg total RNA was reversely transcribed to generate the first strand cDNA by PrimeScript™ II 1st Strand cDNA Synthesis Kit (Takara). Denaturation of template RNA:

Reagents	Volume (μl)
Oligo dT primer	1
dNTP mixture	1
template RNA	2
RNase free H_2O	up to 10

Mixed gently and placed at 65℃ for 5 min, then cooled on ice immediately.

Reverse transcription:

Reagents	Volume (μl)
Mixture used for denaturation from last step	10
5X PrimeScript Buffer	4
RNase Inhibitor	0.5
PrimeScript II RTase	1
RNase free H_2O	up to 20

Placed the tube in the Thermal Cycler and set the program as follows.

Temperature (℃)	Duration (min)
42	35
70	15
4	∞

Stored at -20℃ freezer before proceeding to the downstream application.

2.1.3 Plasmid construction

The target gene was amplified by polymerase chain reaction (PCR) using the achieved cDNA as a template.

Reagents	Volume (µl)
5X HF Buffer	4
dNTP (10 mM)	0.4
template	0.3
Forward primer	0.2
Reverse primer	0.2
Phusion™ High-Fidelity DNA Polymerases	0.2
Milli Q water	up to 20

The mixture was placed in the Thermal Cycler, and the PCR program was set as follows.

Step	Temperature (℃)	Duration (sec)
1	98	180
2	98	30
3	T_m	30
4	72	45
5	Go to 2	35 cycles
6	72	600
7	4	∞

Then the agarose gel electrophoresis was carried out, and the resulting PCR product was purified from agarose gel using gel purification kit (BioTeke) as per manufacturer's instructions. After purification, the PCR product was used as primer to do ligation-independent cloning (Aslanidis and Dejong, 1990; Haun et al., 1992), the reagent composition and program setting are listed as follows.

Reagents	Volume (μl)
5 x HF Buffer	4
dNTP (10 mM)	0.4
Template (vector plasmid)	0.3
PCR product (used as primers)	2
Phusion™ High-Fidelity DNA Polymerases	0.2
Milli Q water	up to 20

Step	Temperature (℃)	Duration (sec)
1	98	180
2	98	30
3	T_m (48-54)	40
4	72	180
5	Go to 2	25 cycles
6	72	1200
7	20	600
8	4	∞

Recombinants were generated through circularization between PCR product and vector plasmid as mediated by the 15-21 nucleotide ends that are complementary to the vector's sequence. The resulting recombinant samples were

subjected to DpnI (Fermentas) digestion at 37℃ for more than 6 hours to remove the template plasmids.

2.1.4 Transformation

The frozen competent cells were taken out of the freezer and thawed on ice. Appropriate number of recombinant molecules were pipetted into competent cells, mixed gently and incubated on ice for 30 min. Heat-shock reaction was performed in 42℃ warm water for 90 sec, and then transferred into ice immediately for 5 min. Competent cells were grown in 500 µl antibiotic-free LB media in 37℃, 250 rpm shaking incubator for 45 min. The sample was then plated into a pre-warm LB agar plate with the corresponding antibiotic and incubated overnight.

2.1.5 Mutants or variants generation

To generate mutations or variants of different length (including deletion and insertion), overlap extension PCR cloning was applied using wild-type constructs as templates. Then these variants are verified by DNA sequencing service provided by the BGI Company.

2.1.6 Over-expression of recombinant proteins in *E.coli*

Small-scale expression

It is critical to search the appropriate expression condition and lysis condition for protein expression and purification. Therefore, optimization of expression conditions such as induced temperature, IPTG concentration, and lysis conditions such as lysis buffer are highly recommended.

Parallel small-scale expression tests were performed at different temperature, namely, 16℃, 30℃ and 37℃. Specifically, single colonies were picked and transferred to 50ml tubes containing 10ml LB supplemented with appropriate antibiotics. Then cell cultures were incubated at 37℃ until the OD_{600} reached 0.6, and the expression of recombinants were induced at the indicated temperature with 0.3 mM IPTG. After induction for particular time length, cells were harvested and subjected to lysis with different types of lysis buffer (PMSF and β-ME were added immediately before lysis), followed by sonication (35% amplitude, 10sec pulse, 12sec pause, 5 min). The sample was kept on ice throughout the sonication process to prevent overheating. Lastly, the sonicated samples were transferred to 1.5 ml tubes and centrifuged at 4℃, 10000 rpm for 30 min.

Then SDS-PAGE was carried out to test the expression and solubility of the desired protein. After electrophoresis, protein bands are visualized using Coomassie blue staining.

Large-scale expression

Followed by the optimization of expression conditions and sonication conditions, recombinant proteins with considerable expression and solubility are ready to go for large-scale expression.

Similar to small-scale expression, after IPTG induction, cells were harvested and sonicated at 35% amplitude, 10 sec pulse, 12 sec pause, 25 min. The sonicated sample was then transferred to a 50 ml centrifuge tube (Nalgene) and centrifuged at 4℃, 18000 rpm for 2 hours. The supernatant after centrifugation was filtered by 0.22 μm membrane before subjected to affinity column.

2.1.7 Selenomethionine substituted protein for phase determination

Selenomethionine substituted Beclin2 coiled coil protein is applied for phasing experiments. Given the wild type Beclin2 CC does not contain methionine in the sequence, mutating other residues into methionine is required. Of noted, the mutated site should not be involved in the critical crystal contacts. Our first attempt in Beclin2 CC Se-derivatization involved the incorporation of mutants Q222M and L236M, and they were grew individually using the M9 Se-Met high-yield growth media kit (Medicilonic). As instructed by the manufacturer, the *E.coli* transfected with Beclin2 Q222M or L236M was cultured at M9 salts media supplemented with minerals and vitamins at 37℃, followed by adding Se-Met and inhibitory amino acid cocktail when the OD_{600} reached 1.2, and incubating at 20℃ for 15min. Then IPTG

was added, and cells were grew at 20℃ overnight.

2.2 Purification

2.2.1 Affinity chromatography

Binding buffer: 20 mM sodium phosphate, 0.5 M NaCl, 40 mM imidazole, pH 7.4, 10% Glycerol.

Elution buffer: 20 mM sodium phosphate, 0.5 M NaCl, 0.5 M imidazole, pH 7.4.

The 5 ml HisTrap HP column (GE Healthcare) was washed with 25 ml Milli Q water, followed by 25 ml elution buffer, and then equilibrated with 35 ml binding buffer.

The recombinant protein containing a hexa-histidine (His_6) tag was then loaded into the column using Superloop (GE Healthcare). After loading, the column was washed with 75 ml binding buffer or until the UV absorbance reached baseline, and then the His_6-tagged protein was eluted by 25 ml elution buffer. The flow rate was set as 4 ml/min for the whole procedure except the sample loading step (1 ml/min).

2.2.2 Protease digestion

After elution, 1% (w/w) 3C protease was added to the fusion protein sample to remove the His_6 tag and its fusion partner. The digestion reaction was conducted at 4℃ for overnight.

2.2.3 Poly-histidine tag and fusion partner removal

The resulting digested sample, which is a mixture of the desired protein, 3C protease, His_6 tag and fusion partner, was subjected to HisTrap HP column again. The desired protein and 3C protease would be presented in wash fractions, while incompletely digested fusion protein, His tag and its fusion partner would be present in eluted fractions. The wash fractions were then collected and concentrated by Amicon Ultra centrifugal filter units (Millipore).

2.2.4 Size Exclusion chromatography

The HiLoad 16/600 Superdex 75 PG column (GE Healthcare) was equilibrated with the appropriate buffer (normally the target protein storage buffer) using the ÄKTA purifier (GE Healthcare). The concentrated protein sample (less than 5 ml) was injected into the column, and proceeded to wash the column at the flow rate of 1 ml/min. Proteins would be separated on the basis of their molecular sizes. Fractions were collected when increase in UV absorbance was observed, and all fraction samples collected were subjected to SDS-PAGE analysis to detect the desired protein.

2.2.5 Concentration determination

Fractions with the desired protein from size exclusion chromatography were concentrated, and their concentrations were determined by Bio-Rad protein assay

reagent (Bio-Rad). Standard curve was constructed using bovine serum albumin according to the manufacturer's instructions. Dye solution was prepared by diluting 200 µl dye reagent into 800 µl Milli Q water. 1 µl of concentrated protein sample was pipetted into the dye solution, and incubated for 5 min at room temperature. The absorbance was measured using the spectrophotometer (GE Healthcare) at 595 nm.

2.2.6 Protein storage

Purified and concentrated protein sample was flash-frozen by liquid nitrogen and stored at -80℃.

2.3 Biophysical and Biochemical Analysis

2.3.1 Mass spectroscopy

A small fraction of purified protein was subjected to buffer exchange in MilliQ water (Milipore). After desalting, the protein sample was mixed with acetonitrile containing 0.1% formic acid using a 1:1 ratio, in which acetonitrile acts as the mobile phase and formic acid acts as the ion-pairing agent. Then the mixture was subjected to matrix-assisted laser desorption/ionization (MALDI) mass spectrometry (Agilent technologies) for protein detection and identification.

2.3.2 Light scattering

Light scattering was performed by the SEC-MALS-DLS system, which is an efficient tool for detecting protein aggregates. 30-100 μg purified recombinant protein was injected into the ÄKTA purifier with SEC column (Superdex 200 10/300 GL, GE Healthcare). The column was equilibrated with the target protein storage buffer before use. The sample's UV absorbance signal was detected at 280 nm by ÄKTA purifier, and the light scattering signal was detected at 662 nm by DAWN HELEOS (MALS system, Wyatt technology), alone or in combination with DyNaPro NanoStar (DLS system, Wyatt technology). Data analysis was performed by the software ASTRA 6.1 (Wyatt technology). The molecular weights of protein samples were calculated by their theoretical extinction coefficients at 280 nm obtained by the

web server ProtParam (ExPASy, http://web.expasy.org/protparam/), and a default dn/dc value of 0.185 ml/g.

2.3.3 Circular dichroism spectroscopy

Circular dichroism (CD) is the differential absorbance of left-handed and right-handed circularly polarized light (LCPL and RCPL), which occurs when a molecule contains chiral chromophores. Circular dichroism spectroscopy is a spectroscopic technique which used extensively to evaluate the secondary structure or conformation of biological molecules over a range of wavelengths. For example, a typical α-helical spectrum shows characteristic negative peaks at 208 nm and 222 nm, and a maximum at 193 nm. Notably, the molar ellipticity at 222 nm is proportional to the amount of helix content(Johnson, 1988). The CD spectra of the β sheet structure, however, usually has a minimum near 220 nm and a positive peak in the 190-200 nm region, while “irregular” or “disordered” structures are usually used to represent those have spectrum that are not specifically assigned to the other categories, which show negative bands near 195 nm(Greenfield, 2006).

In addition, since the secondary structure is sensitive to the environmental conditions like temperature, circular dichroism can also be applied to observe how stable of this secondary structure with temperature changes using a specific wavelength.

2.3.4 Isothermal titration calorimetry

Isothermal titration calorimetry (ITC) is a quantitative biochemical tool that extensively used to characterize the direct molecular interactions. It measures the thermodynamic parameters of interactions occurred in solution, including the enthalpy changes (ΔH), binding affinity K_a, and binding stoichiometry (n) (Velazquez-Campoy et al., 2004b). Typically, an ITC experiment is carried out by the stepwise injection of a ligand solution into the sample cell containing another molecule. Endothermic or exothermic reaction will occur in the process of each titration. Molecules in the sample cell gradually saturate with the ligand addition, along with the gradual decrease of enthalpy changes, and leaving the background heat due to the ligand dilution in the end. The individual titration peak corresponding to each injection is integrated and plotted against the molar ratio to as indicated in Figure 2.1. The K_a and n values could be calculated through nonlinear regression of the resulted plotted curve (Pierce et al., 1999; Velazquez-Campoy et al., 2004a).

Sample preparation: to prevent air bubbles formation, all buffer and sample solutions should be degassed by centrifugation at 13000 rpm for 5 min. Besides, the sample concentration with a high degree of accuracy is necessary for determining an accurate association constant, K_a.

Sample loading: the titration syringe and sample cell were rinsed with buffer

solution several times before loading samples. The reference cell was filled with degassed Milli Q water (not necessary to refill after every experiment), and the sample cell was filled with the protein solution, while another protein solution was added to the titration syringe.

Experimental parameters including experimental mode, sample concentration, total number of injections and measurement temperature were set according to the MicroCal iTC200 user manual.

Data analysis was conducted by the software Origin provided by the manufacturer (MicroCal).

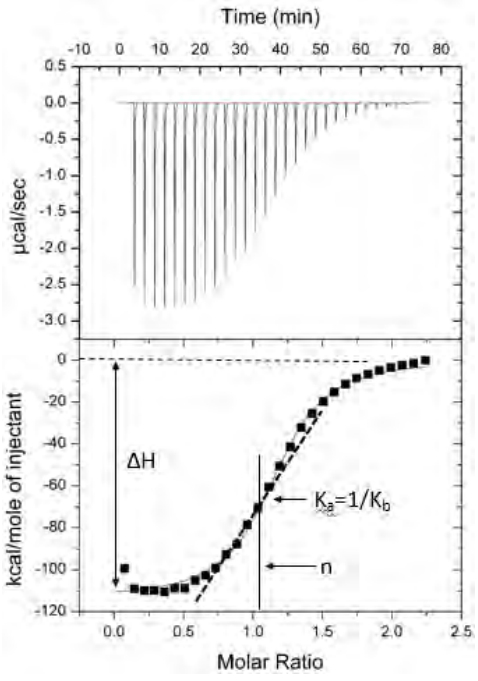

Figure 2.1 Illustration of the result of a typical ITC experiment.

2.3.5 Peptide array chip

A peptide array chip scanning through the Beclin2 N terminus (residues 1-105) was synthesized and purchased from JPT Peptide Technologies company. Specifically, the entire sequence is divided into 31 peptides, each with 15 amino acids long, and with 12 residues overlapping with the next contiguous peptide (Figure 2.2). These peptides are all covalently bound to a cellulose membrane, and subsequently tested for binding with GASP1. The membrane attached with Beclin2 peptides was co-incubated with purified His-tagged GASP1 after blocking with 5% milk at room temperature for 2.5 hours. In a similar manner with western blotting, the membrane was incubated with anti-His antibody overnight, followed by secondary antibody incubation, and finally exposed to detect signals.

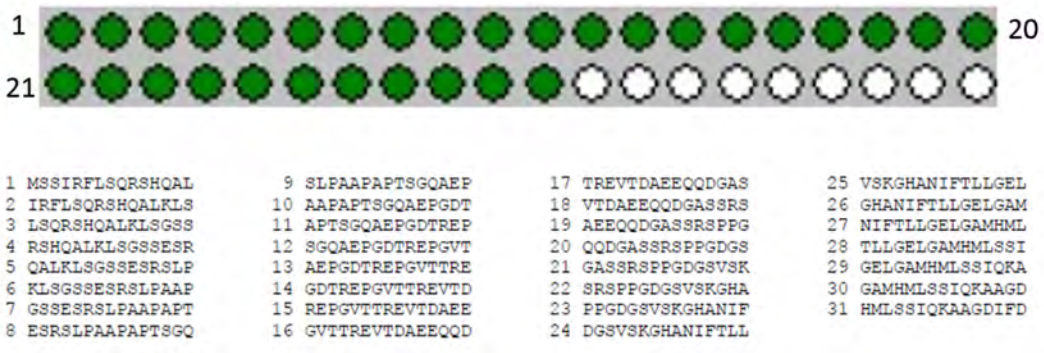

Figure 2.2 A schematic diagram of the peptide array chip scanning through Beclin2 residues 1-105. Each peptide is covalently bound to the cellulose membrane via its C terminal, and has an acetylate N terminus to protect from degradation. In addition, cysteines among the sequence are all substituted to serine residues.

2.4 Cell-based Experiments

2.4.1 Cell culturing

Cell culturing was performed at 37℃ in a humid CO_2 incubator. HEK293 cell and Hela cell were grown in DMEM medium supplemented with 10% FBS, and penicillin (100U/ml) / streptomycin solution (100μg/ml). HEK cell stably expressing flag-D2R was grown in DMEM medium supplemented with 10% FBS, penicillin (100U/ml) / streptomycin solution (100μg/ml), and zeocin (150μg/ml). For transfection experiments, cells were cultured in DMEM medium with 10% FBS.

2.4.2 Immunoprecipitation

When cells were grown to 90% confluency, an appropriate number of plasmids were transfected into culturing cells using Lipofectamine 2000 (Thermo Fisher). After incubation for 24 or 48 hours, cells were completely lysed under non-denaturing conditions, thus protein interactions could retain. Then the cell lysate was co-incubated with the target antibody and protein A/G agarose beads overnight, followed by washing to eliminate non-specific binding proteins. Subsequently, the immunoprecipitated sample was subjected to western blot analysis using the indicated antibodies.

2.4.3 Mass spectrometry-based interactome analysis

Protein immunoprecipitation coupled with mass spectrometry (IP-MS) provides insights to protein-protein interactions on a global scale (Aebersold and Mann, 2003). First, Immunoprecipitation assay was carried out as described, briefly, HEK cells were transfected with flag-Beclin2 wild type or 69-88 deletion mutant for 48 hours. The resulting immunoprecipitated samples were then eluted and loaded into an 8% polyacrylamide gel. The lanes were excised and subjected to reduction, alkylation and trypsin digestion as instructed by the protocol (Shevchenko et al., 2006), followed by analysis using mass spectrometry integrated with liquid-chromatography (LC-MS). Potential interacting proteins of high-confidence (false discovery rate 0.01) were identified subsequently. Theoretically, by comparing the interatom achieved from the wild-type and that from the deletion mutant, those missed interactors in the mutant are believed to be associated with Beclin2 N-terminus.

2.4.4 Biotin protection degradation assay

HEK cells stably expressing flag-tagged D2 dopamine receptors (referred to HEK-D2R hereafter) were seeded on 10cm culture dishes that pre-coated with 1% gelatin, and incubated at 37℃ to 90% confluency. As shown in Figure 2.3, cells were treated with biotinylation reagent (Thermo Fisher) at 4℃ for 30 min (to label receptors on the cell surface with cleavable disulfide-linked biotin and to prevent internalization

in the cold). Cells were then returned to warm DMEM media and incubated at 37℃ for 15min, followed by treatment with agonist dopamine (Sigma) at 37℃ for the indicated time to allow biotinylated receptors for internalization. Following the incubation, cells were moved back to 4℃ to stop endocytosis. To specifically quantify internalized receptors, cells were subjected to stripping reagent, by which the biotin on the cell surface receptor was cleaved off by the reducing agent glutathione (Sigma), while those internalized biotinylated receptors in endosome were protected from stripping. This pool of internalized biotinylated receptors was then lysed, immunoprecipitated, analyzed by western blot, and subsequently visualized by VECTASTAIN Elite ABC HRP Kit (Vector Laboratories) (Tschische et al., 2010).

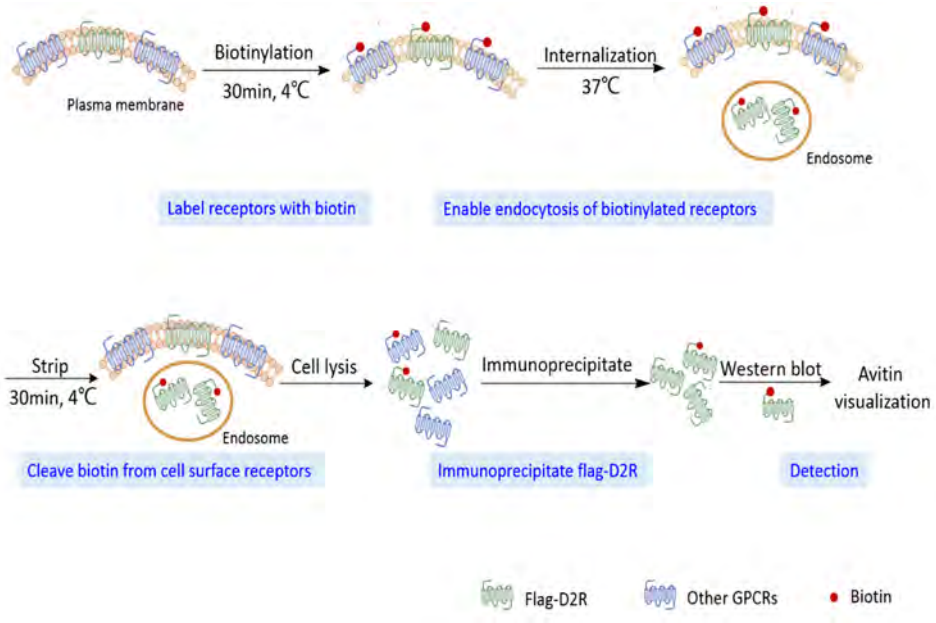

Figure 2.3 The schematic of the biotin protection degradation assay used to assess trafficking of flag-D2R in endosomes.

2.5 Structure Determination by X-ray Crystallography

2.5.1 Crystallization trials

Crystallization studies were performed by the hanging drop vapor diffusion method. Protein samples after purification (as pure as practically possible) with the divergent concentrations were applied.

Firstly, favorable crystallization conditions are identified by screening, because it is extremely difficult, if not impossible, to predict desired conditions for specific protein crystal growth. Crystal screen kits (Hampton research) containing a wide variety of solution conditions with divergent combinations of buffer component, salts, and precipitants, were applied for this step. According to the manufacturer's instructions, 400-500µl of each reagent was pipetted into one reservoir of the 24-reservoir plate. 1µl protein sample was then mixed with 1µl reservoir solution to the center of a clean siliconized cover slide, then this cover slide was inverted onto the edge of the reservoir and sealed with the vaseline. After repeating the operation for all reservoirs, plates were incubated at the 16℃ incubator.

Based on the screening results, subsequent crystallization condition optimization was conducted to obtain large single crystals suitable for x-ray diffraction. A diffraction quality crystal should be three-dimensional, with sufficient size, high purity and structural regularity, meanwhile, without any significant internal

cracks and crystal twinning.

2.5.2 Data screening and dataset collection

Subsequently, a single crystal was mounted on the x-ray machine, producing diffraction patterns as the gradual rotation of the crystal. Once mounted on the machine, the crystal is flash-cooled by liquid nitrogen, and additional step of cryoprotection may be required here, depending on whether cryoprotecting agents already included in the crystallization solution or not. Cryoprotectants such as 20% glycerol or PEG400 were applied if necessary. Lastly, these diffraction data were combined computationally and converted to the electron density map, generating the three-dimensional atomic structure. The diffraction data collection could be achieved by laboratory x-ray source or synchrotron beamlines.

2.5.3 Data processing

After data collection, the first step in the workflow of structure determination is raw-image diffraction data processing, including indexing, cell refinement, integration and scaling. The iMosflm program in the CCP4 package is applied for indexing, cell refinement and integration (Battye et al., 2011; Collaborative Computational Project, 1994). Generally, indexing is used to find crystal lattice to fit diffraction spots. It would do diffraction spots search using one or several images to determine the unit cell parameters, the likely symmetry, and estimate the mosaicity.

While the cell parameters determined here is an assumption and needs to be further tested after image integration. These cell parameters derived from indexing are further refined by cell refinement procedure. In default, two segments of images separated by about 90 degrees in phi are integrated for refinement. The integration is carried out to integrate spots on each image of the entire dataset, resulted in a dataset consisting of the indices (h, k, l) of all reflections with estimated intensities. During integration, the unit cell parameters are normally fixed, but the detector parameters and crystal orientation are further refined to ensure the best prediction of spot positions. Next, the POINTLESS program is used to determine the true symmetry, and with the space group determined by POINTLESS, scaling and merging is performed via Scala program in an attempt to scale together the individual parts of partially recorded reflections into unique reflections, and merges multiple observations into an average intensity. A series of statistic data are generated after scaling, including R_{merge}, completeness and redundancy, which would provide the insight of the data quality. Upon scaling, the Matthews coefficient could be calculated from Matthews program, in which shows the potential oligomeric state with reasonable solvent content in the asymmetric unit.

2.5.4 Phasing

Even though x-ray crystallography is applied extensively to determine three dimensional structures of macromolecules, there are still two major limiting factors,

one is getting the well-diffracting crystals, and the other is the phase problem, which could not be achieved directly from the diffraction experiment. After collecting diffraction data, phase information is required for the subsequent structure determination. Conventionally, the phase angle can be solved by molecular replacement (MR) that applying the atomic coordinates from a structurally similar protein, by multiple isomorphous replacement (MIR) that introducing heavy atoms into the protein, or by single or multi-wavelength anomalous diffraction (SAD/MAD) experiments. One common way to perform SAD/MAD is incorporating selenomethionine (Se-Met) into proteins, in which selenium atoms that replace the sulfur atoms produce a strong anomalous signal at its optimal wavelengths. The Se-Met derivatization of proteins shows advantages over the other two classes of methods in not requiring available structurally similar protein, nor having problems in locating heavy atoms. The diffraction dataset achieved by the Se-Met substituted protein at its optimal wavelength is processed as described previously. Upon scaling, the phase could be calculated and improved by multiple experimental phasing programs.

2.5.5 Model building and refinement

An initial approximate electron density map would be generated after crystallographic data processing and phase determination. Next, the protein sequence is inputted to build the atomic model into the obtained electron density

map. There are a number of programs available for building models automatically. However, the success model building could be very difficult with crystallographic data of low resolution. In addition, refinement by REFMAC program is required by varying all model parameters to improve agreement of the atomic model with the electron density distribution. Depending on the data quality and the phase accuracy, model building could be run iteratively with refinement of fragmentary models for multiple cycles. Ultimately, the refinement process usually involves manual corrections to better interpret the electron density distribution. The R-factor (R_{work}) is the value to evaluate how the model agree with the experimental crystallographic data, while the Free R-factor (R_{free}) is applied to assess the possible over-modeling or over-refining of the data. Generally, the R_{work} and R_{free} value should be similar. Considering the large size of macromolecules, the R value is seldom better that 15%, and R-factors ranging from 15% to 30% are acceptable for proteins.

2.6 The Overall Workflow of This Study

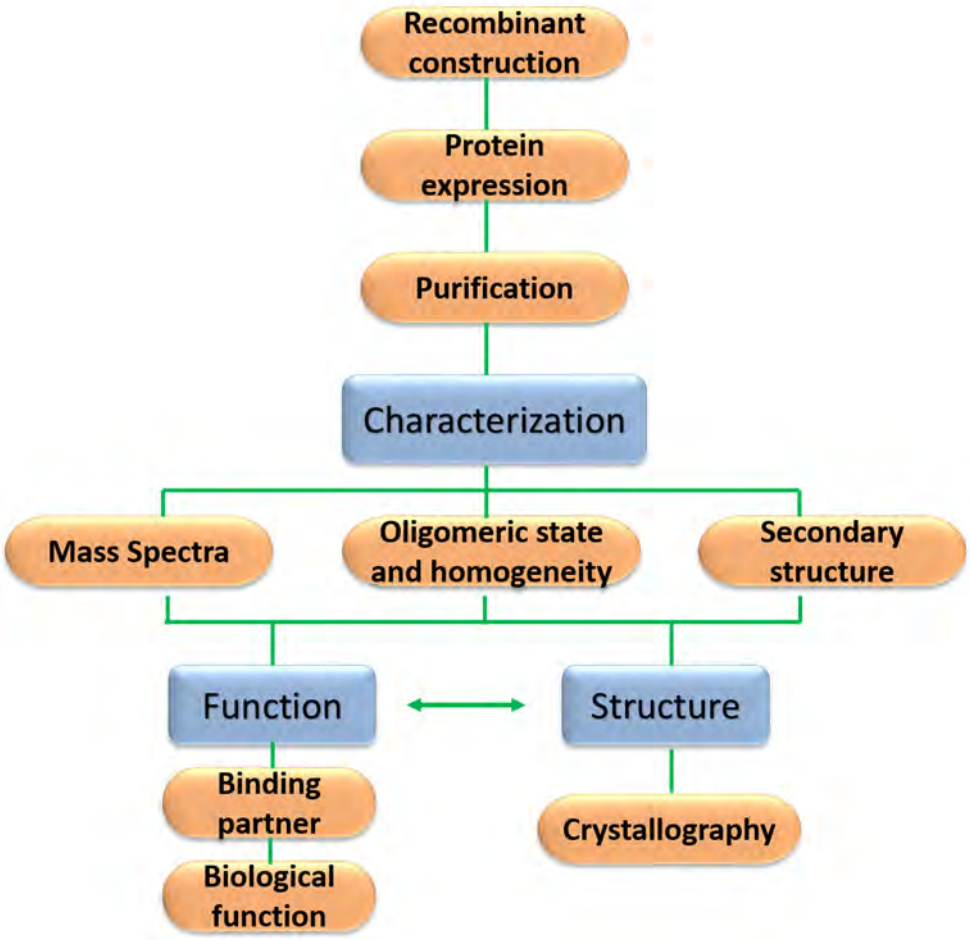

Figure 2.4 A schematic diagram of the workflow. Including recombinant cloning, protein expression, purification, biochemical characterization, crystallography and functional studies.

Chapter Three: Biochemical and Structural Studies of Beclin2 Coiled coil domain

3.1 Overview

The recently published data together with our own studies suggest that the coiled coil (CC) domain of Beclin2 is the major binding site that responsible for Atg14L and UVRAG interactions. As derived from our previous published crystal structure of Beclin1 CC domain, the corresponding CC fragment of Beclin2 (residues 158-250) was designed.

Before we proceed to compare the binding affinities of Beclin2 toward Atg14L and UVRAG, we would like to first analyze the Beclin2 CC domain alone and assess its oligomeric state as well as metastability. This plan is also inspired by our previous study of the Beclin1 CC domain, which showed a metastable homodimer with "imperfect" coiled coil interface (Li et al., 2012). This metastability is essential because it facilitates the transition of Beclin1 homodimer to Beclin1-Atg14L/UVRAG heterodimeric complex. Mutations that stabilize the Beclin1 homodimer lead to weakened Atg14L/UVRAG binding and subdued autophagy response. If Beclin2 CC domain binds to Atg14L/UVRAG in the similar manner as Beclin1, then adopting the metastable homodimeric state is a pre-requisite and thus need to be confirmed first.

3.2 Experimental Results

3.2.1 Recombinant plasmid construction and expression of Beclin2

3.2.1.1 Gene cloning and construct engineering

As shown in Figure 3.1, total RNA was extracted from HEK293 cells using Trizol reagent and analyzed by agarose electrophoresis. Followed by the reverse transcription PCR to generate cDNA, which was subsequently used as the template to amplify Beclin2 CC. Forward primer: CCAGGGGCCCGGATCCGAGGCGGCGGCGCTG; Reverse primer: GACGGAGCTCGAATTCTCAGTTGATTTCCTTCAG.

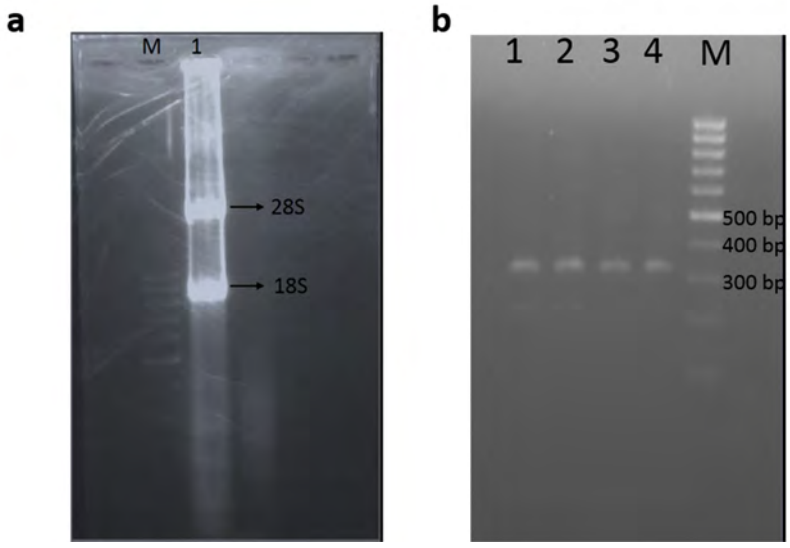

Figure 3.1 Total RNA extraction and PCR amplification of Beclin2 CC. **a**, total RNA isolation from HEK293 cells; Line M: marker; Line 1: total RNA. **b**, agarose gel electrophoresis of PCR amplification products. Lane 1-4: Beclin2 CC; M: Marker.

The amplified Beclin2 CC gene was then cloned into the modified pET32 vector (pET32m), which contains a thioredoxin (Trx) tag, a hexa-histidine (His_6) tag, and a human rhinovirus 3C protease cleavage site. The recombinant gene was inserted after the 3C protease cleavage site, which enables the removal of fusion tags by 3C protease digestion.

3.2.1.2 Expression of Beclin2 CC domain

The recombinant was transformed into *E.coli* BL21, and grown at 37℃ until OD_{600} reached 0.6-0.8. Then IPTG was added to a final concentration of 0.2 mM, and the cell culture was incubated at 30℃ and shaken at 250 rpm in a shaking incubator for 6 hours.

3.2.2 Purification of Beclin2 CC domain

For purification, *E.coli* cells were harvested after IPTG induction, and lysed by sonicator in lysis buffer (50mM Tris, 150mM NaCl, pH 8.0, 1 mM PMSF, 0.7% β-ME). Figure 3.2 shows the expression and purification effect. Briefly, cell lysate was loaded to the HisTrap affinity column, and after washing out the unbound proteins, 3C protease was added directly into the column and digested at 4℃ overnight. After digestion, the 3C protease and target protein without His_6 tag would be washed out from column, while fusion protein (Beclin2 CC+Trx+His_6) and fusion tags (Trx+His_6) would be in elute fractions (Figure 3.2 a). The washed fractions were further purified

using the size exclusion chromatography to separate the 3C protease and Beclin2 CC (Figure 3.2 b&c), and the pure Beclin2 CC was fractionated. All samples were analyzed and detected by Coomassie staining after separation by SDS-PAGE.

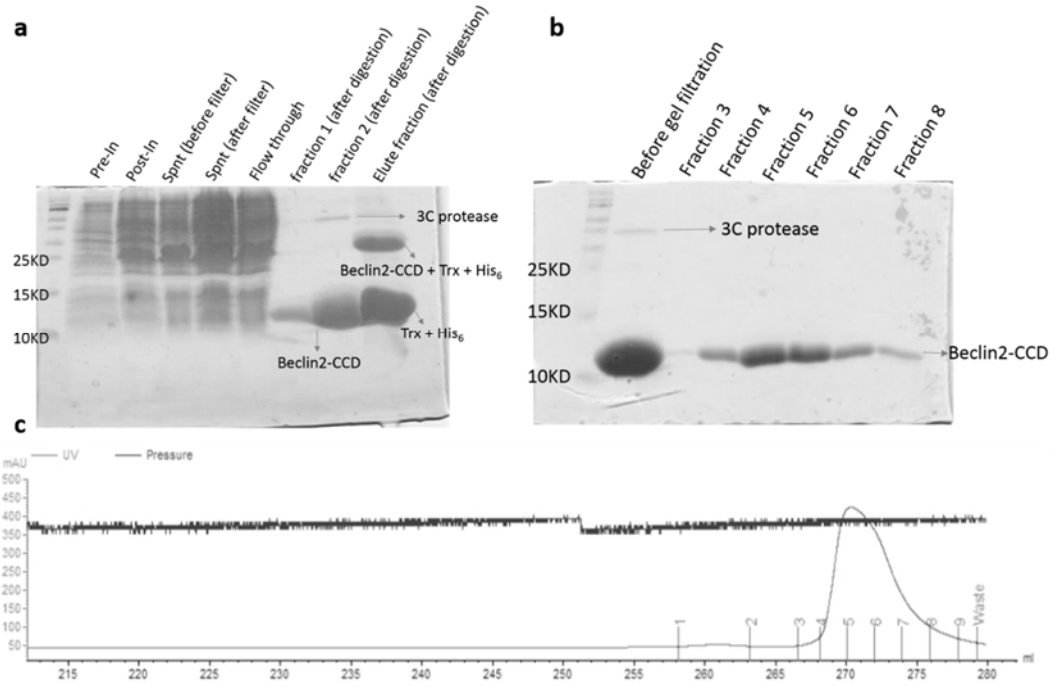

Figure 3.2 The purification and analysis of Beclin2 CC. a, SDS-PAGE analysis of protein expression and purification after affinity chromatography; **b**, SDS-PAGE analysis of Beclin2 CC purification by gel filtration; **c**, the UV absorbance profile depicting sample fractions separated by gel filtration column. Pre-In: pre-induction, the whole cell lysate before IPTG induction; Post-In: post-induction, the whole cell lysate after IPTG induction; Spnt: supernatant, supernatant of cell lysate after centrifugation; Flow through: Proteins unbind to the affinity column when loading sample; Fraction 1 and 2: protein sample washed from affinity column after on column 3C protease digestion.

3.2.3 Biochemical characterization of Beclin2 CC domain

3.2.3.1 Mass Spectrometric analysis

The amino acid sequence of Beclin2 CC after 3C digestion is listed as follows.

G P G S E A A A L R A E L R D L E L E E A R L V Q E L E D V D R N N A R A A A D L Q A A Q A E A A E L D Q Q E R Q H Y R D Y S A L K R Q Q L E L L D Q L G N V E N Q L Q Y A R V Q R D R L K E I N

Number of amino acids: 97; Molecular weight: 11113.1; Theoretical pI: 4.62; Extinction coefficients: 0.402. (Calculated by the web server ProtParam, http://web.expasy.org/protparam/).

The underlined amino acids “GP” on the far N-terminus represent the residues left by 3C protease digestion (specifically recognize amino acid sequence LEVLFQ↓GP), while the “GS” residues are encoded by the BamHI restriction enzyme site (nucleotides GGATCC).

The purified recombinant Beclin2 CC was then confirmed by mass spectrometry. As shown in Figure 3.3, the estimated molecular weight is 11114 Daltons, which quiet matches the theoretical molecular weight of Beclin2 CC.

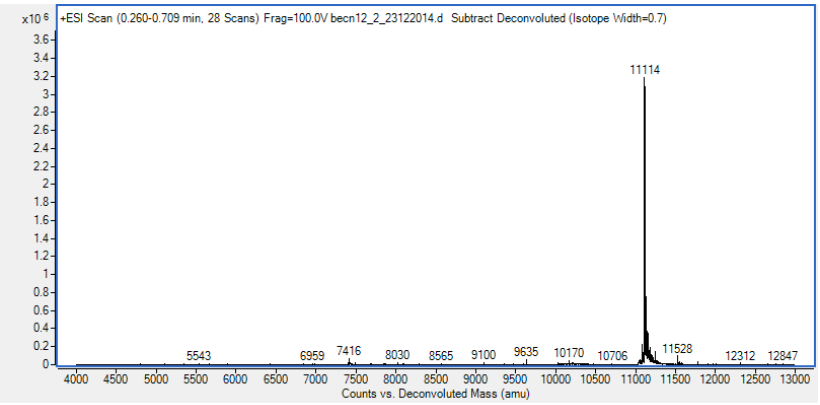

Figure 3.3 Mass spectrometric analysis of Beclin2 CC.

3.2.3.2 Beclin2 self-associates *in vivo* and the CC domain forms a homodimer

Our published experimental data identified the Beclin1 CC as a metastable homodimer, which can easily convert to more stable Beclin1-Atg14L or Beclin1-UVRAG heterodimer. We then investigated whether Beclin2 coiled coil domain exhibits a similar property. The self-association of Beclin2 was examined by immunoprecipitation, two tagged versions of Beclin2, namely, flag-Beclin2 and myc-Beclin2, were transfected into Hela cells, and co-IP assay was performed subsequently to test their association. As indicated in Figure 3.4, the presence of myc-Beclin2 in anti-flag immunoprecipitation assay suggests the self-association of Beclin2.

To further examine the self-association of Beclin2, the oligomeric state of Beclin2 CC was characterized by SEC-MALS. The LS profile of the purified Beclin2 sample yielded an estimated molecular weight of 23 kDa, nearly twice the theoretical

value of 11 kDa. This result suggests that Beclin2 CC forms a homodimer and is in good agreement with the dimerization of Beclin1 CC.

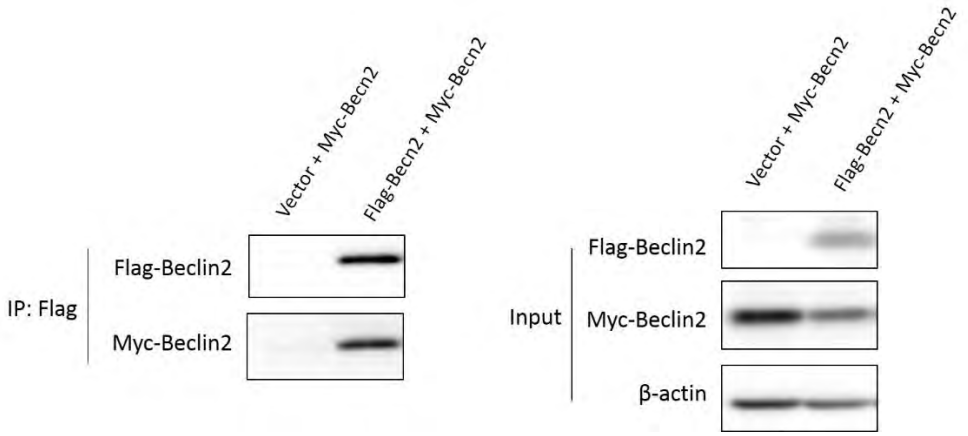

Figure 3.4 Co-immunoprecipitation and immunoblot analysis of protein lysates in Hela cells to detect Beclin2 self-association. Becn2: Beclin2.

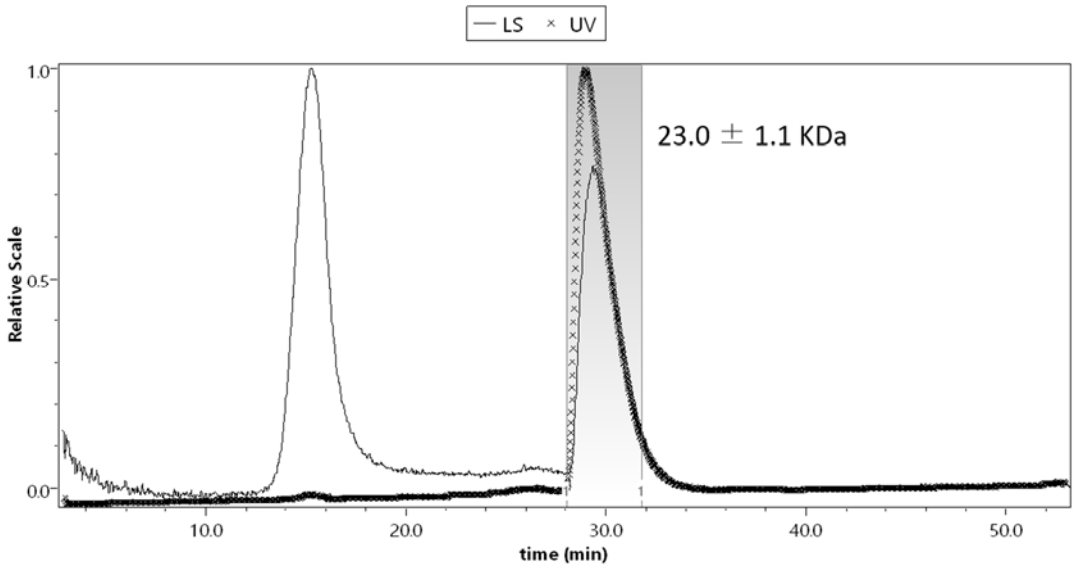

Figure 3.5 Molecular weight distributions of Beclin2 CC as determined in SEC-MALS. LS: light scattering signal; UV: UV signal.

3.2.3.3 Beclin2 CC homodimer is metastable

The assessment of Beclin2 CC homodimer stability was performed by measuring its circular dichroism (CD) profiles at a series of temperatures. The CD spectrum of Beclin2 CC at 20℃ reveals a characteristic pattern of helical structure with two negative peaks at 208nm and 222nm, respectively. However, with the temperature increased to 40℃ or even 60℃, the characteristic two minimum points gradually diminished, indicating the reduction of helical structures upon 40℃ (Figure 3.6). This low thermal stability of Beclin2 CC exhibited in CD spectra probably implies that the Beclin2 homodimer is naturally metastable under physiological temperature.

Subsequently, Isothermal Titration Calorimetry (ITC) method was applied to further characterize the metastability of Beclin2. By titrating the concentrated Beclin2 CC protein sample into buffer solution, the kinetics of its self-dissociation was measured. Similar to Beclin1, Beclin2 self-dissociated when titrated into Tris buffer, as indicated in Figure 3.7, the ITC profile shows endothermic self-dissociation with dissociation constant K_d around 138 μM, confirming its metastability. The ITC profile of Tris buffer titrated to Tris buffer served as the control here. Moreover, the self-dissociation constant K_d of the Beclin 1 CC domain homodimer is reported to be around 89 μM (Li et al., 2012), which suggests the stability of Beclin2 CC homodimer is slightly weaker than that of Beclin1. In summary, these studies lead to the conclusion that Beclin2 CC domain forms metastable homodimer *in vitro*.

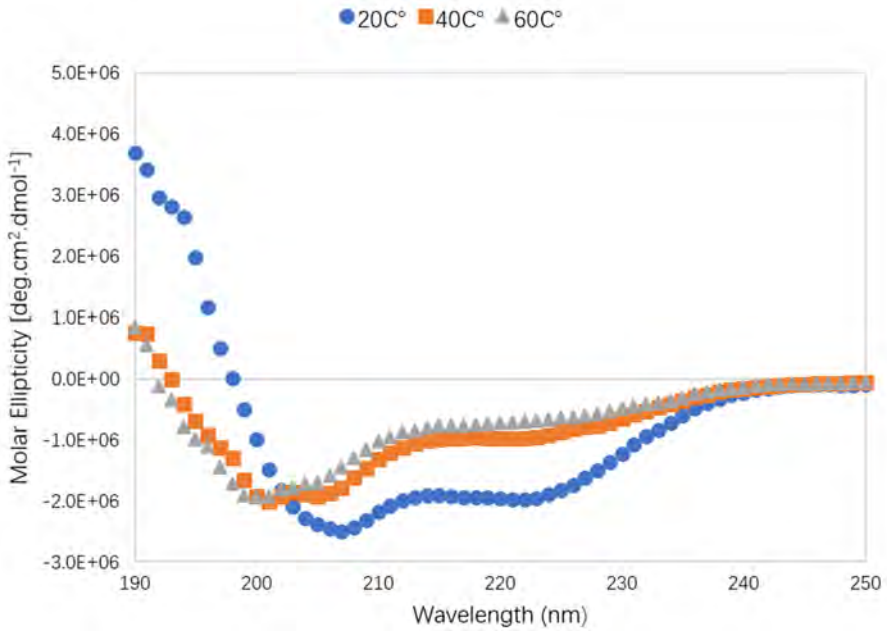

Figure 3.6 Circular Dichroism (CD) spectra of the Beclin2 CC domain at different temperatures.

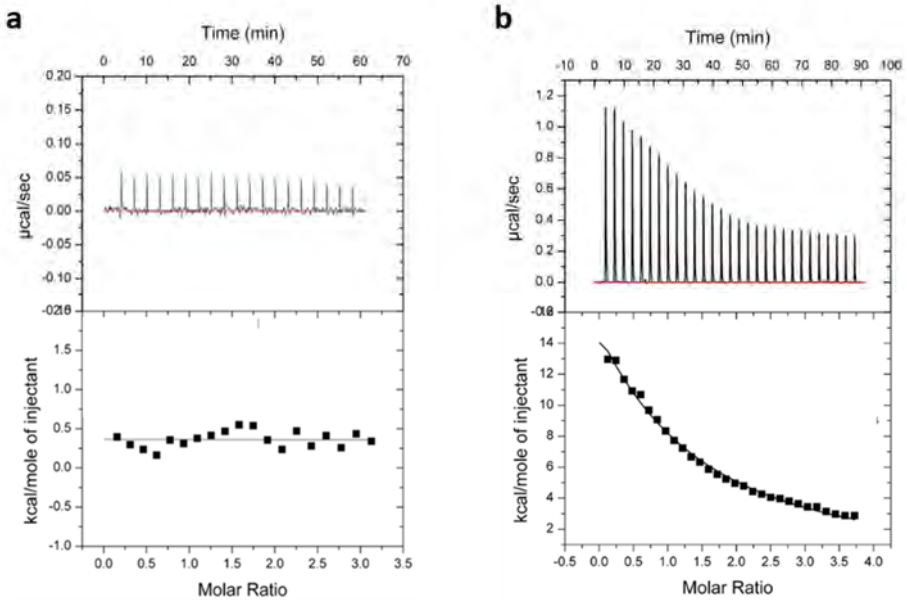

Figure 3.7 Determination of the Beclin2 CC self-dissociation by ITC assay. a, ITC profile of Tris buffer titrated to Tris buffer; **b**, ITC profile of Beclin2 CC titrated to Tris buffer.

3.2.4 Crystallization initial screening of Beclin2-CC

The process of the protein crystallization could be divided into two stages, screening and optimization. In the screening phase, a variety of reagent conditions, which are usually available from commercial crystal screening kits, are examined for crystal growth. Generally, parallel experiments with different protein concentration are also carried out to identify the crystallization conditions. Incubation temperature, despite its limited use, is another critical element in macromolecule crystallization. Based on the condition(s) determined in the screening stage, further optimization, if necessary, will be carried out subsequently to produce qualified crystals for x-ray analysis.

In this study, the purified and concentrated Beclin2 CC protein was subjected to crystallization studies using Crystal Screen, Crystal Screen 2 and Index from Hampton Research Company. All experiments were carried out in 24-well plates using the hanging drop vapor diffusion method as described in the methodology section, and each drop contains 1 µL of protein solution and 1 µL of reservoir solution.

The Beclin2 CC protein crystallized readily within a few days. As listed in Table 3.1, four distinct crystallization conditions (B1-B4) for Beclin2 CC were obtained from the screening stage. Referring to the initial crystallization conditions, optimization was then performed through refining a set of chemical parameters such as buffer pH

value and salt concentration, individually or in combination. Followed by x-ray crystallography measurements to check crystal diffraction patterns.

Table 3.1 Summary of the screened crystallization conditions for Beclin2 CC

Condition Code	Crystallization condition composition	Diffraction
B1	0.2M Magnesium acetate tetrahydrate, 0.1M Sodium cacodylate trihydrate pH6.5, 30% v/v 2-Methyl-2,4-pentanediol	No or poor diffraction
B2	0.2M Magnesium chloride hexahydrate, 0.1M HEPES sodium pH7.5, 30% v/v 2-Propanol	Two-dimensional crystals
B3	0.1M Sodium citrate tribasic dihydrate pH 5.6, 20% v/v 2-Propanol, 20% v/v PEG4000	No diffration
B4	1.5M $(NH_4)_2SO_4$, 0.1M Tris pH8.5, 12% v/v Glycerol	Salt crystals

The Beclin2 CC crystals grown from the optimized conditions and the corresponding x-ray diffraction images are shown in Figure 3.8. The x-ray diffraction image in Figure 3.8a suggests the crystal is actually an $(NH_4)_2SO_4$ crystal rather than that of Beclin2, as its diffraction spots are sporadic and mostly located at the outer

rim, a strong indication of a salt crystal. However, a diffraction pattern of a protein crystal is typically an array of spots across all resolution levels, in which diffraction spots of low resolution are located close to the central area, while those of high resolution extend to the outer space of the diffraction image. For the crystal in Figure 3.8b, there is no diffraction at all, while the crystal identity was confirmed to be the Beclin2 CC protein by SDS-PAGE and Coomassie blue staining (crystal #1 in Figure 3.8d). Another Beclin2 CC crystal shows limited diffraction in Figure 3.8c, and is validated to be Beclin2 CC protein by SDS-PAGE (crystal #2 in Figure 3.8d). However, its diffraction pattern fades away at some diffraction angle, suggesting the presence of crystal defects such as poor packing and irregular arrangement, which render it unfit for structure determination.

Although the Beclin2 CC construct readily yielded crystals, they only have poor or no x-ray diffraction patterns. Even though a wider range of crystallization conditions were tried for optimization, all crystals diffracted only to low or medium resolution. Therefore, a new set of Belcin2 CC constructs were designed with expectation to get the three-dimensional crystals of sufficient size to diffract x-ray.

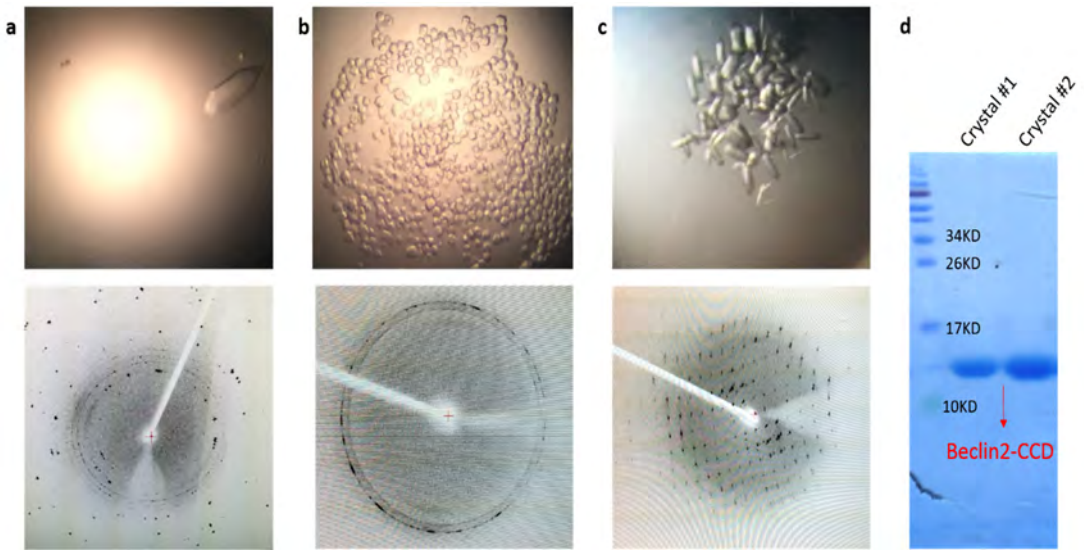

Figure 3.8 Crystals of Beclin2 CC protein and their corresponding x-ray diffraction images. a, the crystal obtained from modified condition B4 and its diffraction pattern; **b**, the Beclin2 CC crystal grown from modified condition B1 and its diffraction pattern; **c**, the Beclin2 CC crystal grown from modified condition B1 and its diffraction pattern; **d**, crystals were identified by SDS-PAGE. Crystal #1: crystals grown in the reservoir of **b**; Crystal #2: crystals grown in the reservoir of **c**.

3.2.5 Optimization of Beclin2 CC constructs

The initial Beclin2 CC construct was designed on the basis of its sequence similarity to the Beclin1 CC construct that was published by our lab previously. Given that preliminary Beclin2 CC crystals were obtained, only subtle changes were applied to optimize the Beclin2 CC construct. To further improve the diffraction power of the preliminary crystals, we made subtle changes to the original construct.

The initial construct (residues 158-250) starts at the residue Glu 158, and the CC

region is predicted to start at residue Ala 159, followed by a series of hydrophobic amino acids runs to residue Leu 162. To ensure that this secondary structure is not interrupted, which might be important for domain folding, and also increase the solubility, we chose to include one more additional residues at the starting point. In addition, the ending point is altered to Glu 248 rather than Asn 250 with prediction of increased solubility. The resulting new construct Beclin2 CC (residues 157-248) was also incorporated with mutants R209A, R243L, and R209AR243L, respectively (Table 3.2). Among these mutants, Beclin2 R209A intends to improve the crystal packing, on the basis on its similarity to Beclin1. And Beclin2 R243L mutant was designed with intention to improve dimer stability. Typically, coiled coil structures contain a highly characteristic sequence motif known as a heptad repeat, in which the motif repeats itself every seven residues (abcdefg) along the sequence, where “a” and “d” positions are occupied by hydrophobic amino acids to stabilize the coiled coil structure by Van der Waals interactions. In this regard, we assume that the charged residue R243 on the “a” position impairs the stability of Beclin2 homodimer, and a mutation of this residue to leucine with increased stability may help to improve crystallization. The third mutant is a combination of the previous two mutated sites, which is expected to feature better packed and higher stability, therefore be more likely to result in better diffracting crystals.

Table 3.2 Summary of the new constructs design and rationale

Construct	Rationale for construct design
Beclin2 CC (residues 157-248)	To avoid interrupting the secondary structure
Beclin2 R209A	To improve the crystal packing
Beclin2 R243L	To stabilize the dimeric interface
Beclin2 R209AR243L	To improve the packing and the dimer stability

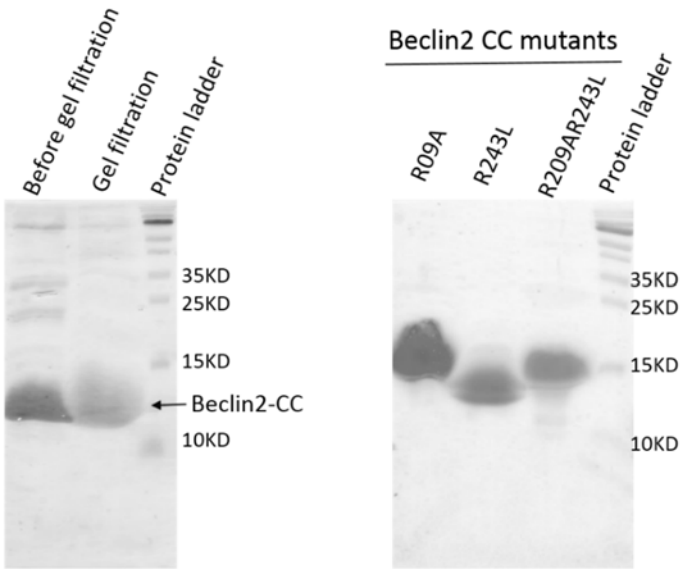

Figure 3.9 SDS-PAGE of novel Beclin2 CC protein (residues 157-248) and its mutants.

These four Beclin2 CC variants were constructed following the same protocol described in the methodology section. All variants yielded large amounts of pure protein after the multistep purification process, including affinity chromatography, fusion tag-cleavage and gel filtration. Crystallization screening yielded crystals within one week for all constructs. Beclin2 CC (157-248) behaved similarly with Beclin2 CC (158-250). Beclin2 R209A and R209AR243L led to crystals at a variety of conditions, but most of them were tiny crystals with poor diffraction. Lastly, Beclin2 R243L exhibited the nicest three-dimensional crystals at the condition of 1.6M ammonium sulfate, 0.1M MES, pH6.5, and 10% Dioxane.

3.2.6 Crystallographic studies of Beclin2 CC domain

With Beclin2 R243L yielding good-quality crystals after initial crystallization screening, further optimization and refinement were pursued. Eventually, crystals could readily grow to ~200 μm in size in about a week and diffracted to ~ 2.4 Å at home x-ray source. The space group is C2221 with unit cell dimension of (47.36 Å, 143.45 Å, 139.04 Å, 90°, 90°, 90°). A native data set to 2.0 Å was collected at Shanghai synchrotron source (Figure 3.10).

3.2.7 Phase determination

Multiple isomorphous replacement (MIR) is preformed subsequently to estimate the phase. Specifically, the native crystal of Beclin2 R243L was soaked into

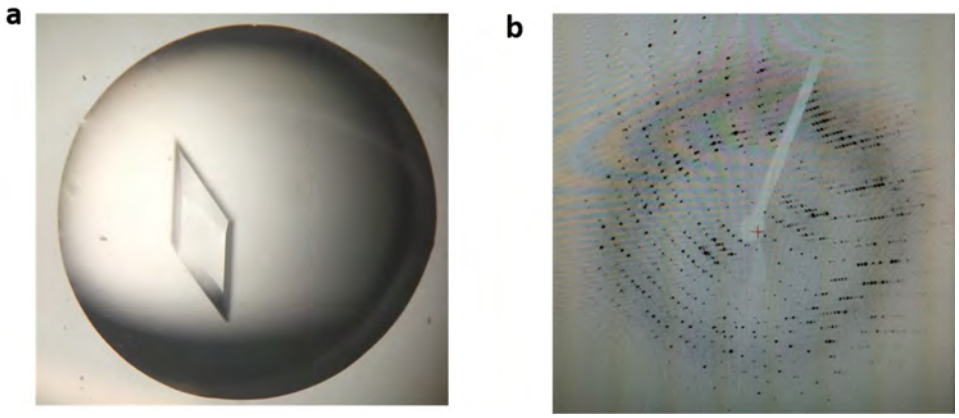

Figure 3.10 Crystal of Beclin2 R243L protein (a) and its corresponding X-ray diffraction image at Shanghai synchrotron (b).

its buffer condition in supplement with heavy atoms, for instance, iodine, gold, or mercury. With expectation that these heavy ions may bind to the protein crystal without conformational changes, the difference of diffracting data between native and isomorphpous derivative crystals could serve as a clue to calculate the phase angle. Unfortunately, thus far, none of such derivative data is collected after extensive trials, as these heavy ions did not soak into crystals.

Another method that is widely applied to determine phase is multiwavelength anomalous diffraction (MAD). One common way to conduct such experiment is to replace methionine residues among the sequence to selenomethionine residues. However, since Beclin2 CC domain lacks methionine in its sequence, two mutant

constructs, with Q222M and L236M mutations respectively, were engineered to incorporate a single Met residue into the CC domain. The expression and purification of two selenomethionyl Beclin2 mutants were almost identical with the native one, except for using the Se-Met growth media kit as demonstrated by the manufacturer (Medicilonic). Purified selenomethionyl Beclin2 mutants, as shown in Figure 3.11, were then subjected to crystallization screening as previously described.

After initial crystallization screening, the L236M mutant produced many nice-looking, three-dimensional crystals within one week as shown in Figure 3.12, while the Q222M mutant only yielded tiny crystals that were too small for x-ray diffraction test. Subsequently, selenomethionine substituted Beclin2 L236M crystals grown from a variety of buffer conditions were tested at laboratory x-ray source, with high resolution limit to ~ 2.4 Å. Of note, the nicest selenomethionyl protein crystal with good-diffracting property was obtained from the same solution condition where its native counterpart was grown (1.6M ammonium sulfate, 0.1M MES, pH6.5, and 10% Dioxane). Furthermore, two datasets diffract up to 2.3 Å was collected in Shanghai Synchrotron Radiation Facility (SSRF) at the wavelength of 0.97946 Å, their diffracted patterns are shown in Figure 3.13. The dataset processing was performed as described in methodology, and the data is reliable to 2.5 Å with reasonable statistics (Table3.3). The Crystal displayed space group C2221 with unit cell dimension of (47.33 Å, 143.43 Å, 146.19 Å, 90°, 90°, 90°). The presence of four molecules in the

asymmetric unit gives a solvent content of 56%.

The initial phase was obtained using the Autosol in Phenix suite of programs (Adams et al., 2002), with four selenium atoms were found in an asymmetric unit. Then model building was preformed through the Autobuild program in Phenix (Terwilliger et al., 2008), whereas the obtained model is of poor quality with R_{work} value 39.8%. In an attempt to improve phase and the building model, the obtained model was used as reference model, and the native dataset of Beclin2 CC was applied for molecular replacement by CCP4 package. This strategy resulted in a better model, after refinement by REFMAC and manual correction in COOT program (Emsley and Cowtan, 2004), the final atomic model was achieved with R_{work} = 21.6%, and R_{free} = 25.8%.

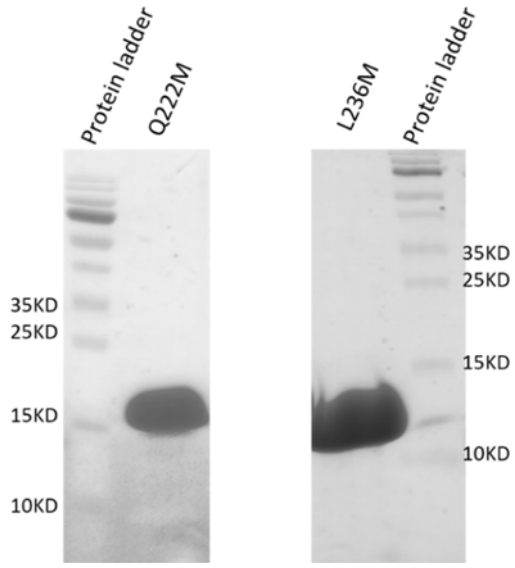

Figure 3.11 SDS-PAGE of selenomethionyl Beclin2 CC mutants.

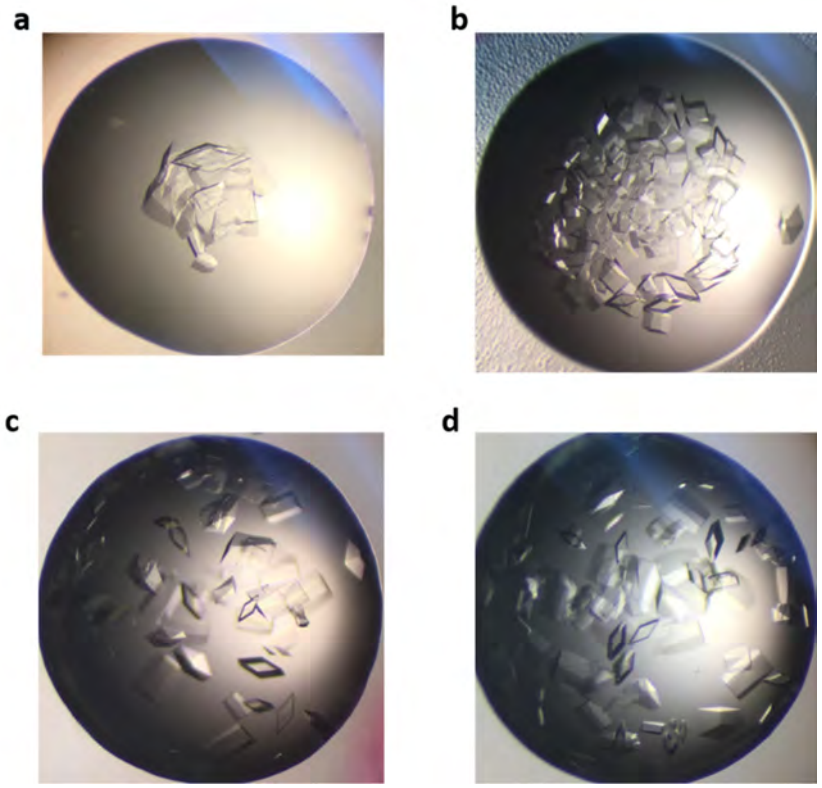

Figure 3.12 Crystals of selenomethionyl Beclin2 CC L236M mutant after initial crystallization screening. **a**, crystals obtained from solution condition of 0.2M Ammonium phosphate monobasic, 0.1M Tris pH8.5, and 50% v/v 2-Methyl-2,4-pentanediol; **b**, crystals grown from solution condition of 0.2M Ammonium acetate, 0.1M Sodium citrate tribasic dehydrate pH5.6, and 30% v/v 2-Methyl-2,4-pentanediol; **c & d**, crystals grown from solution condition of 1.6M ammonium sulfate, 0.1M MES, pH6.5, and 10% Dioxane.

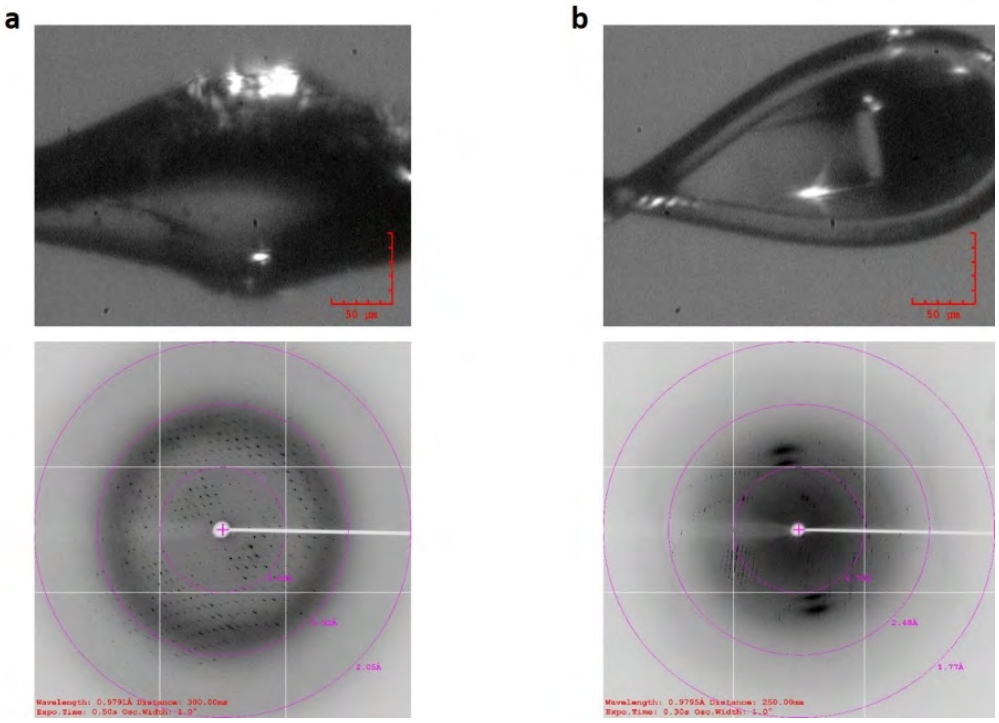

Figure 3.13 Crystals of selenomethionyl Beclin2 L236M mutant and their diffraction patterns in Shanghai synchrotron. a, the crystal obtained from solution condition of 0.2M Ammonium acetate, 0.1M Sodium citrate tribasic dehydrate pH5.6, and 30% v/v 2-Methyl-2,4-pentanediol; **b**, the crystal grown from solution condition of 1.6M ammonium sulfate, 0.1M MES, pH6.5, and 10% Dioxane.

Table 3.3 Crystallographic data processing and refinement statistics for Beclin2 CC

	R243L	Se-Met
Data collection		
Space group	$C222_1$	$C222_1$
Cell dimensions		
a, b, c (Å)	46.33, 143.46, 143.86	47.10, 143.33, 146.16
α, β, γ (°)	90, 90, 90	90, 90, 90
Resolution ^	71.92- 2.00 (2.10-2.00)	73.06 -2.50 (2.64-2.50)
R_{sym} or R_{merge} *	10.2% (30.6%)	11.2% (28.4%)
$I / \sigma I$ *	17.7 (8.6)	15.8 (7.1)
Completeness (%) *	99.7 (99.7)	99.8 (99.9)
Redundancy *	13.3 (12.8)	13.6 (14.2)
Refinement		
Resolution (Å)	71.59 -2.00	
No. reflections	50442	
R_{work} / R_{free}	21.6%/25.8%	
No. atoms		
Protein	2946	
Ligand/ion	N/A	
Water	131	
B-factors		
Main chain	21.18	
Side chain	28.75	
Water	28.08	
R.m.s deviations		
Bond length (Å)	0.020	
Bond angle (°)	1.799	

^ Numbers in parenthesis define the highest resolution shell of data.

* Numbers in parenthesis are the statistics for the highest resolution shell of data.

3.2.8 Beclin2 coiled coil domain structure

Eventually, the Beclin2 CC crystal structure was solved as shown in Figure 3.14. The structure is an anti-parallel CC homodimer with two helices wrapped around each other in head-to-tail fashion. Each crystallographic asymmetric unit contains four chains, which is equivalent to two identical pairs of coiled coil homodimers. The full length of the Beclin2 CC chain (from residue 156 to residue 246) is around 130 Å, and the molecular surface is mostly negatively charged as reflected by its electrostatic surface charge distribution map (Figure 3.14).

In general, the sequence of Beclin2 CC chain follows the hallmark of coiled coil structure. Each chain contains 13 heptad repeats, with each repeat denoted as “abcdefg” in Figure 3.15. According to canonical coiled coil structures, hydrophobic residues are usually found at the “a” and “d” positions to form energetically favorable pairings at the coiled coil interface, while charged residues are usually found at the “e” and “g” positions to form interhelical and intrahelical electrostatic interactions. Collectively, these hydrophobic and electrostatic interactions contribute to stabilizing the coiled coil architecture.

For the anti-parallel Beclin2 homodimer, the first heptad repeat (residues 159-165) of chain A packs against the 13th heptad repeat of chain B (residues 243-248), and residues at positions “a” of chain A packs against residues position “d” on the

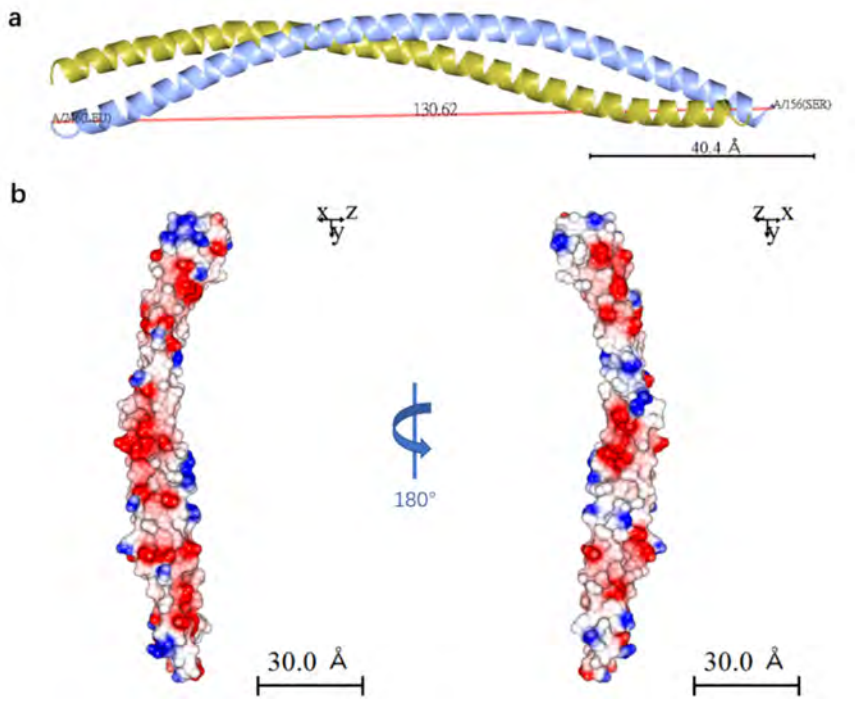

Figure 3.14 The crystal structure of Beclin2 CC domain. a, the full length of Beclin2 CC anti-parallel homodimer structure is around 130 Å; **b**, The distribution of electrostatic charges on Beclin2 CC homodimer surface.

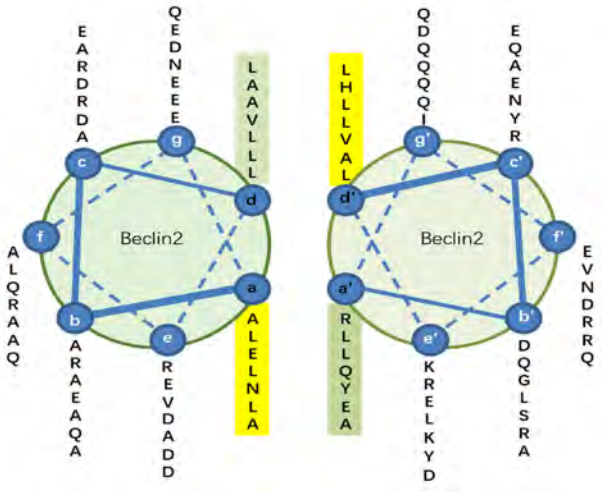

Figure 3.15 Helical wheel presentation of the 13 heptad repeats in Beclin2 coiled coil domain. Only 7 heptad repeats are mapped, representing the unique half of the anti-parallel homodimer with a-d' pairings at the dimer interface.

chain B to form a-d' packing (Figure 3.16). As indicated in Figure 3.17, among the thirteen a-d' hydrophobic interacting pairs at the dimer interface, 6 pairs are "canonical" pairings because they contain hydrophobic residues that form strong Van del Waals interactions at the interface to stabilize the dimer. Specifically, the 6 canonical pairings include three pairs of ideal "leucine zipper" (L169-L236, L176-L229, L180-L225), and three acceptable Leu-Ala pairs (A159-L246, L166-A239, A201-L204) (Figure 3.17a). In fact, Beclin1 and Beclin2 share three identical Leucine zippers that strongly stabilize their anti-parallel CC interface. However, careful analysis reveals that Beclin1 homodimer consists of 7 canonical a-d' pairings, while Beclin2 possess only 6 canonical pairings. This difference in number may correlate with our previous observation that the Beclin2 homodimer is slightly less stable than Beclin1 (K_d 138μM versus 89μM).

Besides six canonical pairings, 7 pairs are considered as "imperfect" pairings with bulky polar even charged amino acids at either the "a" or "d" positions. For "imperfect" pairings, there are four of them that contain charged residues (E173-V232, E208-A197, H211-L194, R243-L162), and the remaining three pairs contain polar residues like Gln (Q222-V183), Tyr (Y215-A190) and Asn (N187-L218). In addition, polar contacts also contribute to stabilize the CC structure by forming intrahelical and interhelical hydrogen bonds. There are three intrahelical polar interactions (R175-E179, R213-S216, K219-Q222) and one pair of interhelical polar

interaction, which D184 of one chain forms hydrogen bond with Q222 of the other chain. In summary, the structure of Beclin2 coiled coil domain is consistent with our biochemical studies in forming a metastable homodimer with multiple “imperfect” interfacial interactions (Figure 3.17b).

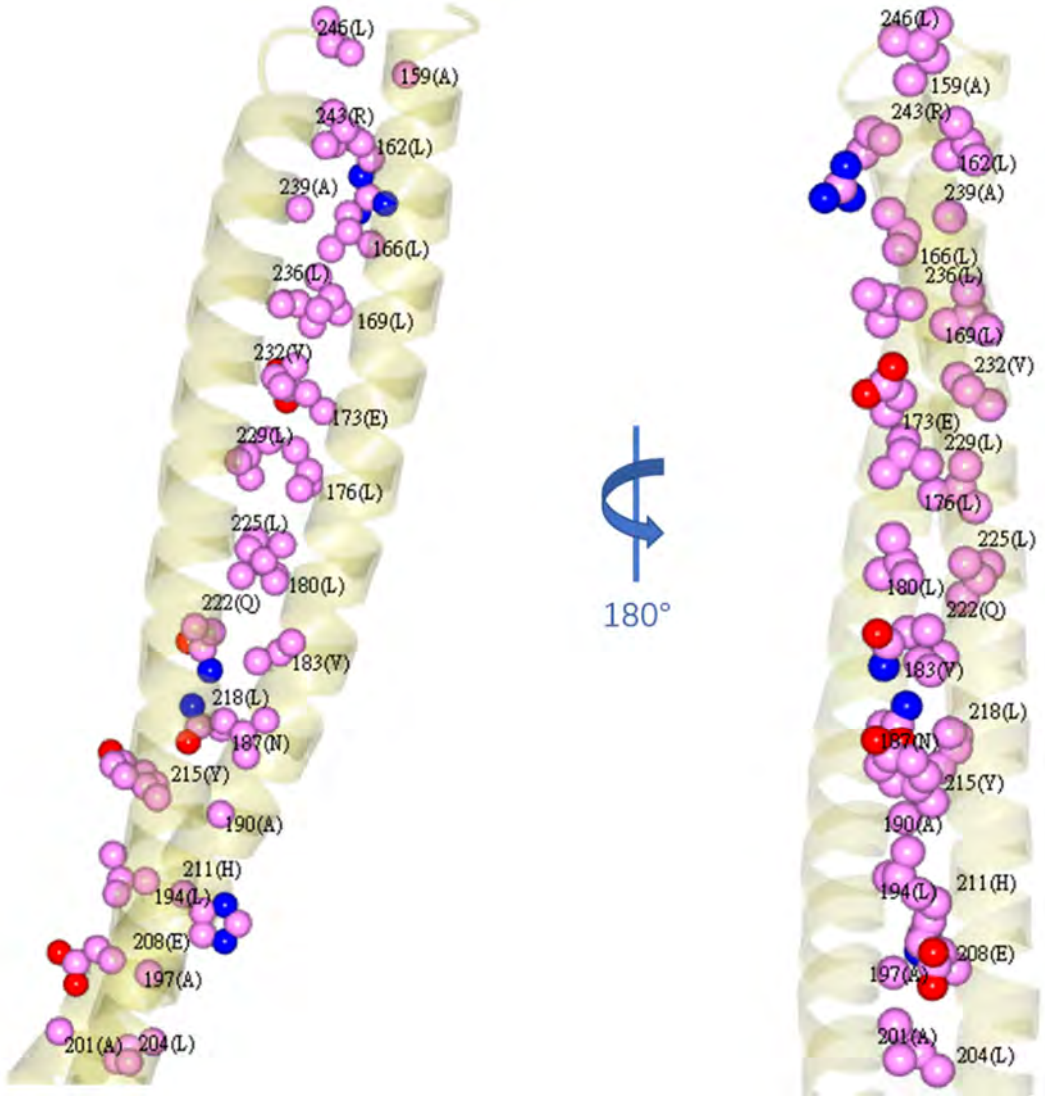

Figure 3.16 Atomic details of 13 a-d’ pairings at the interface of Beclin2 homodimer. Atoms of side chains are represented as spheres.

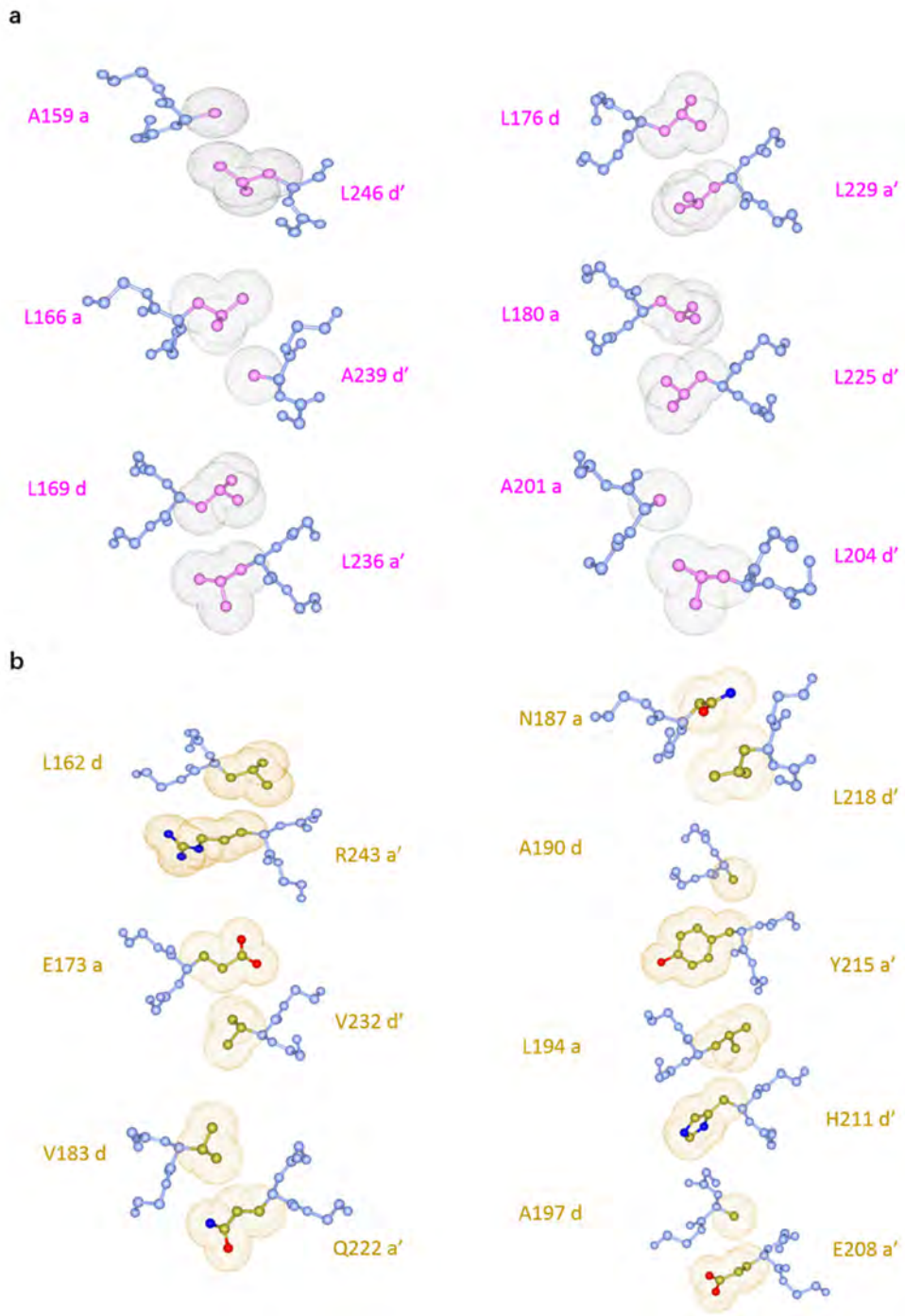

Figure 3.17 Close-up view of the canonical (a) and imperfect (b) a - d' pairings in Beclin2 CC. Each residue is illustrated in ball-and-stick model. Main-chain atoms are colored blue and side-chain atoms are colored pink for canonical pairings or golden for imperfect pairings. The a - d' packing is illustrated by Van der Waals spheres depicting the side-chain atoms.

3.2.9 Biochemical distinction between Beclin1 and Beclin2 coiled coil domain structures

The structure of Beclin2 CC domain was then compared with that of Beclin1 CC domain (PDB code 3Q8T) via Superpose program in CCP4. The three-dimensional superposition of these two structures gives a root mean square deviation (RMSD) value of 2.56 Å for 175 residues aligned. This result shows the difference between these two structures, likely explains that why the original phasing attempt by the molecular replacement was not successful despite high sequence identity.

We next ask whether these two homologs would interact with each other. The potential of such interaction was examined by *in vitro* ITC experiments and immunoprecipitation assay. As reflected by the ITC results in Figure 3.18 a&b, no cross-association between Beclin1 and Beclin2 coiled coil regions was detected. For immunoprecipitation assay, as indicated in Figure 3.19, the GFP tagged Beclin1 immunoprecipitated with endogenous Beclin1, while GFP tagged Beclin2 did not, suggesting that despite high sequence similarity, Beclin1 and Beclin2 could not interact with each other *in vivo*, matching the results from *in vitro* binding studies.

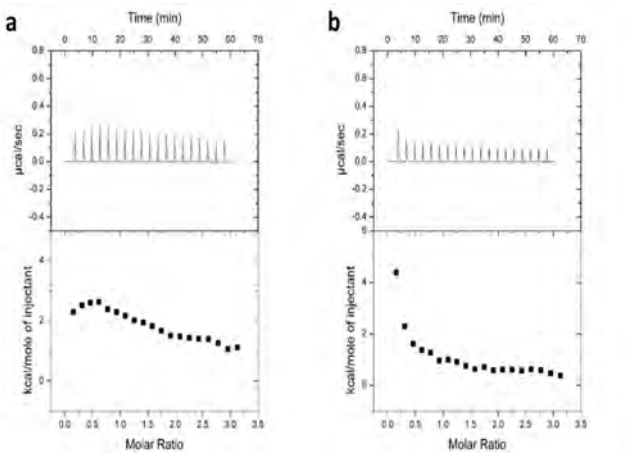

Figure 3.18 Determination of the mutual cross-association between Beclin1 CC and Beclin2 CC by ITC experiments. a, The ITC profile of Beclin2 CC titrated to Beclin1 CC; **b**, The ITC profile of Beclin1 CC titrated to Beclin2 CC;

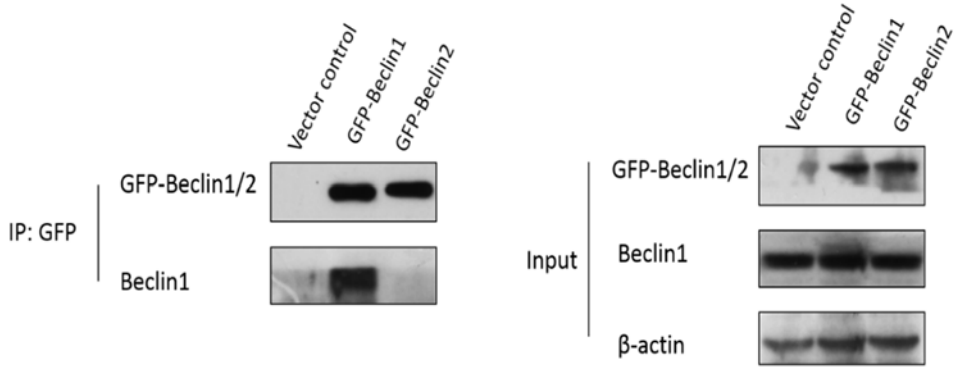

Figure 3.19 Determination of the mutual cross-association between Beclin1 and Beclin2 by immunoprecipitation.

To explain this phenomenon, we generated a model of the Beclin1-Beclin2 heterodimer by replacing one chain within the Beclin1 homodimer with that of Beclin2 (Figure 3.20). First of all, in our model of the Beclin1-Beclin2 heterodimer complex, 13 canonical hydrophobic pairings are found at its coiled coil interface,

while 14 pairs in Beclin1 homodimer, and 12 pairs in Beclin2 homodimer. In fact, Beclin1 homodimer interface and Beclin1-Beclin2 heterodimer interface share 6 identical Leucine zipper pairs. Additionally, charged residues at the “e” and “g” positions of the Beclin1-Beclin2 model form no interhelical repulsive interactions to destabilize the complex, again similar to the Beclin1/Beclin2 homodimers.

However, Beclin2 contains residue R243 at a position that would form a seriously “imperfect” pairing with L162 in Beclin2 homodimer interface, or with L178 in the Beclin1-Beclin2 heterodimer model. In contrast, Beclin1 homodimer contains a perfect Leu zipper pair at corresponding position. This difference may render the Beclin1-Beclin2 heterodimer less favorable as compared to the Beclin1 homodimer.

In comparison with Beclin2 homodimer, the Beclin1-Beclin2 heterodimer contains one more canonical hydrophobic pairing. On the other hand, the Beclin1-Beclin2 heterodimer is also less favorable than the Beclin2 homodimer because the Ala159-Leu246 pairing in Beclin2 would be replaced by Ser 175-Leu246 pairing (Ser175 of Beclin1 would replace the Ala159 of Beclin2), which is slightly less “perfect”. In this regard, it is hard to compare the stabilities of these two dimers based on our model driven analysis. Experimental investigation is required to evaluate such analysis, for example, the mismatched residues in Beclin2 could be mutated into the matching types of Beclin1 to see if Beclin1-Beclin2 cross interaction can be detected.

In addition, it has been reported that minor difference or replacement in residues, even though forming favorable hydrophobic interactions, could affect the orientation, oligomeric state and specificity of coiled coil structures (Grigoryan and Keating, 2008; Hadley et al., 2008). Furthermore, although interactions among “a-d”, and “e-g” residues account for most structural stability in coiled coils, the influence of “b”, “c” and “f” positions have long been controversial, and this aspect of knowledge is poorly understood at present.

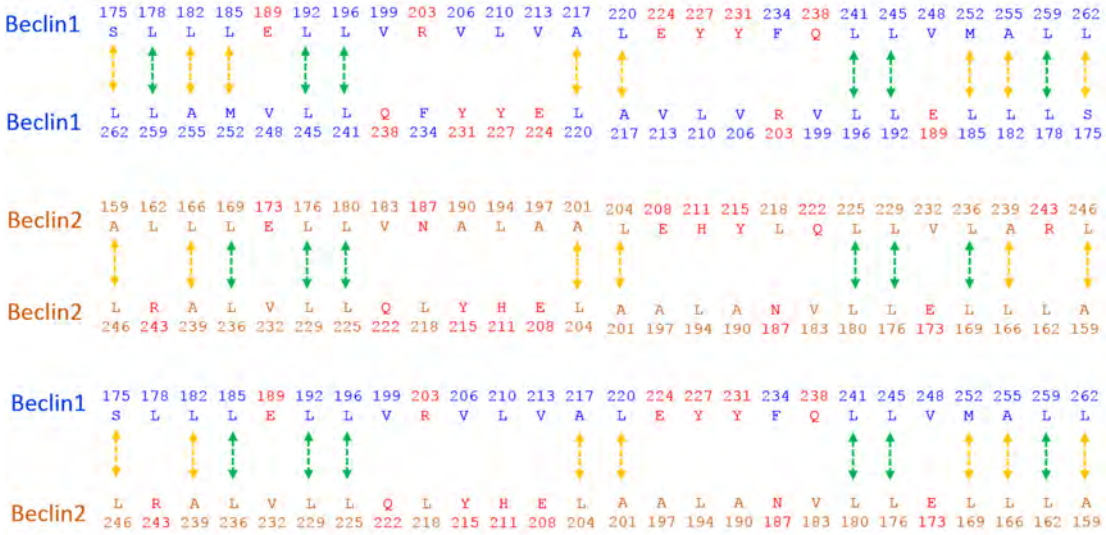

Figure 3.20 Comparison of the coiled coil interfaces of Beclin1 homodimer, Beclin2 homodimer and modelled Beclin1- Beclin2 heterodimer. The charged or polar residues at the sequence are colored in red. The arrows indicate the canonical hydrophobic pairings at the interface. Green arrows mark the strongly hydrophobic “leucine zippers”; yellow arrows mark the moderately hydrophobic pairings.

Chapter Four: Biochemical Analysis of Beclin2-Atg14L Interaction

4.1 Overview

The conserved nature of CC domain of Beclin1 and Beclin2 implies that Beclin2 may interact with similar interactors of Beclin1. In this chapter, the interactions between Beclin2 and Atg14L/UVRAG via CC assemblies were investigated using isothermal titration calorimetry (ITC), which is applied extensively to measure the thermodynamic changes caused by the biochemical reaction between macromolecules. The CC fragments of these proteins with high purity and quality are required for ITC studies. However, Unlike the well-defined boundary for the coiled coil domain of Beclin1 and Beclin2, the exact start and end points for the Atg14L and UVRAG coiled coil region are not easy to pinpoint due to their weak sequence pattern of canonical heptad repeats in the form of “abcedfg” with hydrophobic residues expected at positions “a” and “d”. Through extensive screening in our previous studies, a soluble coiled coil fragment from UVRAG (residues 228-298) that can bind to the Beclin1 coiled coil domain effectively was identified.

As for Atg14L, it was reported that there are three potential CC regions presenting in the N-terminal half of Atg14L, as predicted by the program COILS. They are amino acids 71-101, 107-127, and 141-180 respectively (Matsunaga et al., 2009). Deletion analysis of Atg14 in yeast Saccharomyces cerevisiae suggests that the N-

terminal tail containing these coiled-coil fragments is required for autophagy modulation, including the ability to form the PI3KC3 complex, and to localize on isolation membranes or its precursor structures (Obara et al., 2006). The second coiled-coil domain is believed to be essential for the interaction with Atg6 (Beclin1 homolog), while both the first and the second are involved in the interaction with Vps34. Apart from these CC regions, there is also a cysteine-rich region in the far N-terminus of Atg14L, which is found to be critical for the proper localization of Atg14L (Obara and Ohsumi, 2011), and plays a role in the membrane tethering as recently reported (Diao et al., 2015). In the initial investigation of Beclin2-Atg14L interaction, the Atg14L construct (residues 88-179) was applied.

4.2 Experimental Results

4.2.1 Purification of Beclin1, Atg14L and UVRAG coiled coil regions

For biochemical characterization of the Beclin2-Atg14L/UVRAG interaction, as well as for comparing it to the homologous Beclin1-Atg14L/UVRAG interaction, recombinant proteins for the coiled coil region of Beclin1, Atg14L and UVRAG were individually expressed and purified from *E. coli* according to the procedure in our previous study (Figure 4.1). Information of these constructs is listed in Table 4.1. All protein samples used for ITC experiments were dissolved in Tris buffer (50mM Tris, 150mM NaCl, pH 8.0) unless otherwise specified.

Table 4.1 Summary of Beclin1 CC, Atg14Ls2 and UVRAG constructs information.

Construct name	Length	Vector (fusion tag)	Theoretical Mw (after fusion tag cleavage)
Beclin1 CC	174-266	pETM (His_6)	11597.8
Atg14Ls2	88-179	pET49m (GST+ His_6)	11449.2
UVRAG	228-298	pET32m (Trx + His_6)	8517.7

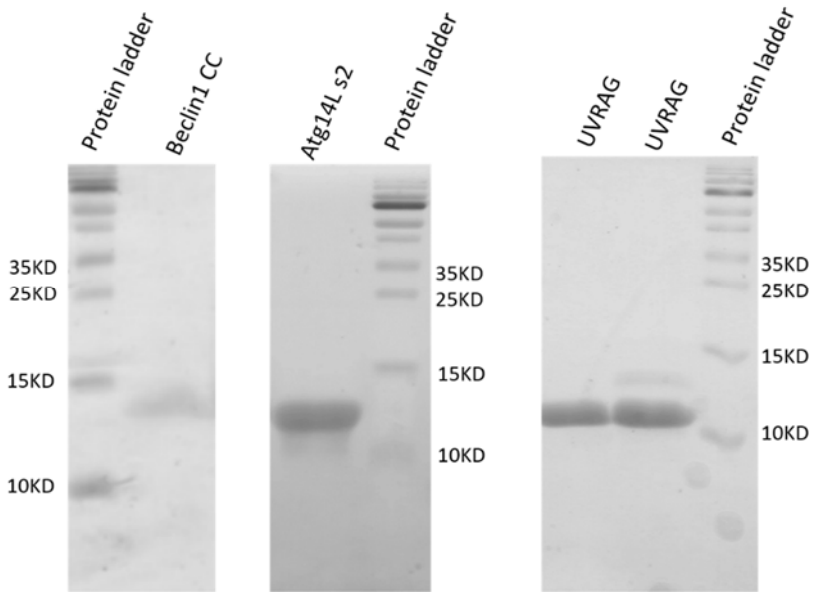

Figure 4.1 SDS-PAGE analysis for coiled coil fragments of Beclin1, Atg14L and UVRAG. All proteins were purified by the combination of affinity chromatography and gel filtration chromatography, and fusion tags were removed during purification.

4.2.2 Beclin2 interacts with Atg14L and UVRAG via coiled coil domain

Our previous studies have shown that Atg14L and UVRAG bind to Beclin1 CC domain in mutually exclusive manner to form functionally distinct PI3KC3 complexes I and II that are essential for the autophagy process. Here we would like to examine whether similar binding pattern is observed for Beclin2-Atg14L/UVRAG CC regions. The ITC profiles suggest that Beclin2 binds to both Atg14L and UVRAG in an exothermic reaction manner, with a stoichiometry of 1:1 (Figure 4.2 a&c). Reverse titrations (reversing the role of ligand and molecule in sample cell) were carried out to confirm the interactions (Figure 4.2 b&d). These results confirm that, similar to

Beclin1, Beclin2 can form strong interactions with Atg14L and UVRAG. The K_d value for Beclin2-Atg14L interaction is ~0.7 μM, while the K_d of Beclin2-UVRAG is ~10.0 μM. These values suggest that Beclin2 binds to Atg14L coiled coil region stronger than UVRAG. Interestingly, in our previous study, Beclin1 shows stronger binding affinity to UVRAG than to Atg14L (Li et al., 2012).

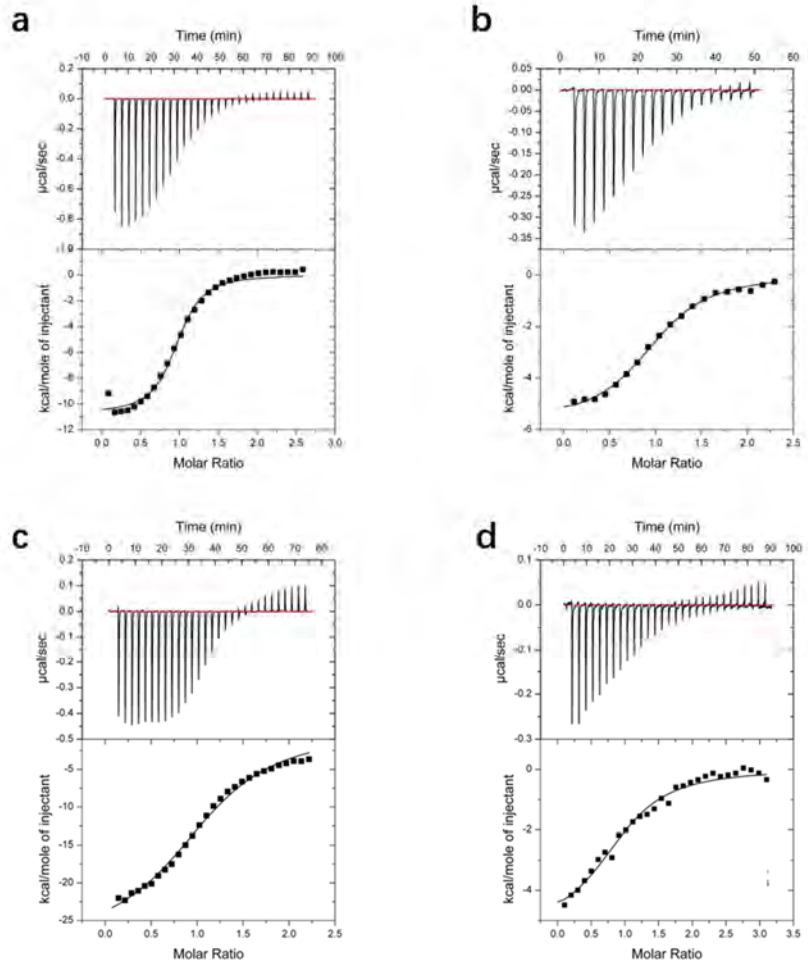

Figure 4.2 Determination of the interaction between Beclin2 CC and Atg14Ls2/UVRAG. a, ITC profile of Beclin2 CC titrated to Atg14Ls2; **b**, ITC profile of Atg14Ls2 titrated to Beclin2 CC; **c**, ITC profile of Beclin2 CC titrated to UVRAG; **d**, ITC profile of UVRAG titrated to Beclin2 CC;

Previous studies of our lab reported that the interaction between Beclin1 and Atg14L/UVRAG is largely weakened even abolished under high-salt buffer containing 1M NaCl, suggesting the importance of electrostatic interaction in maintaining the Beclin1-Atg14L/UVRAG complex (Li et al., 2012). Furthermore, the Beclin1-UVRAG complex structure recently solved in our lab reveals both hydrophobic and electrostatic interactions at the coiled coil interface (manuscript to be submitted). To test whether electrostatic interactions help to stabilize Beclin2-Atg14L/UVRAG interaction, we measured its binding affinity under high-salt conditions. Interestingly, high-salt conditions, represented by 1M NaCl or even 2M NaCl, weakened the Beclin2-Atg14L/UVRAG interaction without completely abolishing it (Figure 4.3). In comparison with the normal buffering system, the K_d value for Beclin2-Atg14L association decreases to 26.9 μM in 1 M NaCl and to 42.2 μM in 2 M NaCl. As for Beclin2-UVRAG, the K_d value is 23.7 μM in 1 M NaCl, and 40.3 μM in 2 M NaCl. These results suggest that the Beclin2-Atg14L/UVRAG interaction may have stronger hydrophobic effect than the homologous Beclin1-Atg14L/UVRAG interaction. Notably, Beclin2-UVRAG interaction seems less sensitive to high-salt conditions than Beclin2-Atg14L, as its binding affinity is largely maintained.

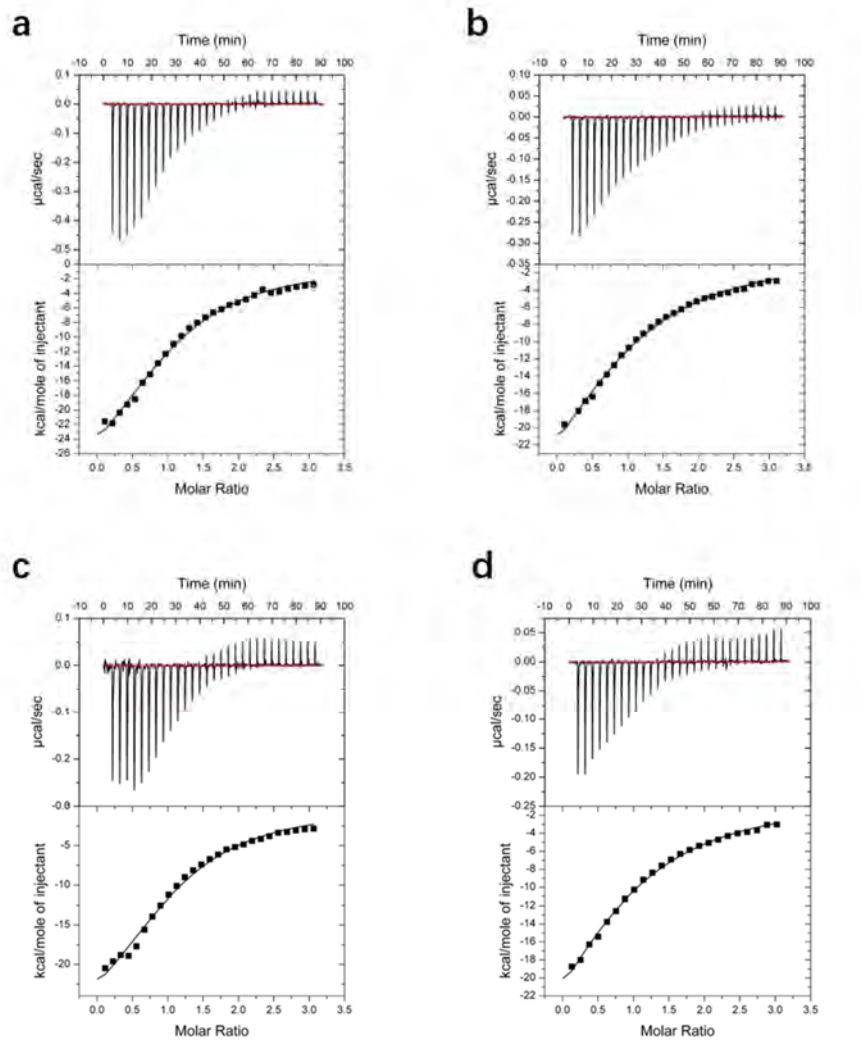

Figure 4.3 The interaction of Beclin2-Atg14L/UVRAG under high-salt conditions. a&b, Determination of the Beclin2 CC and Atg14Ls2 interaction at high-salt buffer conditions. **a**, ITC profile of Beclin2 CC titrated to Atg14Ls2 at Tris buffer containing 1M NaCl. **b**, ITC profile of Beclin2 CC titrated to Atg14Ls2 at Tris buffer containing 2M NaCl. **c&d**, Determination of the Beclin2 CC and UVRAG interaction at high-salt buffer conditions. **c**, ITC profile of Beclin2 CC titrated to UVRAG at Tris buffer containing 1M NaCl. **d**, ITC profile of Beclin2 CC titrated to UVRAG at Tris buffer containing 2M NaCl.

4.2.3 Atg14L and UVRAG are two mutually exclusive binding partners of Beclin2

To further compare the biochemical properties of Beclin2 versus Beclin1 in terms of binding to Atg14L and UVRAG, a series of competitive binding assays were carried out. We first used competitive ITC experiments to re-evaluate the binding affinity of Beclin2 to Atg14L and UVRAG. As indicated in Figure 4.4, competitive binding assays performed by ITC reveal that Atg14L can competitively bind to Beclin2 in presence of saturating amount of UVRAG, but not vice versa. These results suggest that the Atg14L and UVRAG are mutually exclusive binding partners of Beclin2, and the Beclin2-Atg14L interaction is more potent than the Beclin2-UVRAG interaction. This finding is consistent with our previous ITC data that directly compared the K_d values of these two interactions. The possibility of UVRAG-Atg14L interaction can be ruled out because no direct interaction was observed between UVRAG and Atg14L according to the previously reported data (Sun et al., 2008).

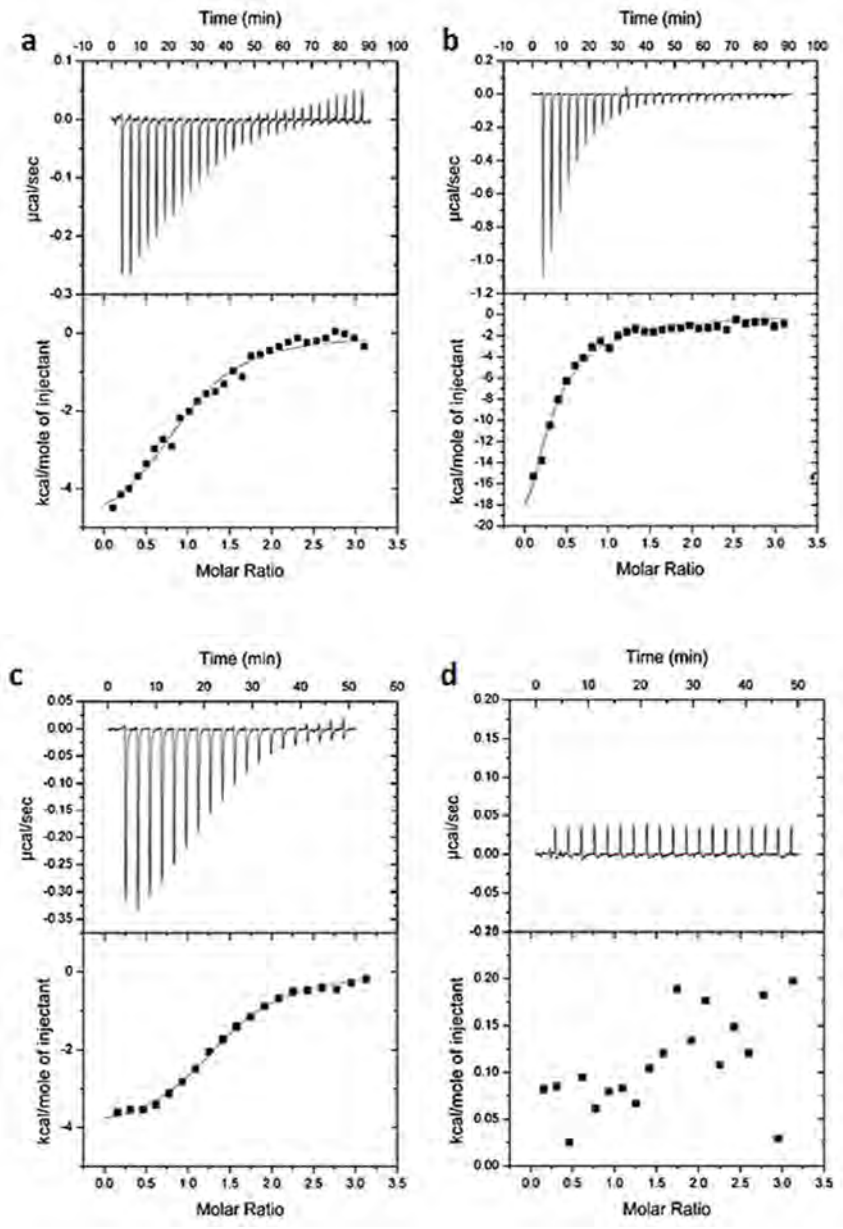

Figure 4.4 Competitive binding of Atg14Ls2 and UVRAG to Beclin2 CC. a&b, The ITC profile of UVRAG titrated to Beclin2 CC (**a**), and the ITC profile of Atg14Ls2 titrated to Beclin2 CC which had already been saturated by UVRAG (**b**); **c&d**, The ITC titration profile of Atg14Ls2 titrated to Beclin2 CC (**c**), and the ITC profile of UVRAG titrated to Beclin2 CC which had already been saturated by Atg14Ls2 (**d**).

4.2.4 The Beclin2-Atg14L interaction is the strongest among Beclin1/2-Atg14L/UVRAG interacting pairs

Given the biophysical differences between Beclin1 and Beclin2, we further ask whether this could result in distinct binding potency of Beclin1 and Beclin2 to Atg14L/UVRAG. *In vitro* competitive experiments to compare the binding affinities of Beclin1 and Beclin2 to Atg14L/UVRAG by ITC were performed. When oversaturated amount of Beclin1 was presented, Beclin2 could outcompete Beclin1 for binding with Atg14L (Figure 4.5 a&b), whereas Beclin1 could not competitively bind with Atg14L in the presence of excessive amount of Beclin2 (Figure 4.5 c&d). Parallel experiments were performed to assess the competitive interaction of Beclin1 and Beclin2 to UVRAG. In the presence of excessive amount of Beclin1, Beclin2 failed to compete with Beclin1 for interacting with UVRAG (Figure 4.6 a&b). Conversely, Beclin1 couldn't outcompete Beclin2 for binding with UVRAG either (Figure 4.6 c&d). These results indicate that Beclin1 and Beclin2 bind to UVRAG with comparable affinity.

In summary, our competition assays have allowed us to rank the interactions in the following order based on their binding affinities: **Beclin2-Atg14L > Beclin2-UVRAG / Beclin1- UVRAG > Beclin1- Atg14L**. The distinct binding affinities suggest that, despite high sequence similarity and the same anti-parallel CC structure, there are significant biophysical and biochemical difference between Beclin1 and Beclin2, particularly involving the binding affinities for Atg14L and UVRAG. The functional

significance of different binding potencies is yet to be investigated.

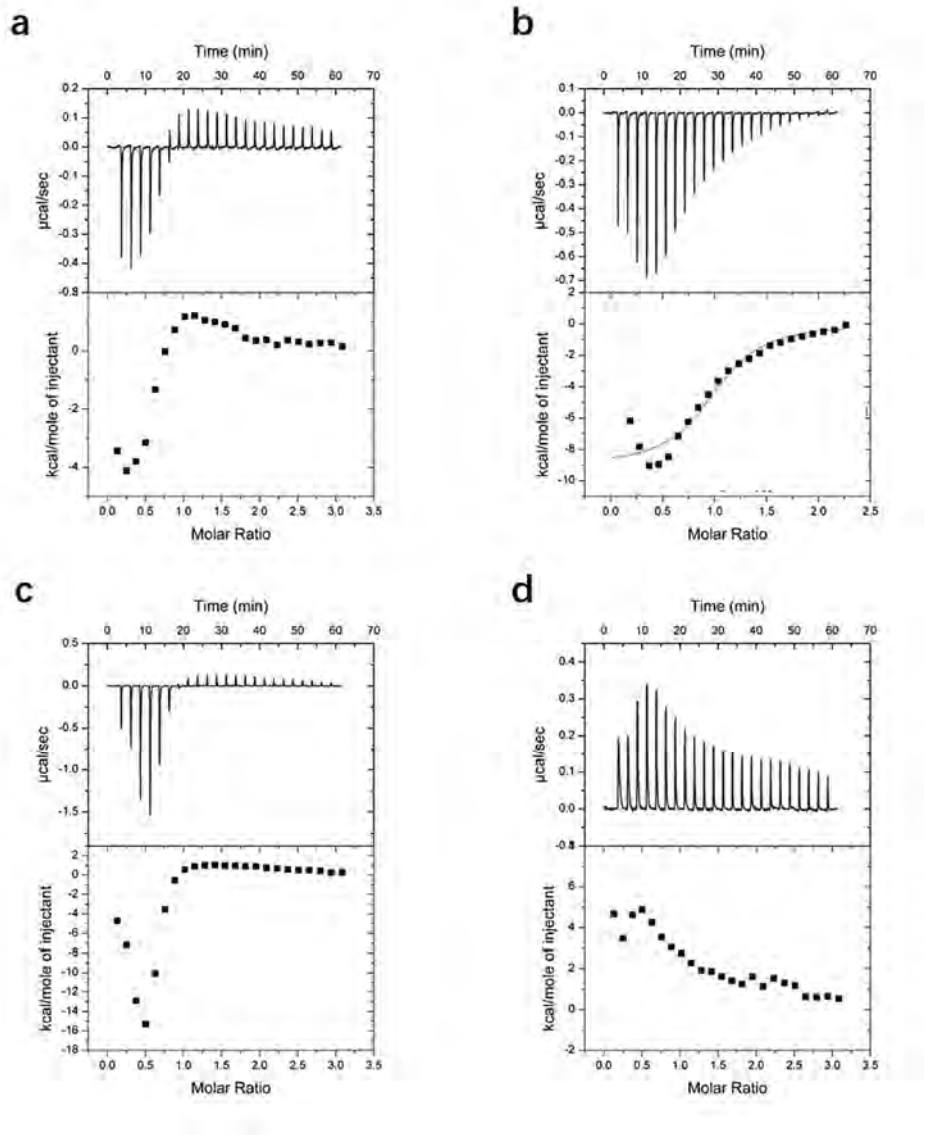

Figure 4.5 Competitive binding of Beclin1 CC and Beclin2 CC to Atg14Ls2. a&b, The ITC profile of Beclin1 CC titrated to Atg14Ls2 (**a**), and the ITC profile of Beclin2 CC titrated to Atg14Ls2 which had already been saturated by Beclin1 CC (**b**); **c&d**, The ITC titration profile of Beclin2 CC titrated to Atg14Ls2 (**c**), and the ITC profile of Beclin1 CC titrated to Atg14Ls2 which had already been saturated by Beclin2 CC (**d**).

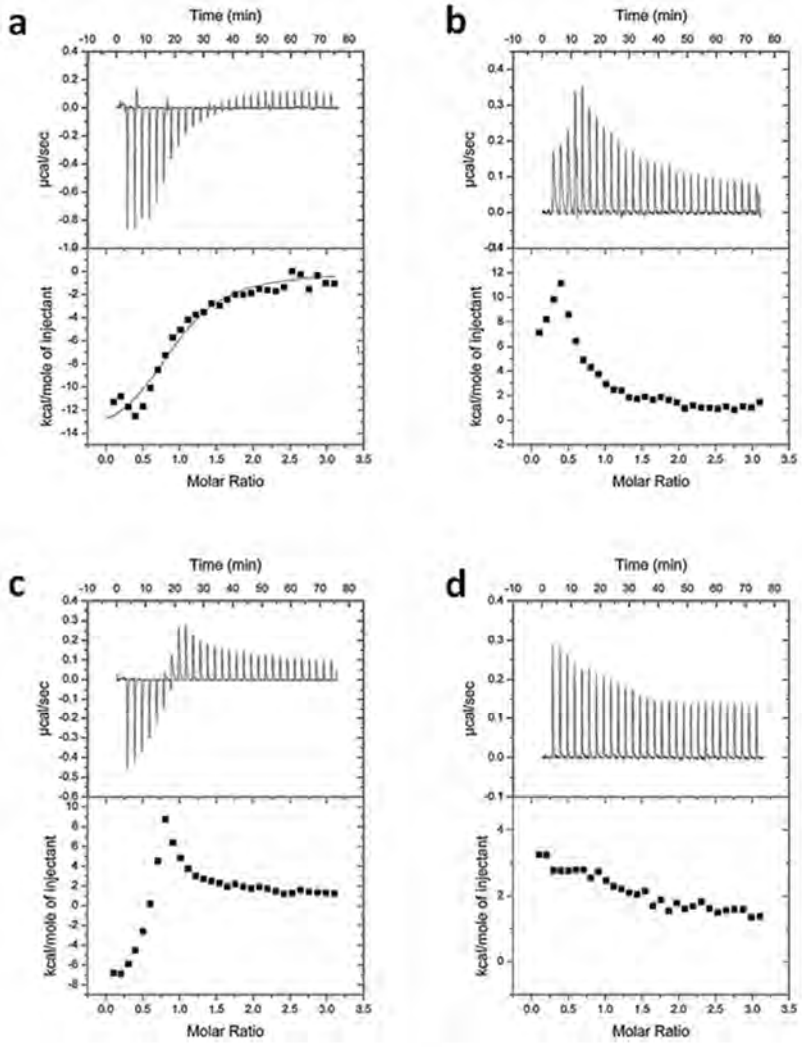

Figure 4.6 Competitive binding of Beclin1 CC and Beclin2 CC to UVRAG. a&b, The ITC profile of Beclin1 CC titrated to UVRAG (**a**), and the ITC profile of Beclin2 CC titrated to UVRAG which had already been saturated by Beclin1 CC (**b**); **c&d**, The ITC titration profile of Beclin2 CC titrated to UVRAG (**c**), and the ITC profile of Beclin1 CC titrated to UVRAG which had already been saturated by Beclin2 CC (**d**).

4.2.5 Structural modeling of Beclin2-UVRAG coiled coil assembly

The structure of Beclin1-UVRAG coiled coil assembly has been recently solved in our lab (manuscript to be submitted). Unlike the anti-parallel homodimeric structure seen for the coiled coil domain of Beclin1 and Beclin2, the Beclin1-UVRAG coiled coil assembly is a parallel heterodimer. Each component contains 7 heptad repeats that packed around each other in the form of a-a' and d-d' pairing pattern (Figure 4.7).

Given the high sequence similarity and structural similarity between Beclin1 CC and Beclin2 CC, a model structure of Beclin2-UVRAG CC assembly can be constructed by superimposing the Beclin2 CC segment (residues 159-206) from its homodimer structure onto that for Beclin1 (residues 175-222) within the Beclin1-UVRAG complex structure. This superposition was done using the secondary-structure matching (SSM) algorithm within the CCP4 suite.

As indicated in Figure 4.8a, the structural model of Beclin2-UVRAG coiled coil complex reveals significant overlapping between Beclin1 and Beclin2. As discussed previously, Beclin2 CC homodimerization results in a non-ideal dimer interface, thus facilitating the transition of Beclin2-UVRAG heterodimer. In our superposition model, more favorable hydrophobic pairings are found at the Beclin2-UVRAG heterodimer interface. Notably, these UVRAG-interacting hydrophobic residues, leucine in

particular, are highly conserved between Beclin1 and Beclin2, suggesting a similar interacting pattern between Beclin1-UVRAG and Beclin2-UVRAG complexes.

Among the thirteen hydrophobic interacting pairs at the dimeric interface, 6 pairs are non-ideal, and 7 pairs are “canonical” pairings. In particular, 5 of 7 “canonical” pairs are leucine zippers (leucine-leucine pairs) that strongly stabilize Beclin2-UVRAG dimer interface via robust Van del Waals interactions (Figure 4.8b). Specifically, the Beclin2-UVRAG structure retains three leucine zippers (L169d-L239d’, L176d-L236d’ and L180a-L250a’) that exist equivalently in Beclin2 homodimer (L169d-L236a’, L176d-L229a’ and L180a-L225d’). Importantly, Beclin2-UVRAG assembly replaces two “imperfect” pairs (L162d-R243a’ and L194a-H211d’) in Beclin2 homodimer into “perfect” leucine zippers, which greatly stabilize the Beclin2-UVRAG heterodimer.

Unlike the Beclin1-UVRAG coiled coil interface that contains a salt bridge interaction for stabilizing the heterodimeric assembly, no such interaction was observed at the Beclin2-UVRAG interface. This reduced involvement of electrostatic interaction is consistent with previous ITC result that Beclin2-UVRAG interaction is more resistant to high salt condition in comparison with Beclin1-UVRAG.

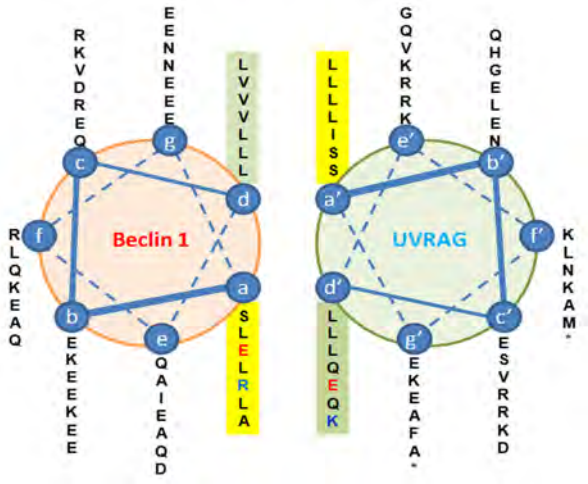

Figure 4.7 Helical wheels presentation of the heptad repeats in Beclin1-UVRAG complex.

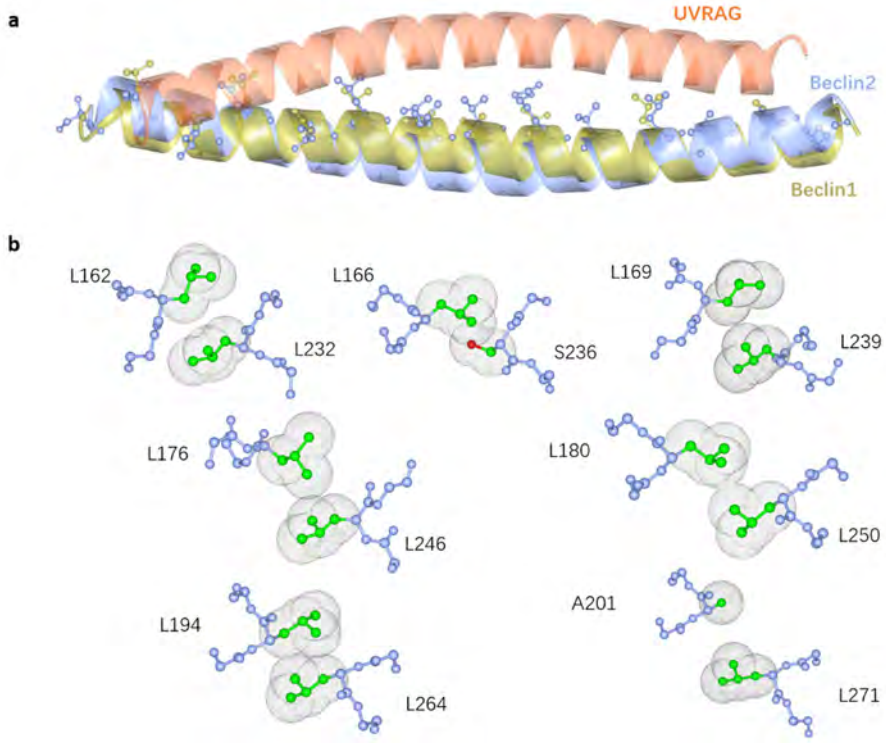

Figure 4.8 The superposition structure model of Beclin2-UVRAG complex and its close-up atomic details. a, the superposition map of Beclin1-UVRAG and Beclin2-UVRAG structures. Peptide chains of UVRAG, Beclin1 and Beclin2 are colored coral, gold and blue, respectively. **b**, atomic details of 7 canonical pairings at the interface of Beclin2-UVRAG heterodimer.

4.2.6 Mapping the coiled coil segments most critical for the Beclin2-Atg14L interaction

The CC region of Atg14L is not highly stable, as degradation was frequently observed in previous experiments. For example, purified Atg14Ls2 protein sample readily degraded at room temperature. As shown in Figure 4.9, a light band slightly lower than the original protein size (around 11KDa) was already presented on the protein sample after purification ("0 hour" sample). With the extension of incubation time, the degradation significantly increased, and the protein band was hardly observed after 24 hours' incubation.

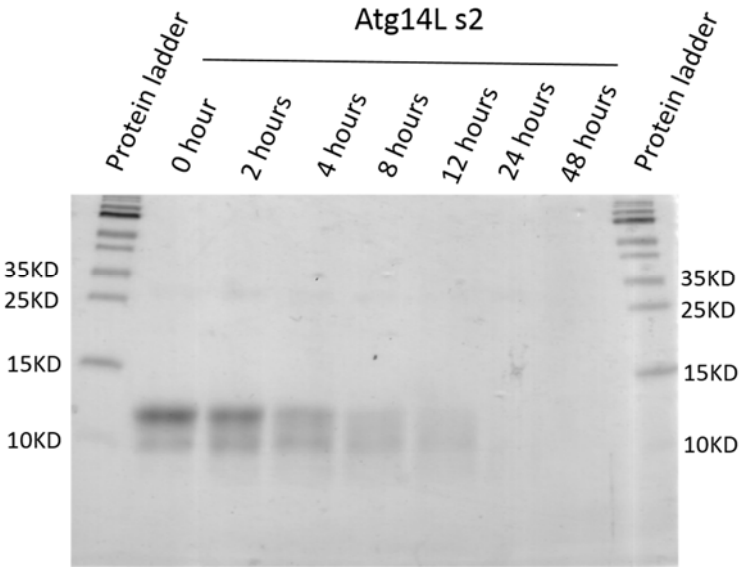

Figure 4.9 SDS-PAGE analysis of Atg14Ls2 protein degradation at different time intervals. The purified Atg14L s2 was placed at room temperature for indicated time lengths, and same amounts of protein were loaded for SDS-PAGE. "0 hour" indicates the purified protein after gel filtration column and concentration using the Amicon centrifugal filter.

In order to identify the Atg14L segments most critical for Beclin2 binding, a series of Atg14L variants were designed to scan through its CC region (as listed in Figure 4.10). All Atg14L variants were cloned into pET49m vector with His_6-GST tag, and expressed in *E. coli.* BL21 strain with reasonable to good yield. The recombinant proteins were purified individually, and then examined by ITC assays to determinate their interactions with Beclin2 CC. Such experiments would also help to identify critical region within Atg14L for Beclin2 binding. Among these variants, the longest construct L2 that covers the entire coiled coil region of Atg14L, together with Atg14Ls2, are unstable.

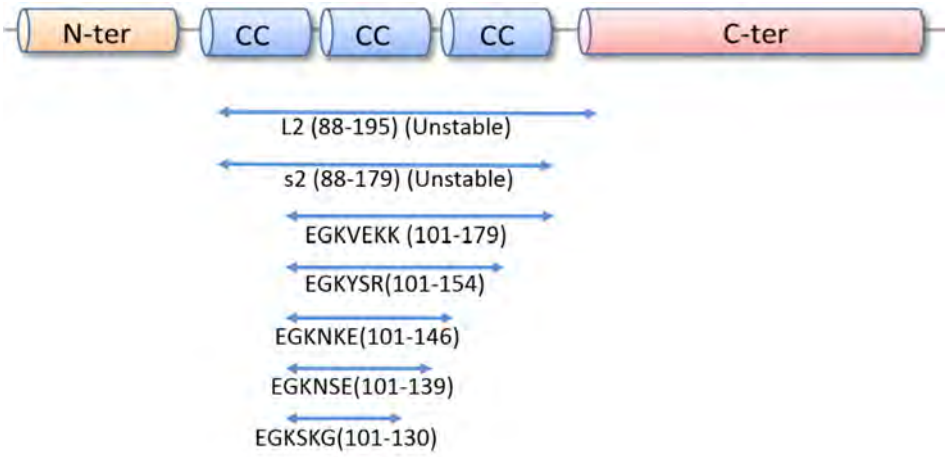

Figure 4.10 Schematic depicting Atg14L variants designed for examination of Beclin2 interaction.

As indicated in Figure 4.11, the ITC results reveal that EGKNKE (101-139) is necessary and sufficient to interact with Beclin2 CC, and Atg14L variants possessing this region can bind to Beclin2 CC in a highly exothermic fashion. However, another

Atg14L variant EGKSKG (101-130) only consists of the core of the second CC region could not bind to Beclin2 CC as estimated from the ITC assay, which only showed the endothermic dilution effect of Beclin2 CC.

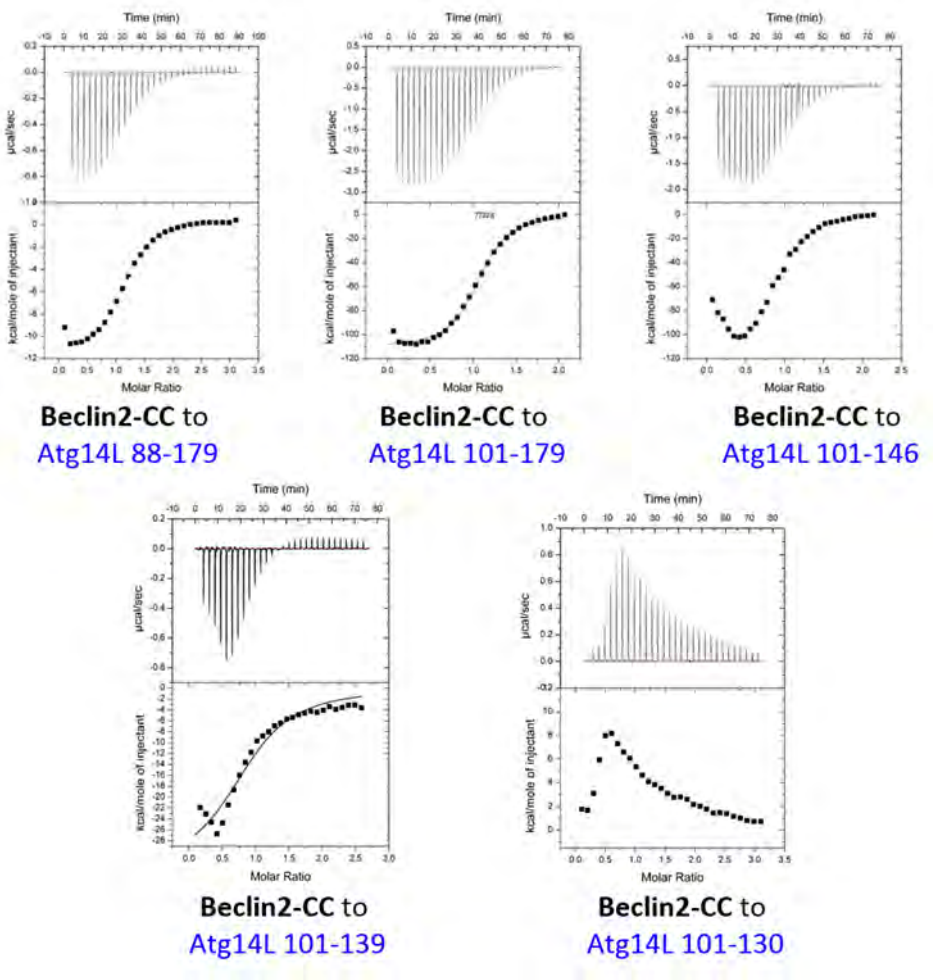

Figure 4.11 The ITC profiles of Beclin2 CC titrated to Atg14L variants.

According to the above ITC measurements, both EGKVEKK (101-179) and EGKNSE (101-139) strongly bind to Beclin2 CC with comparable interacting affinity (K_d 1.2 µM verus 2.5 µM). The longer variant EGKVEKK is selected for further investigation as we believe it would provide us more information about the Beclin2-

Atg14L complex structure.

Subsequently, competitive ITC assays to determine the binding affinity of EGKVEKK to Beclin1-3A mutant and Beclin2 CC were performed. We first confirmed that there is not cross-association between Beclin1-3A and Beclin2-CC (Figure 4.12 a&b). Strikingly, EGKVEKK lost interaction with Beclin1 CC but retain binding with Beclin1-3A mutant (Figure 4.12 c), just like the degraded fragment of Atg14Ls2. Beclin2 could readily outcompete Beclin1-3A for interaction with EGKVEKK in the presence of oversaturated amount of Beclin1-3A (Figure 4.12 c&d), but not the opposite (Figure 4.12 e&f). These results suggest that Beclin2 is superior to Beclin1-3A in terms of interaction with Atg14L (binding affinity: Beclin2-Atg14L > Beclin1-3A-Atg14L). In summary, Beclin2 is a stronger binding partner of Atg14L, even the monomeric form of Beclin1 cannot prevail.

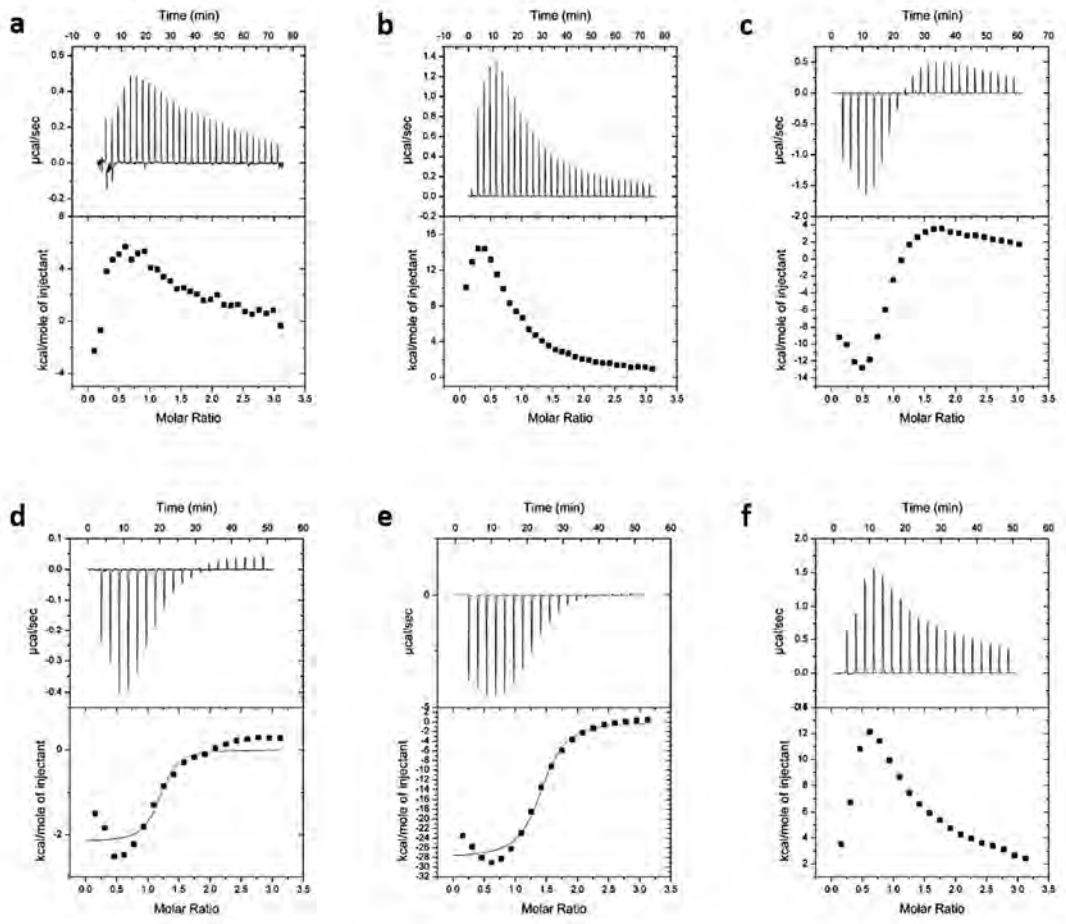

Figure 4.12 Competitive binding of Beclin1-3A and Beclin2 CC to Atg14L EGKVEKK. a, The ITC profile of Beclin1-3A titrated to Beclin2 CC; **b**, The ITC profile of Beclin2 CC titrated to Beclin1-3A. **c&d**, The ITC profile of Beclin1-3A titrated to Atg14L EGKVEKK (**c**), and the ITC profile of Beclin2 CC titrated to Atg14L EGKVEKK which had already been saturated by Beclin1-3A (**d**); **e&f**, The ITC titration profile of Beclin2 CC titrated to Atg14L EGKVEKK (**e**), and the ITC profile of Beclin1-3A titrated to Atg14L EGKVEKK which had already been saturated by Beclin2 CC (**f**);

Chapter Five: Structural Investigation of the Beclin2-Atg14L Complex

5.1 Overview

Various attempts have been made by our lab and other labs to get the Beclin1-Atg14L CC assembly structure via crystallography (Mei et al., 2016). However, those attempts were unsuccessful because of failure in crystallization, probably because the interaction between Beclin1 and Atg14L is relatively weak. In the previous chapter, we demonstrated that Beclin2 exerts stronger binding affinity with Atg14L than that of Beclin1. Such robust interaction between Beclin2 and Atg14L may increase the possibility to crystallize. In addition, given the structural homology between Beclin1 CC and Beclin2 CC, the structure of Beclin2-Atg14L CC assembly, if solved, could further help to reveal that of Beclin1-Atg14L complex.

Empirically, crystals of protein complexes could be yielded from protein mixtures and protein linkers, which crosslinking two proteins or peptides together. Actually, the protein linkers provide a variety of advantages in the manner of generating fusion proteins, for example, increasing expression level, improving stability and solubility, and achieving biological activity (Chen et al., 2013). There are three categories of linkers, namely, rigid linkers, flexible linkers and *in vivo* cleavable linkers. Among these linker, the peptide flexible linkers (usually formed by the

combination of glycine and serine) and protease cleavable linkers are widely applied in crystallography studies, because these linkers provide sufficient flexibility to allow the interaction between the connecting peptides (Chen et al., 2013). In view of that, both flexible linkers and *in vivo* cleavable linkers (cleaved by protease 3C) were applied in this chapter for crystallization trials of the Beclin2-Atg14L complex.

To date, crystallization remains the rate-limiting step in protein crystallography studies, because it is not yet possible to predict the protein behavior in crystallization trials. To improve the likelihood of successful crystallization, “trial and error” strategy is used through extensive screens. In this chapter, a series of crystallization trials were conducted in an attempt to get the Beclin2-Atg14L coiled coil assembly crystal, and various constructs designed for crystallization trials are summarized as follows.

Table 5.1 Trials towards the rational design of Beclin2-Atg14L constructs for crystallization

Beclin2	**Atg14L**	**Rationale**	**Crystal**
CC (157-248)	101-179	N.A.	Precipitate
CC-L225AL229A	101-179	Circumvent the precipitation	No
CC1 (157-207)	101-154	Diminish random coils content	No
CC1 (157-207)	101-154-S116LG130L	Stabilize the complex	Multiple hits

5.2 Experimental Results

5.2.1 Preliminary crystallization trials of Beclin2-Atg14L complex

Crystals of protein complexes are commonly achieved by mixing the complex components together. In this study, the Beclin2 CC and Atg14L EGKVEKK protein was expressed and purified individually, followed by mixing in ratios of 1:2, 1:1, and 2:1 respectively. Surprisingly, the mixture of Beclin2 CC and Atg14L EGKVEKK with ratio of 1:2 or 1:1 precipitated once Atg14L was titrated to the concentrated Beclin2 protein. This could be resulted from the intervention of Atg14L disrupts Beclin2 CC homodimer, exposing hydrophobic residues located on the dimer interface rapidly. This kind of precipitation can be rescued by mixing Atg14L with excess amount of Beclin2, for example, mixing Beclin2 CC and Atg14L EGKVEKK protein with ratio of 2:1. Such mixture was then subjected to crystallization studies using the hanging drop vapor diffusion method as described before.

As observed in Figure 5.1, crystals were grown from two conditions. In condition C1, crystals were grown with some obvious cracks on the surface (Figure 5.1 a), while in condition C2, needle-like crystals appeared (Figure 5.1 b), which are unable to get the x-ray diffraction pattern because of its one-dimensional structure. These crystals were then verified by SDS-PAGE analysis, which suggests these crystals are Beclin2 CC alone rather than Beclin2-Atg14L complex (Figure 5.1 c).

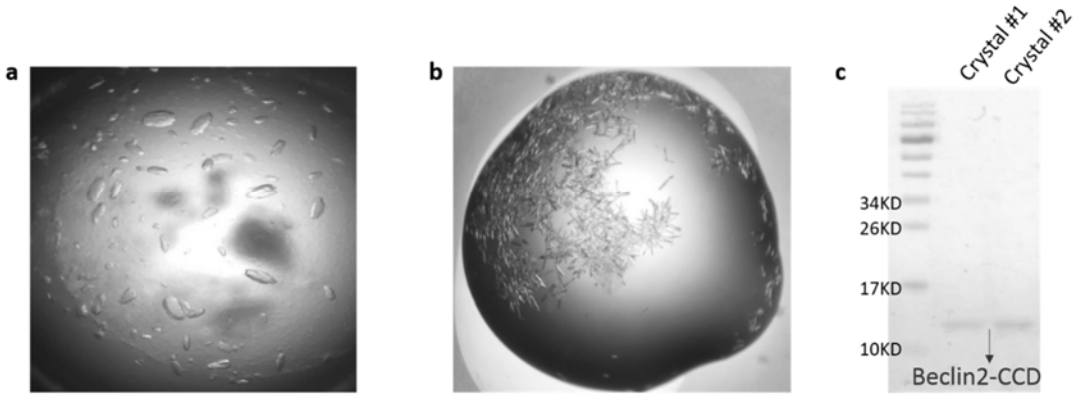

Figure 5.1 Crystals obtained from the optimized crystallization conditions of Beclin2 CC and EGKVEKK mixture. **a**, the crystal grown from modified condition C1 (0.14M Sodium citrate tribasic dehydrate, 0.1M Sodium cacodylate trihydrate pH6.5, 20% v/v 2-Propanol); **b**, the crystal grown from condition C2 (0.2M Sodium citrate tribasic dehydrate, 0.1M Sodium cacodylate trihydrate pH6.5, 30% v/v 2-Methyl-2,4-pentanediol); **c**, crystals were identified by SDS-PAGE. Crystal #1: crystals grown in the reservoir of **a**; Crystal #2: crystals grown in the reservoir of **b**.

Given the easy self-crystallization of Beclin2 CC, the Beclin2 CC and Atg14L EGKVEKK mixture seems less possible to form complex crystals *in vitro*. Then we plan to generate a covalently linked Beclin2 CC-EGKVEKK construct, within which the Beclin2 CC and Atg14L EGKVEKK are tethered together through a flexible peptide chain of 5 x GS. Such cross-link design would not only prevent the spontaneous self-assembly among Beclin2 CC proteins, but also facilitate the immediate interaction of Beclin2 and Atg14L after synthesis in ribosome.

After cloning, the construct Beclin2 CC-$(GS)_5$-EGKVEKK was transform into *E.coli*

strain BL21 for expression. The recombinant protein was loaded into the HisTrap HP column after cell lysis via sonication, and eluted out as instructed by the manufacturer. However, the recombinant protein precipitated immediately after eluting out from the column, and thus not pursued further.

5.2.2 Construction of Beclin2 monomer mutant to circumvent the precipitation problem

To circumvent the precipitation problem caused by the exposure of Beclin2 CC dimer interface, we then decided to incorporate the Beclin2 monomer mutant within the linker construct with Atg14L. This monomer mutant is designed based on the crystal structure of Beclin2 CC, in which two leucine residues L225 and L229 forming leucine zippers that strongly stabilize the Beclin2 homodimer are mutated to alanine. The consequent Beclin2-L225AL229A mutant was expressed and purified as described. The target protein was greater than 95% purity after purification by affinity column in combination with gel filtration column chromatography, as estimated by SDS-PAGE analysis (Figure 5.2a).

Then size exclusion chromatography coupled with static light scattering (SEC-MALS) was applied here to characterize the oligomeric state of Beclin2-L225AL229A. Strikingly, L225AL229A mutant loses its ability to form homodimer, and results in a measured molecular mass of 13.5 KDa (Figure 5.2b), but retains the binding affinity

with Atg14L that is comparable to wild type (Figure 5.2c). Importantly, the failure of Beclin2 self-association solved the precipitation problem when covalently linked with Atg14L via GSx10 linker, by which the length of GS linker was increased to improve its flexibility. Subsequently, crystallization trials of Beclin2-L225AL229A-Atg14L EGKVEKK mixture and Beclin2-L225AL229A-$(GS)_{10}$- Atg14L EGKVEKK were performed. However, these proteins defied crystallization, probably due to the intervening loops within Atg14L and/or the flexible nature of the CC assembly.

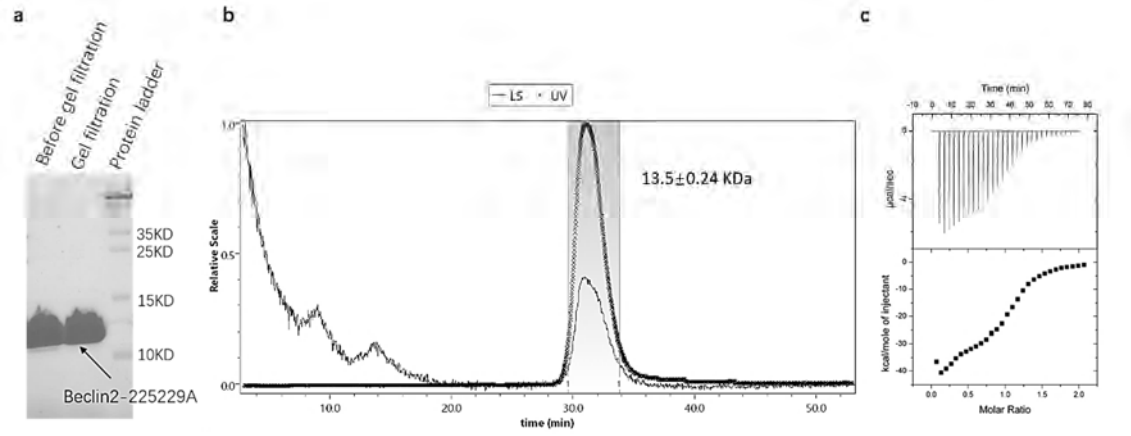

Figure 5.2 Purification, oligomer state, and interaction characterization of Beclin2-L225AL229A mutant. a, SDS-PAGE of Beclin2-L225AL229A; **b**, Molecular weight distributions of Beclin2-L225AL229A as determined in SEC-MALS. LS: light scattering signal; UV: UV signal. **c**, The ITC profile of Beclin2- L225AL229A titrated to Atg14L.

5.2.3 Optimization of Beclin2-CC1 and Atg14L complex for crystallization

It is reported that CC regions of Atg14L are not continuous, but with random coil

fragments between two CC regions (Zhong et al., 2009). We suspect that random coils within the Atg14L construct may impede the crystallization of Beclin2-Atg14L complex. Given that the most critical region within Atg14L for Beclin2 binding already identified in last chapter, likewise, we decided to screen the critical region within Beclin2 CC domain for Atg14L interaction. Four Beclin2 CC sub-constructs (CC1-CC4) were generated, expressed and purified individually. Each sub-construct is 7 heptad repeats in length, with 5 heptad repeats overlapping with the next contiguous sub-construct, scanning through the entire 13 heptad repeats of Beclin2 CC domain (residues 157-248) (Figure 5.3).

Figure 5.3 Constructs designed to map the core region of Beclin2 CC domain responsible for Atg14L/UVRAG interaction. Four constructs CC1-CC4, each consisting of 7 heptad repeats, are engineered to scan through the entire Beclin2 CC. Each heptad repeat is represented by a segment with gradient color from N- to C-terminal.

Then ITC experiments were conducted to investigate the interactions of these Beclin2 sub-constructs with Atg14L. As shown in Figure 5.4, Beclin2-CC1, the N-terminal half of the CC domain, interacts strongly to Atg14L with the binding affinity

comparable to that of the entire Beclin2 CC domain. Whereas constructs CC2 to CC4 show significantly weakened or no interaction with Atg14L. Likewise, Beclin2 CC1 also exhibits the strongest interaction with UVRAG coiled coil domain than other fragments (Figure 5.5). These studies imply that this N-terminal half of Beclin2 CC domain is responsible for the majority of the affinity for Atg14L/UVRAG interaction.

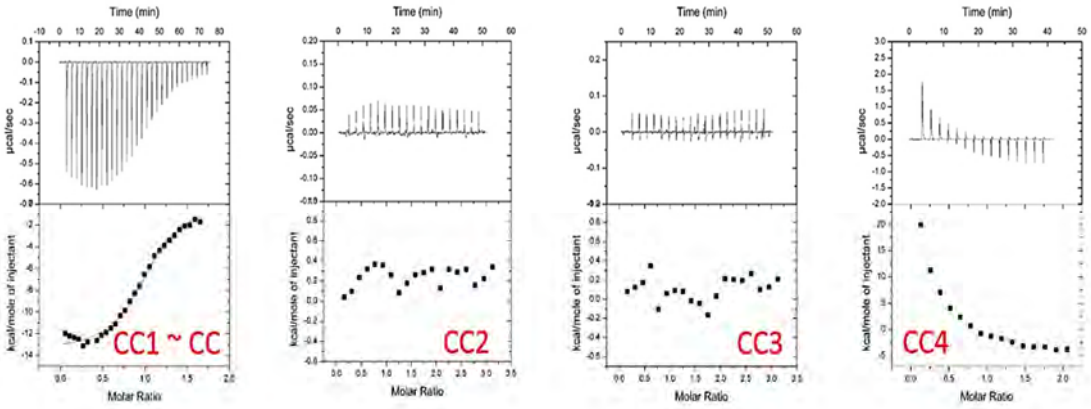

Figure 5.4 ITC profiles for measuring the interactions between Atg14L and Beclin2 CC1-CC4.

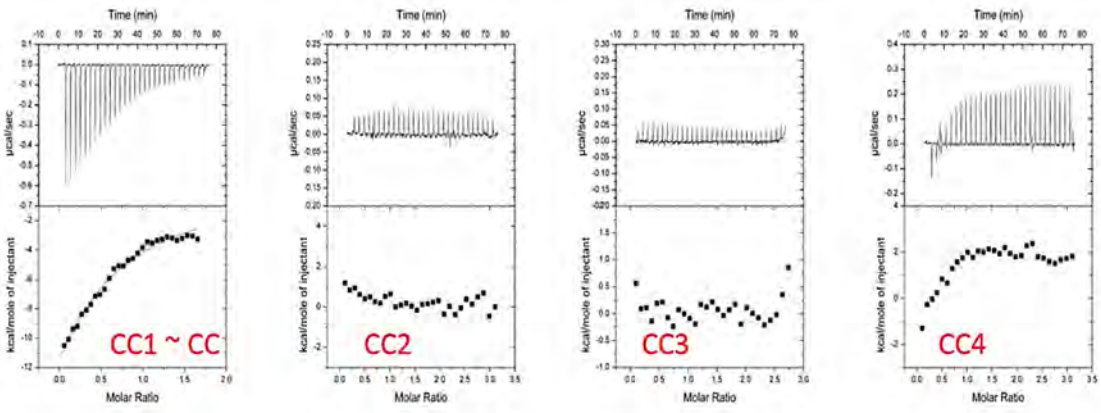

Figure 5.5 ITC profiles for measuring the interactions between UVRAG and Beclin2 CC1-CC4.

To further map the exact binding segment within the CC region of Beclin2, CC1

was divided into three fragments (CC1-A, CC1-B and CC1-C) for Atg14L interaction measurement. Each fragment contains 5 heptad repeats for the sake of maintaining the coiled coil structure. The Atg14L construct EGKNSE with comparable length was applied for ITC examination. As shown in Figure 5.6, only CC1-A (residues 157-193) exhibits binding with Atg14L EGKNSE. However, CC1-B and CC1-C show no detectable interaction with Atg14L.

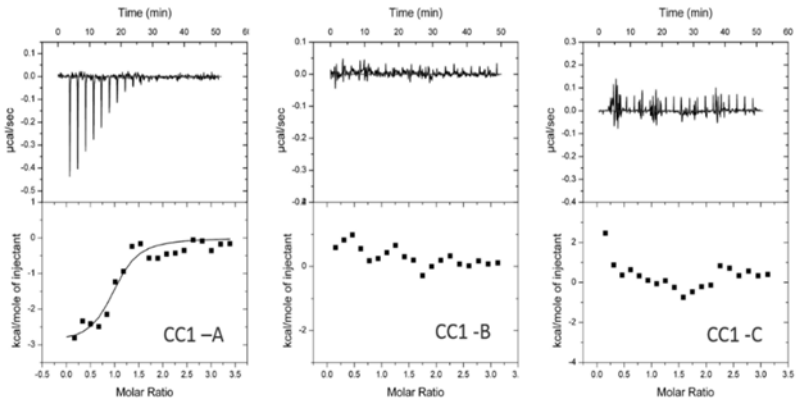

Figure 5.6 ITC profiles for measuring the interactions of Atg14L EGKNSE and three Beclin2 CC1 fragments.

With the most critical region of Beclin2 for Atg14L interaction confirmed, we proceeded to link Beclin2 CC1 with the Atg14L CC segment of comparable length (EGKYSR, residues 101-154) via GS x 10 linker (Figure 5.7 **a**). In this trial, we also design a new construct that covalently links Beclin2 CC1 with Atg14L through the cleavable protease 3C linker (residues LEVLFQGP) (Figure 5.7 **b**). This novel construct allows two peptides to be released independently after protease 3C cleavage,

generating stoichiometrically equal amounts of each subunit for co-incubation. Similarly, Beclin2 CC1-A and Atg14L EGKNSE (residues 101-139) cross-linked constructs were generated (Figure 5.7 **c&d**). These four constructs were further subjected to crystallization trials, whereas no crystal yielded.

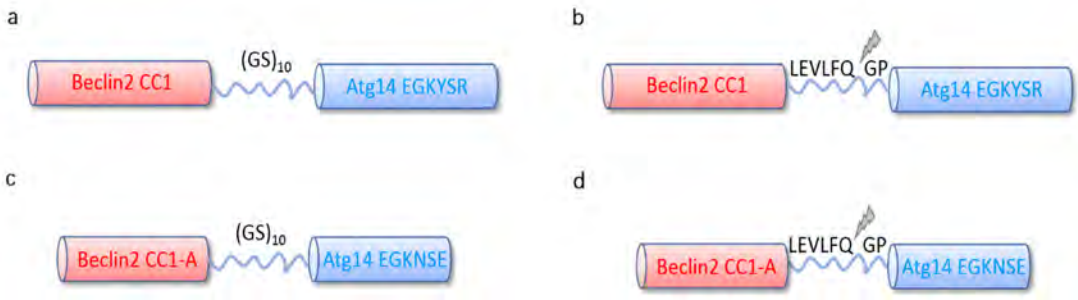

Figure 5.7 Schematic depicting Beclin2 CC1 and Atg14L complex constructs linked via GSx10 linker or cleavable protease 3C linker.

5.2.4 Incorporation of Atg14L mutants to stabilize the Beclin2-Atg14L assembly

Given the flexibility of the Atg14L coiled coil regions, we attempt to incorporate mutations into Atg14L for stability improvement, which might enhance the possibility for crystallization. Based on the characteristic heptad repeats of CC structures, imperfect residues in a or d positions are mutated into leucine with intention to improve stability of the CC interface. In this regard, imperfect residues serine 116, histidine 158, and lysine162 were replaced by leucine respectively, and ITC assays were performed to examine their interactions with Beclin2 thereafter.

As shown in Figure 5.8, the Atg14L S116L mutant enhances the binding with Beclin2 CC with the K_d value around 0.2 μM, stronger in comparison with the wild-type Atg14L. However, H158L and K162L, which positioned away from the critical Beclin2 interacting segment, exhibit similar binding affinity with the wild-type, in consistent with our previous data that Atg14L 101-139 region is essential and sufficient for interacting with Beclin2. In view of that, another imperfect residue glycine 130 within such region was also mutated to leucine, generating S116LG130L mutant in combination of the S116L mutation.

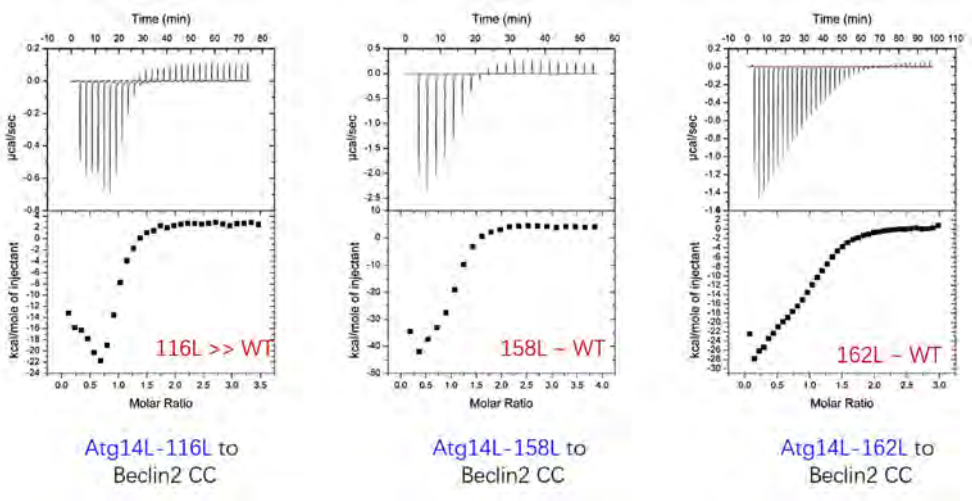

Figure 5.8 ITC profiles for measuring the interactions between Atg14L mutants and Beclin2 CC after imperfect residues at position "a" or "d" are replaced by leucine.

5.2.5 Crystallization of Beclin2-Atg14L complex

Next, the S116LG130L mutation was incorporated into the Beclin2 CC1- Atg14L-EGKYSR cross-link constructs. Two constructs, cross-linking via GSx10 linker and 3C

cleavable linker respectively, were generated as previously described, and subjected to crystallization screening trials after purification. Encouragingly, the Beclin2-CC1-LEVLFQGP-Atg14L-EGKYSR-S116LG130L construct eventually yielded crystals upon a time-consuming process of six month.

To rule out the possibility of degradation during crystallization, the crystal was verified via mass spectrometric analysis. As shown in Figure 5.9, the mass spectrum profile exhibits two components with molecular mass in agreement with the Beclin2-CC1 and Atg14L-EGKYSR-S116LG130L fragments. This data suggests that these two components, generated after the 3C cleavage, remain stable during the process of crystallization.

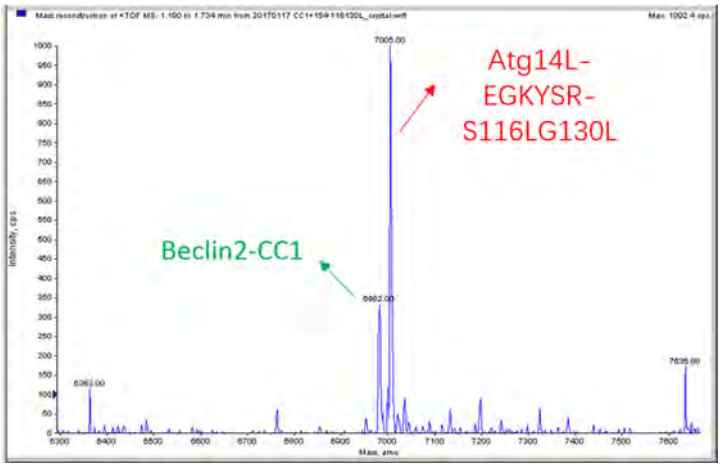

Figure 5.9 Mass spectrometric analysis of the Beclin2-Atg14L crystal sample.

Then the crystal emerged was subjected to x-ray testing, and its diffraction pattern was achieved as showed in Figure 5.10. This crystal is appropriately 200µm in size, and diffracted to ~ 3.4 Å at home x-ray source. Another dataset was collected

at Shanghai synchrotron with resolution to ~ 2.5 Å (Figure 5.11). The space group is $P4_32_12$ with unit cell dimension of (72.50 Å, 72.50 Å, 68.94 Å, 90°, 90°, 90°), and the crystallographic data processing statistics are listed in Table 5.2.

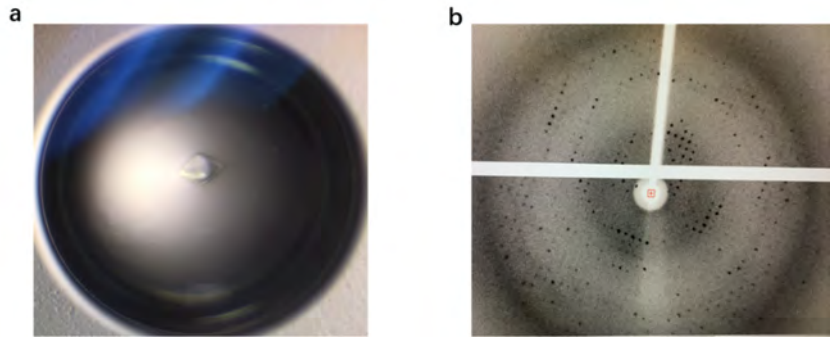

Figure 5.10 Crystal of Beclin2-CC1 and Atg14L-EGKYSR-S116LG130L complex (a) and its x-ray diffraction profile by in-house x-ray machine (b). The crystal was obtained from the solution condition containing 2M Ammonium acetate, 0.1M Sodium citrate tribasic dihydrate pH 5.6, and 30% w/v Polyethylene glycol 4000.

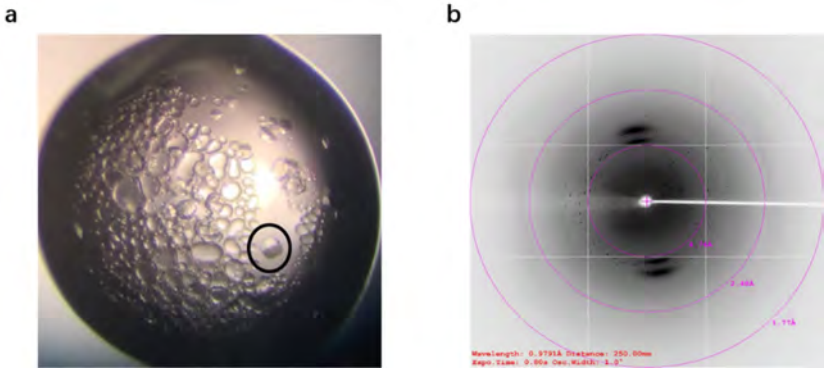

Figure 5.11 Crystal of Beclin2-CC1 and Atg14L-EGKYSR-S116LG130L complex (a) and its x-ray diffraction profile in Shanghai synchrotron (b). The crystal was obtained from the solution condition containing 1.8M Ammonium citrate tribasic pH 7.0.

5.2.6 Beclin2 interacts with Atg14L to form a parallel coiled coil dimer

Given the absence of experimental phasing information, extensive attempts were applied to solve the phase information by molecule replacement, for example, using the partial structure of Beclin2 CC and the structure of Beclin1-UVRAG complex as reference models, or using *ab initio* modeling via MR-Rosetta. However, these attempts of molecular replacement fail to solve the structure, likely because their differences from the target structure prevented phase solving.

In case of no available homolog structural model for molecular replacement, direct *ab initio* phasing is also applicable, however, this algorithm is usually for high-quality data to a resolution of 1.2 Å or better. Recently, a novel program "Arcimbodol lite" was developed to break this resolution limitation, and do *ab initio* phasing using PHASER and SHELXE to locate and extend a large number of small structural fragments like small helix bundles (Rodriguez et al., 2009; Sammito et al., 2013). We then explored this program for structure determination. By inputting the native reflection data only, the program produced an initial poly-alanine structural model. This model was then further built and refined, with a R value of 0.212 (Table 5.2).

Table 5.2 Crystallographic data processing and refinement statistics for Beclin2-Atg14L

Data collection	
Space group	$P4_32_12$
Cell dimensions	
a, b, c (Å)	72.50, 72.50, 68.94
α, β, γ (°)	90, 90, 90
Resolution ^	51.26 – 2.50 (2.64-2.50)
R_{sym} or R_{merge} *	12.5% (34.0%)
I / σI *	14.1 (6.9)
Completeness (%) *	99.8 (100)
Redundancy *	12.2 (12.4)
Refinement	
R_{work} / R_{free}	21.2%/25.3%
No. atoms	
Protein	1093
Ligand/ion	N/A
Water	12
B-factors	
Main chain	61.4
Side chain	72.31
Water	69.37
R.m.s deviations	
Bond length (Å)	0.019
Bond angle (°)	1.82

^ Numbers in parenthesis define the highest resolution shell of data.

* Numbers in parenthesis are the statistics for the highest resolution shell of data.

There are 4 coiled coil chains in a crystal asymmetric unit, where chain A packs against chain D, and B packs against C, forming two almost identical copies of Beclin2-Atg14L heterodimer. However, the C terminal fragments, including residues 188-207 in Beclin2 and residues 137-154 in Atg14L, are likely highly flexible and thus not visible in the electron density map. Interestingly, these invisible flexible fragments are also outside of the mapping critical regions for the Beclin2-Atg14L interaction. Therefore, in line with the previous ITC data, the Beclin2-Atg14L CC assembly is likely not sustained beyond the mapping regions.

The Beclin2-Atg14L complex exhibits a parallel coiled coil assembly as shown in Figure 5.12, where residues at a and d positions of the heptad repeats form hydrophobic pairings by a-a' and d-d' packing. As predicted, the mutation sites (residues 116 and 130) within Atg14L are located on the dimeric interface, which explains the stabilizing effect for the sake of crystallization. It is unlikely that these two mutations would cause artificial complex structure, because the structure successfully matched up 4 pairs of leucine-leucine/isoleucine pairings. These two residues were then replaced by serine and glycine respectively to probe the native interacting state of Beclin2-Atg14L complex. Whereas glycine is a known helix breaker, and along with this line, the Beclin2-Atg14L complex generates 7 pairs of a-a' or d-d' pairings, and 5 of them are canonical hydrophobic pairings (Figure 5.13).

Analysis of this heterodimeric interface reveals the molecular determinants that

enable the stable interaction of Beclin2 and Atg14L (Figure 5.13 and 5.14). Specifically, canonical hydrophobic pairings in Beclin2 homodimer (L166-A239, L169-L236, L1760-L229, L180-L225) are largely maintained in the Beclin2-Atg14L heterodimer (L166-I113, L169-S116, L1760-L123, L180-I127). In addition, one imperfect pairing (L162-R243) in Beclin2 is altered as perfect leucine zipper (L162-L109) in the complex. Besides, residue E173 in Beclin2 forms energetically favorable electrostatic interaction with residue R119 in Atg14L, exerting a positive effect in stabilizing the heterodimeric interface in comparison with the destabilizing effect in Beclin2 homodimer. There are two additional pairs of interhelical electrostatic interactions at the dimeric interface, which formed by residues E165-K117, and E172-K124. Taken together, Beclin2-Atg14L is notably more stable than the Beclin2 homodimer by retaining perfect hydrophobic pairings and gaining additional stabilizing interactions.

As shown in Figure 5.14, comparison analysis of the dimeric interfaces reveals that Atg14L and UVRAG compete for multiple interacting sites within Beclin2 (L162, L166, L169, L176 and L180) for hydrophobic pairing formation. Such competition likely explains the mutually exclusive manner of Atg14L and UVRAG when binding with Beclin2. Furthermore, by forming additional electrostatically complementary pairing (E173-R119), the Beclin2-Atg14L complex achieves higher binding affinity in comparison with Beclin2-UVRAG complex.

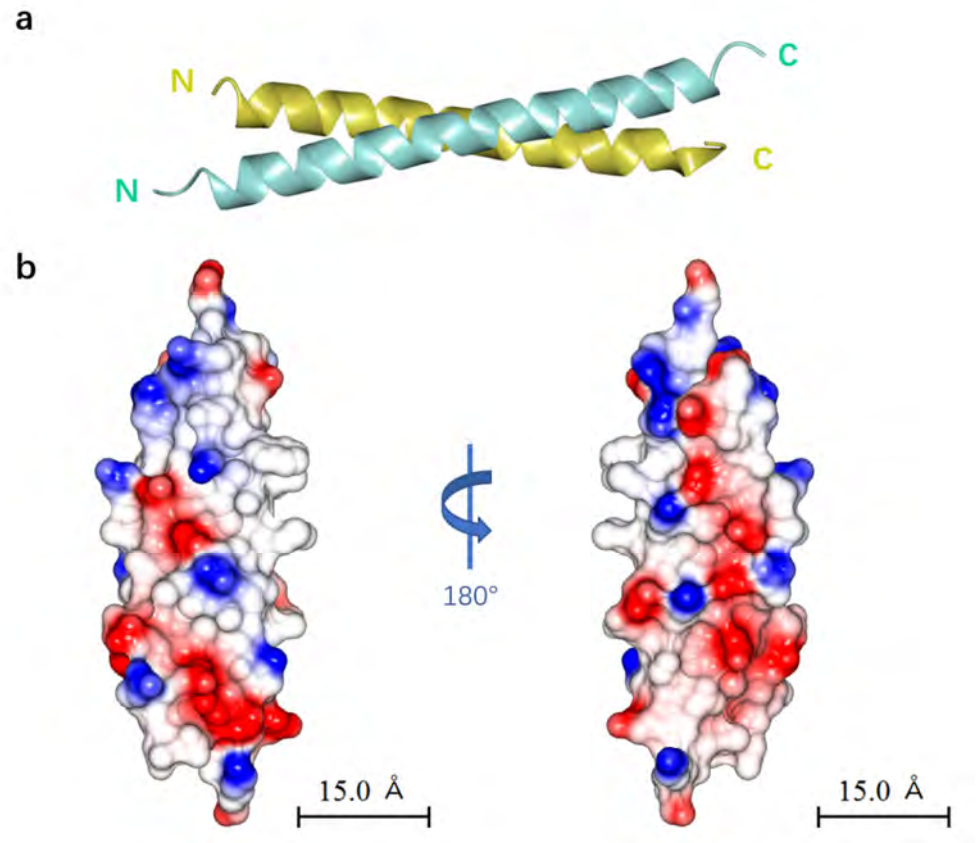

Figure 5.12 The crystal structure of Beclin2-Atg14L coiled coil assembly. a, the parallel heterodimer structure of Beclin2-Atg14L complex represented by ribbons. Beclin2 is colored in gold, and Atg14L in sea green. **b,** the distribution of electrostatic charges on the complex surface.

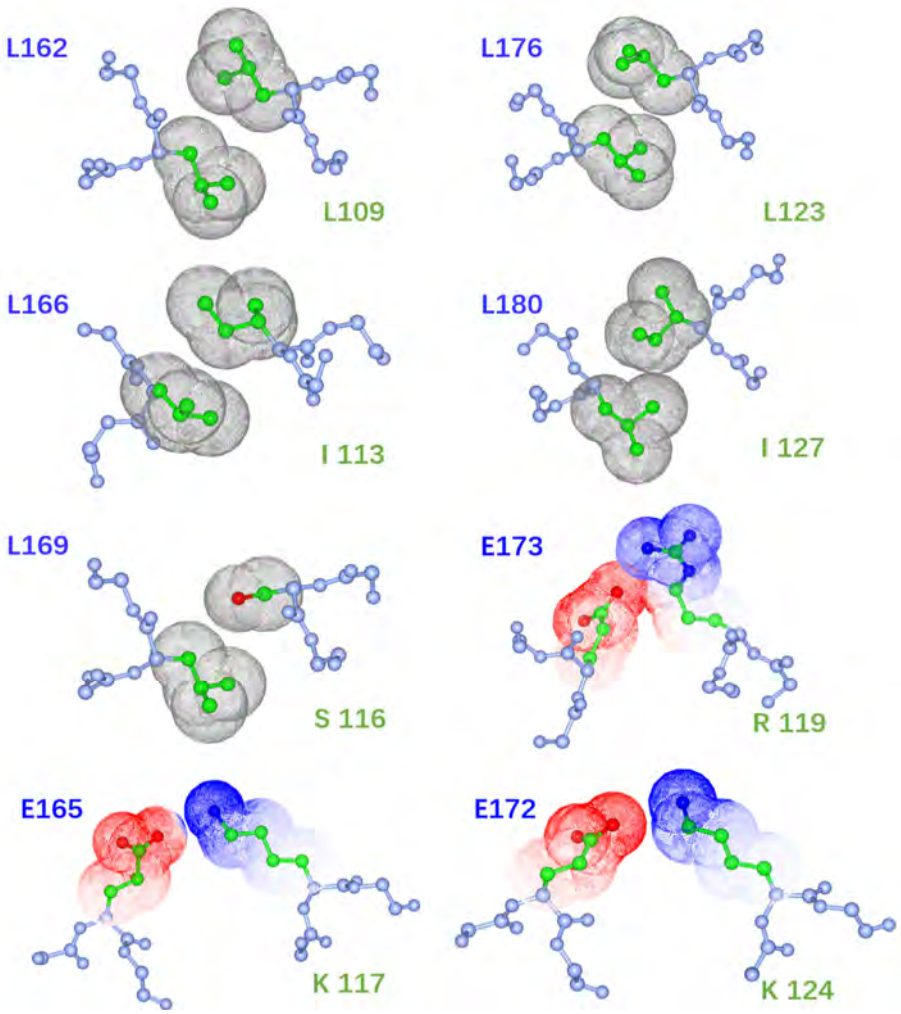

Figure 5.13 Close-up view of the hydrophobic and electrostatic pairings of Beclin2-Atg14L complex structure. Residues in Beclin2 are labelled in blue, and residues in Atg14L in green. The interacting pairings are illustrated by Van der Waals spheres depicting the side-chain atoms.

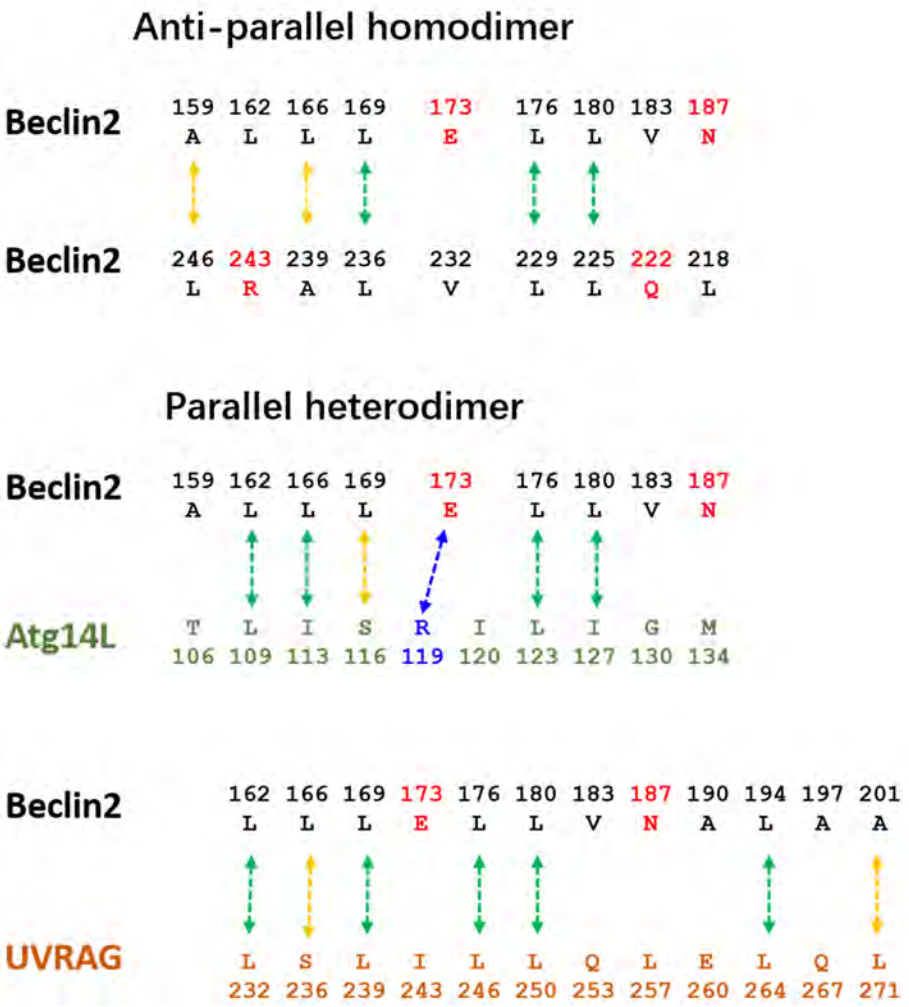

Figure 5.14 Comparison analysis of the dimeric interfaces of Beclin2 homodimer with the Beclin2-Atg14L and Beclin2-UVRAG heterodimers. Residues colored in red indicate the charged or polar residues within Beclin2 that may destabilize its coiled coil interface. Arrows represent the energetically favorable pairings at the interface. Orange arrows mark the canonical hydrophobic pairings, green arrows mark the leucine-leucine or leucine-isoleucine pairs that strongly stabilize the interface, and the blue arrow indicates the electrostatic interacting pairing.

5.2.7 Structure-based mutations to delineate the molecular determinants that drive the formation of a Beclin2-Atg14L complex

Based on the structural information of Beclin2-Atg14L CC assembly, experiments were set out to test whether mutational perturbation in Beclin2 or Atg14L would weaken this interaction. To examine the role of hydrophobic pairings in Beclin2-Atg14L association, leucine pairs L166L169 and L176L180 were mutated to glutamic acids. As a control, leucine 194 and alanine 20, which position away from the binding region, were also mutated (Figure 5.15). Similarly, isoleucine 113 and 127 of Atg14L were also mutated to glutamic acid respectively to perturb the hydrophobic interface.

Then ITC assays were performed to examine their effects on Beclin2-Atg14L interaction. As shown in Figure 5.16, Beclin2 CC mutants L166EL169E and L176EL180E abolished the interaction between Beclin2 and Atg14L, while mutations outside the binding region (L194EA201E) retains the binding affinity comparable to that of wild-type, suggesting that leucine 166, 169, 176 and 180 are critical for maintaining Beclin2-Atg14L interaction. Likely, for Atg14L mutants, single mutation of Ile to Glu abolishes the interaction between Beclin2 and Atg14L (Figure 5.17). Such mutational perturbation is in line with our structural model that hydrophobic pairings contribute largely to stabilize the Beclin2-Atg14L CC assembly.

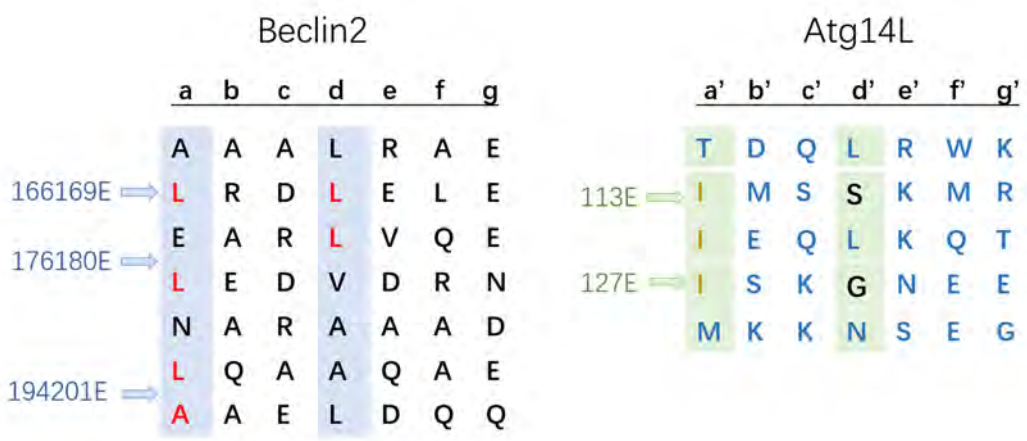

Figure 5.15 Schematic illustrating the mutation design within Beclin2 or Atg14L sequence. The heptad repeats of coiled coil are represented by "abcdefg", among which "a" and "d" are typically hydrophobic amino acids, while "e" and "g" are normally charged amino acids, and other positions could be any kind of amino acid.

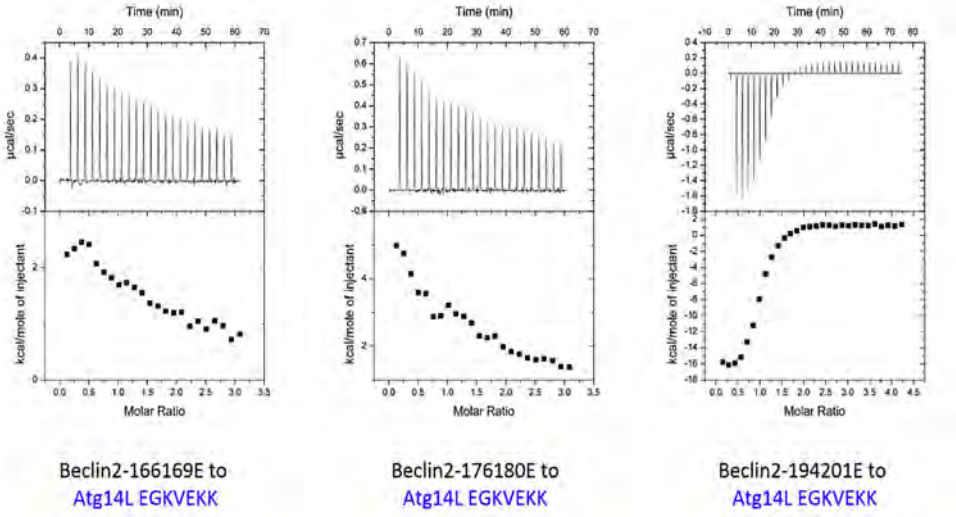

Figure 5.16 ITC profiles for measuring the interactions between Beclin2 CC mutants and Atg14L. Leucine residues within Beclin2 critical for forming the hydrophobic CC interface were replaced by glutamic acids.

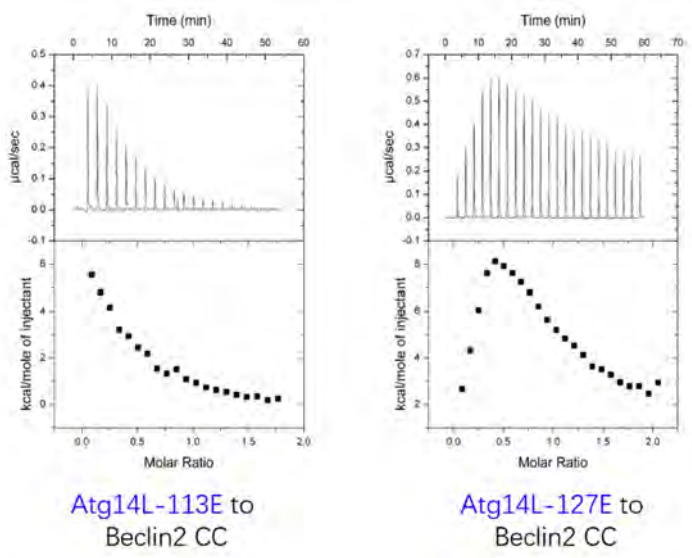

Figure 5.17 ITC profiles for measuring the interactions between Atg14L mutants and Beclin2 CC. Isoleucine residues within Atg14L critical for forming the hydrophobic CC interface were replaced by glutamic acids.

Subsequently, *in vivo* co-IP experiments were applied to further investigate the potency of these variants on Beclin2-Atg14L interaction. First, myc-tagged Beclin2 mutants and flag-tagged Atg14L wild type were co-transfected into Hela cells, followed by assessment of their interaction by co-IP. Experimental results reveal that double Leu-to-Glu mutations of Beclin2, which is sufficient to abolish the Beclin2-Atg14L CC assembly *in vitro*, could not impair the full length Becin2-Atg14L interaction *in vivo* (Figure 5.18).

Similarly, flag-tagged Atg14L mutants and myc-tagged Beclin2 wild type were co-transfected into Hela cells, and then their interactions were assessed by co-IP assays. Our data shows that, in contrast to the significant blocking or enhancing effect

in vitro, single mutations of Atg14L (113E, 127E and 116L) pull down similar amount of Beclin2 as wild type (Figure 5.19 a), suggesting that although these residues are critical for Beclin2-Atg14L interaction, they are not sufficient to completely abolish the association *in vivo*. This may be due to the involvement of other regions and/or other co-factors such as Vps34 to facilitate Beclin2-Atg14L association. However, double mutations of Atg14L (S116LG130L) could positively regulate Beclin2-Atg14L interaction in comparison with wild type Atg14L (Figure 5.19 a&b), likely because two additional perfect hydrophobic pairings are formed at the CC interface.

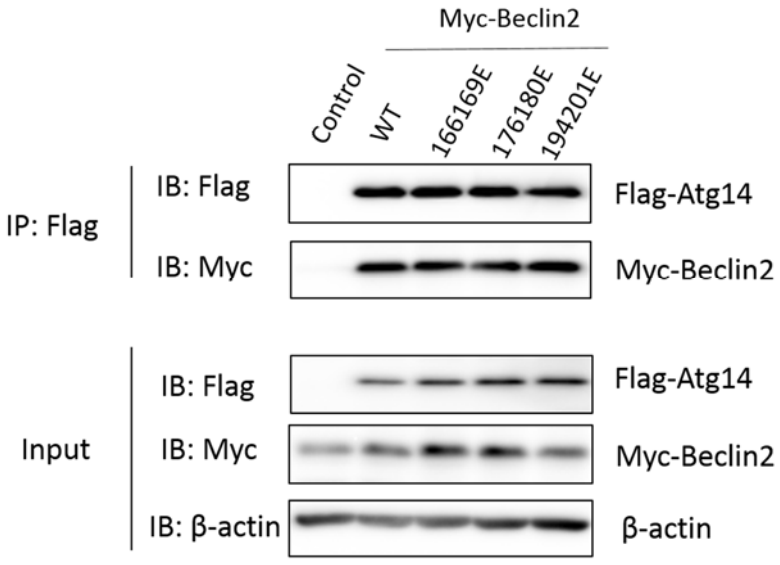

Figure 5.18 Co-IP and immunoblot analysis to characterize the association between Beclin2 mutants and Atg14L in Hela cells. Flag-tagged Atg14L was probed using anti-flag agarose beads for IP, and the cell lysate (input) and immunoprecipitated (IP) were analyzed by immunoblotting (IB) with antibodies as indicated.

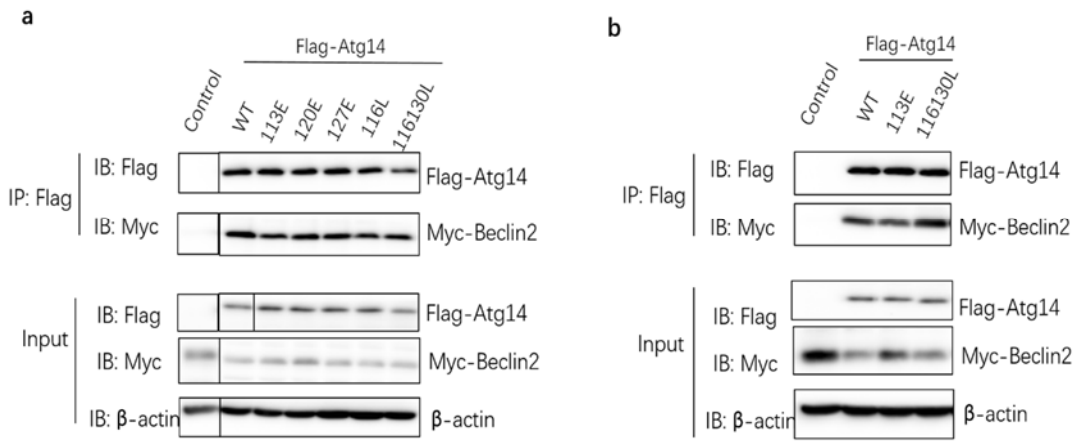

Figure 5.19 Co-IP and immunoblot analysis to characterize the association between Atg14L mutants and Beclin2 in Hela cells. Flag-tagged Atg14L was probed using anti-flag agarose beads for IP, and the cell lysate (input) and immunoprecipitated (IP) were analyzed by immunoblotting (IB) with antibodies as indicated.

Chapter Six: Biochemical and Functional Studies of Beclin2 in GPCR Signaling

6.1 Overview

G protein-coupled receptors (GPCRs) are a large family of transmembrane receptors that trigger intracellular response to extracellular stimuli through G-protein signaling pathways. A variety of GPCRs are expressed on the surface of mammalian cell membrane to sense distinct stimulus, and therefore, controlling a vast array of physiological processes. Given its broad significance in normal physiology, GPCRs are common therapeutic targets in the pharmaceutical industry.

Following agonist stimulation, activated GPCRs become internalized into endosomes and sorted into two separate paths: either released back to the plasma membrane for reactivation, or trafficked to lysosomes for degradation. The lysosomal degradation of GPCRs normally relies on the ubiquitin-dependent ESCRT machinery or ubiquitination-independent GASP1 pathway. For the latter, only a subset of GPCRs are regulated, including D2 dopamine receptors (D2R), δ-opioid receptor (DOR), type 1 cannabinoid receptor (CB1R), and G protein-coupled receptor 55 (GPR55).

It is reported that GASP1 is one of the Beclin2 binding partners, and their interaction is critical to its function in GPCR signaling regulation (He et al., 2013). The

interaction between Beclin2 and GASP1 was identified by the yeast two-hybrid screening, and it was further proved that the N-terminal fragment of Beclin2 (Beclin2-NTF) and GASP1 C-terminus are responsible for this interaction using co-immunoprecipitation (He et al., 2013). However, the specific binding sites of both proteins that contribute to their interaction need to be further clarified. In this chapter, the interaction between Beclin2 NTF and GASP1 C-terminal armadillo Repeat domain was investigated, and the potential of Beclin2 in regulating GPCR signaling was examined.

6.2 Experimental Results

6.2.1 Expression and purification of GASP1 C-terminus

It is reported that the GASP1 C-terminal tail is responsible for the interaction with Beclin2 N-terminus (He et al., 2013). Therefore, the C-terminus of GASP1 (residues 1000-1395) was cloned into a modified pETsumo vector, which contains a hexa-histidine (His_6) tag, a sumo tag, and the human rhinovirus 3C protease cleavage site. The recombinant protein was expressed and purified following the same protocol described previously. However, after affinity column and gel filtration column chromatography, the target protein could not separate from the fusion protein and other impurities (Figure 6.1), implying the existence of self-aggregate and/or folding problems in the recombinant protein.

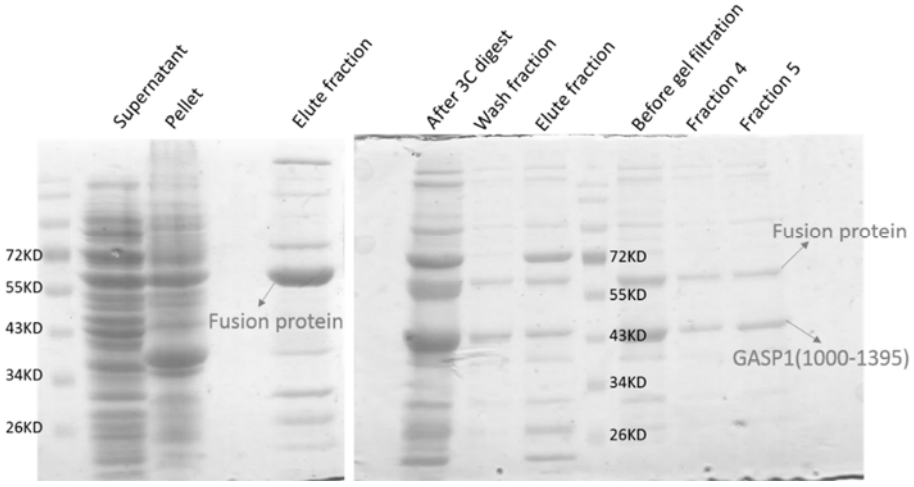

Figure 6.1 SDS-PAGE analysis of the GASP1 (1000-1395) expression and purification.

To examine the possible protein aggregates, GASP1(1000-1395) protein sample

was analyzed under either non-reducing or reducing conditions via light scattering. As indicated in Figure 6.2, GASP1 (1000-1395) exists as high molecular mass aggregates in buffer 50mM Tris, 450mM NaCl, pH 8.0, while this aggregation could be prevented by adding 5mM DTT, the reducing reagent to avoid disulfide bridge formation between cysteines. GASP1 (1000-1395) exhibits a measured molecular mass of 47 KDa, in good agreement with its theoretical value 45 KDa, suggesting it converts to monomeric state in the presence of DTT. This phenomenon probably caused by the cysteine-rich region in the N-terminal of GASP1 (1000-1395), which can be easily oxidized to form covalent disulfide bonds between thiol groups of cysteines. The intermolecular disulfide bonds resulted in the failure of separating GASP1 (1000-1395) from the fusion protein during purification.

6.2.2 Optimization of GASP1 C-terminal construct

According to the result of Jpred (Drozdetskiy et al., 2015), a consensus secondary structure prediction server, the cysteine-rich region of GASP1 (1000-1395), about 150 amino acids in length, is almost unstructured. The remaining portion of the protein (1148-1395) is predominantly helical, which consists of six armadillo repeats (AR). Therefore, we generated a novel construct (1148-1395) that contains these six armadillo repeats, but excludes the unstructured but cysteine-rich region. In addition, inspired by the result of structure homology modelling using SWISS-MODEL Workspace (Bordoli et al., 2009), a hydrophobic residue phenylalanine 1170

was mutated to lysine with intention to improve the solubility. This new construct incorporated with the F1170K mutation is termed as GASP1-F1170K.

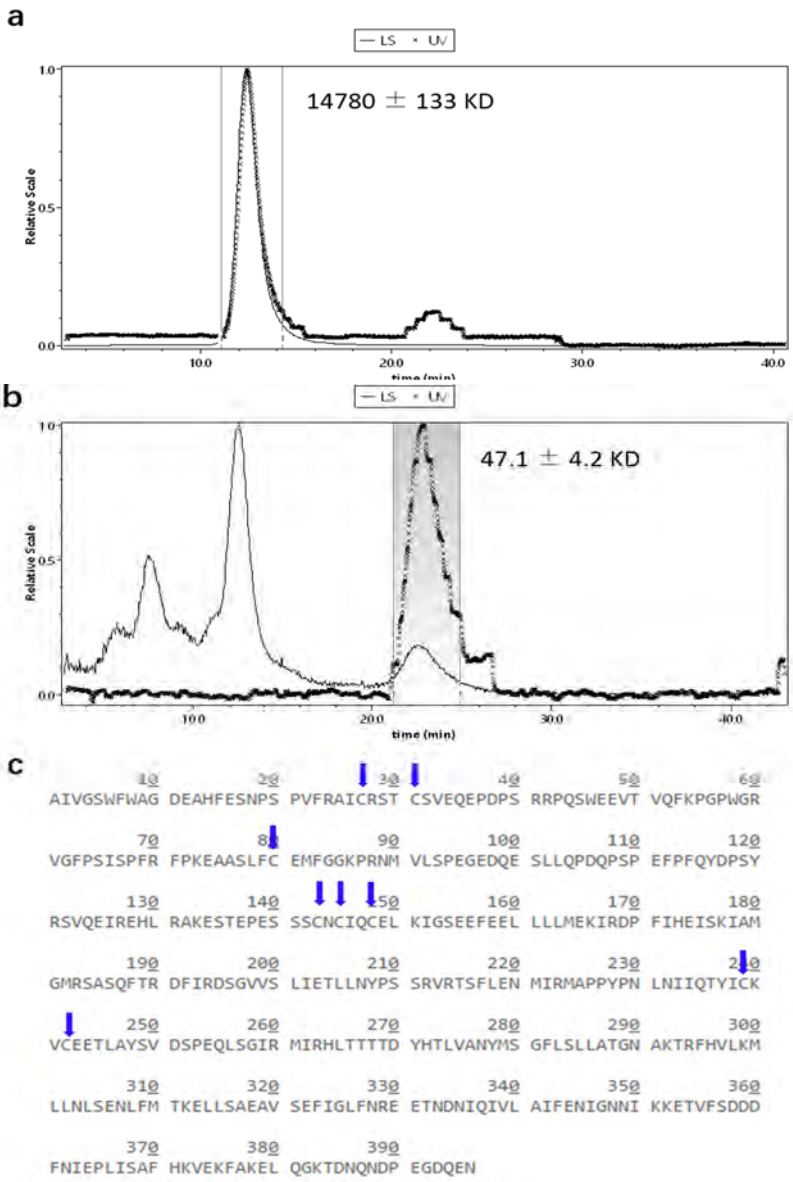

Figure 6.2 Protein aggregate analysis of GASP1 (1000-1395) by SEC-MALS. a, GASP1 (1000-1395) aggregated in buffer 50mM Tris, 450mM NaCl, pH 8.0; **b**, GASP1 (1000-1395) present as a monomer in buffer 50mM Tris, 450mM NaCl, 5mM DTT, pH 8.0. LS: light scattering signal; UV: UV signal. **c**, protein sequence of GASP1 (1000-1395). The arrows indicate cysteine residues.

The gene construction, expression and purification of GASP1-F1170K were conducted, and pure protein was obtained without any noticeable impurity band on the SDS-PAGE gel (Figure 6.3a). Then GASP1-F1170K was subjected to the SEC-MALS analysis for oligomeric state determination. The result shows an estimated molecular mass that is close to it theoretical value (31.9 KD versus 28.6KD), suggesting that GASP1-F1170K is prevailingly presented as monomer without aggregation problems (Figure 6.3b).

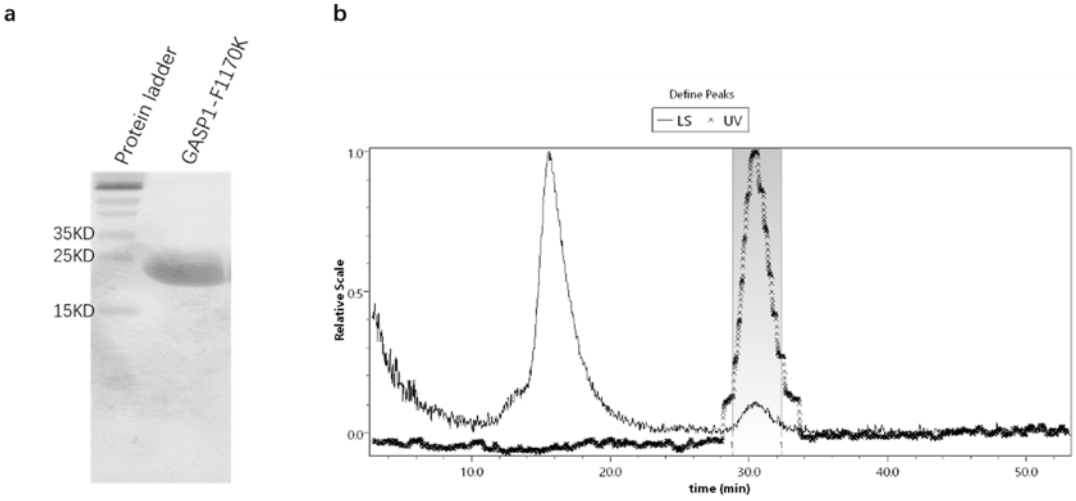

Figure 6.3 Characterization of GASP1-F1170K by SDS-PAGE and SEC-MALS analysis. a, SDS-PAGE analysis of GASP1-F1170K after purification; **b,** Molecular weight distributions of GASP1-F1170K as determined in SEC-MALS. LS: light scattering signal; UV: UV signal.

6.2.3 Characterization of Beclin2-GASP1 interaction

With pure Beclin2 NTF (residues 12-90) and GASP1-F1170K obtained, their

interaction was then investigated via a series of experiments. First, ITC assays were conducted, whereas the result denied the direct interaction between these two proteins (Figure 6.4).

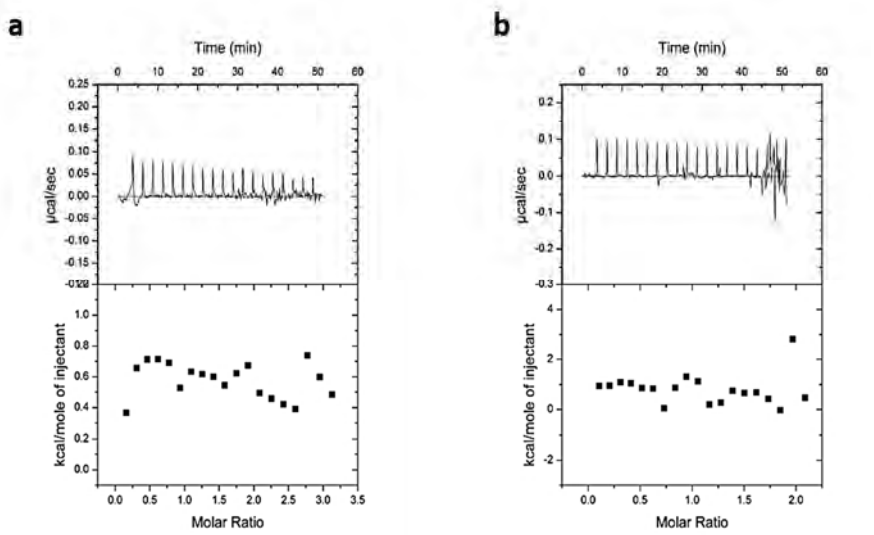

Figure 6.4 Determination of the interaction between Beclin2 NTF and GASP1-F1170K. a, ITC profile of GASP1-F1170K titrated to Beclin2 NTF; **b**, ITC profile of Beclin2 NTF titrated to GASP1-F1170K.

Since ITC assay might not sensitive enough to detect interactions of low binding affinities, to rule out the possibility of false negative, we next performed pull-down assay to further examine this interaction. Specifically, the purified His-sumo tagged GASP1 was bound to the nickel agarose resin, followed by the adding of Beclin2 NTF protein. After co-incubating for a few hours, the unbound protein was washed away. Then the binding partner, if any, would be eluted out with the His-sumo tagged GASP1, and analyzed by SDS-PAGE. In a parallel experiment, His-sumo tag was

applied as the control. As indicated in Figure 6.5, for the control sample, Beclin2 NTF protein was presented only in the washed fraction, and His-sumo tag was in the eluted fraction. For the His-sumo tagged GASP1 sample, however, Beclin2 NTF protein presented in both washed and eluted fractions, even though excess amount of GASP1 was loaded. This data may imply that the Beclin2-GASP1 interaction is quite weak and dynamic.

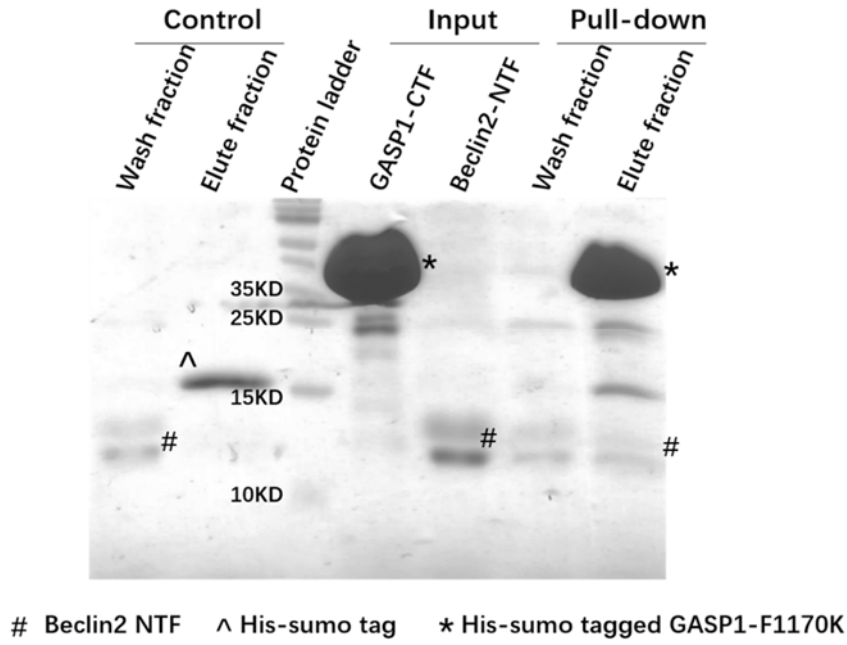

Figure 6.5 SDS-PAGE analysis of samples from pull-down assay.

To further illuminate the potential Beclin2-GASP1 interaction, a peptide array chip was designed and applied to probe residues within Beclin2 NTF which are responsible for GASP1 binding. This experiment is designed based on the reported data that Beclin2 N-terminus is natural unstructured, and that armadillo repeats

domain is known as a peptide-binding scaffold (Parmeggiani et al., 2008). The entire Beclin2 N-terminus (residues 1-105) is divided into 31 peptides, each with 15 amino acids long, and with 12 residues overlapping with the next contiguous peptide. A cellulose membrane attached with these peptides was co-incubated with purified His-sumo tagged GASP1-F1170K, and then incubated with anti-His antibody, followed by detection via immunoblotting. However, this peptide array chip screening throughout the Beclin2 N-terminus did not identify any peptide fragment that positively interacts with GASP1 (Figure 6.6).

Figure 6.6 Immunoblotting analysis of Beclin2 peptide array chip. The position of 31 membrane-anchored peptides is indicated.

6.2.4 Mass spectrometry-based interactome analysis of Beclin2 N-terminus

Thus far, there is still insufficient evidence to support the direct interaction between Beclin2 N terminus and GASP1 C terminal armadillo repeats domain. This

raises the possibility that the binding of Beclin2 and GASP1 maybe too weak and dynamic to be detected in above assays that require interactions with high off-rates. Given the reported positive result using co-IP (He et al., 2013), another possibility is that other co-factors may be involved to stabilize the formation of this complex, which are lacked in the above *in vitro* assays. To investigate the existence of these potential co-factors, mass spectrometry driven proteomics analysis, as described in methodology, was performed to identify putative proteins that might affect the formation of Beclin2-GASP1 complex. Such experiment, if successful, could not only serve as an effective strategy to detect interactors, but also provide clues for potential co-factors involved in this interaction.

Briefly, two groups of immunoprecipitated samples, one is flag-tagged Beclin2 wild-type (Beclin2-WT), the other is flag-tagged Beclin2 69-88 deletion mutant (Beclin2-Δ69-88) that is reported to loss interaction with GASP1 (He et al., 2013), were subjected to SDS-PAGE analysis. The lanes of the resulting SDS-PAGE gel were excised as indicated in Figure 6.7, and then subjected to reduction, alkylation and trypsin digestion as instructed by the protocol (Shevchenko et al., 2006). Subsequently, mass spectrometry was applied to search for the digested peptides and the corresponding interacting proteins.

The mass spectrometry analysis results show almost identical profiles for the wild type Beclin2 and the Beclin2- Δ 69-88 deletion mutant. No individual

chromatographic peak is presented here owing to the large number of eluting peptides. Briefly, several Beclin2 binding partners, direct or indirect, were identified, for example, Ambra1, Vps34, Vps15, and Atg14L. However, GASP1 was not detected in the context of the assay used, nor any GASP1-associated proteins.

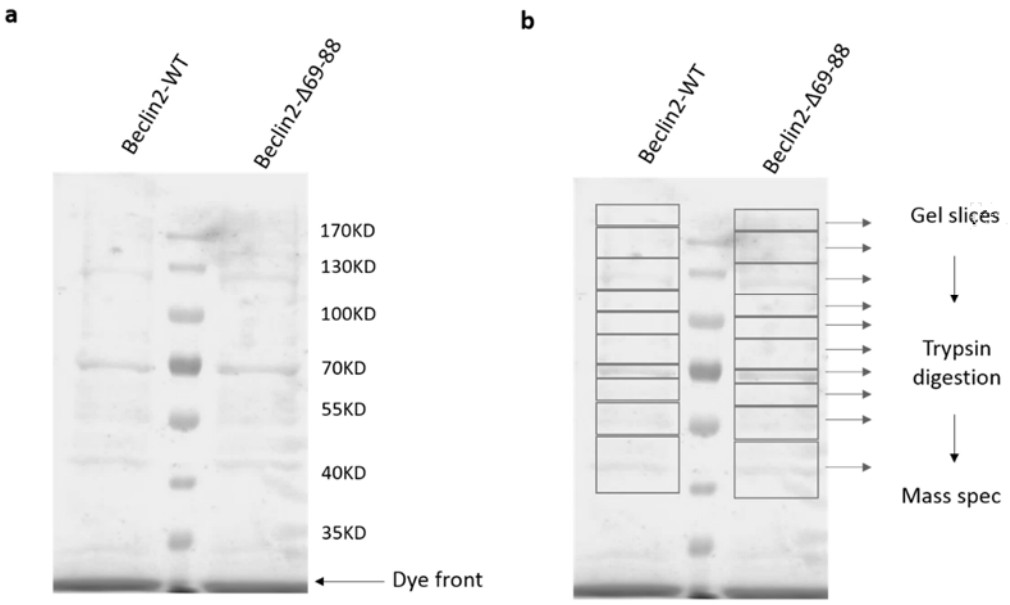

Figure 6.7 Coomassie-stained polyacrylamide gel of flag-Beclin2 wild type or flag-Beclin2-Δ69-88 deletion mutant immunoprecipitated samples. a, The Coomassie-stained gel of immunoprecipitated samples. **b**, The Coomassie-stained gel was sliced into ten lanes as labelled. A total of 20 lanes (each with 10 lanes) were excised for in-gel digestion and then analyzed by Orbitrap mass spectrometry.

6.2.5 Functional roles of Beclin2 in GPCR degradation

Even though the Beclin2-GASP1 interaction is not yet clarified, we indeed

observed a functional role of Beclin2 N-terminus in regulating GPCRs endosomal sorting via biotin-protection degradation assay. This assay has been proved as an effective approach to track the agonist-induces internalization and lysosomal degradation of GPCRs (He et al., 2013; Tschische et al., 2010). Specifically, HEK293 cells stably expressing Flag-D2R, termed as HEK-D2R cells hereafter, were transfected with siRNA Beclin2 to knockdown endogenous Beclin2 expression, followed by transfection of various Beclin2 non-targetable mutants (NTm) that are siRNA resistant to rescue Beclin2 expression. Of note, neither △69-88 nor I80S mutants would interact with GASP1 as reported previously (He et al., 2013). Then cells transfected with indicated plasmids were subjected to biotin-protection degradation assays respectively as described in methodology.

As shown in Figure 6.8, the flag-D2R degradation was blocked in the “control” group, where no rescue plasmid was transfected after Beclin2 knockdown, while restoring wild-type Beclin2 expression could reverse this blocking effect, with plenty of flag-D2R was degraded after dopamine treatment for 30 minutes. However, the GASP1 interaction abolished mutants △69-88 and I80S failed to do that at the same time point. These results suggest that Beclin2 is essential for dopamine-induced D2R endosomal trafficking and subsequent lysosomal degradation, and such function is depended on Beclin2-GASP1 interaction.

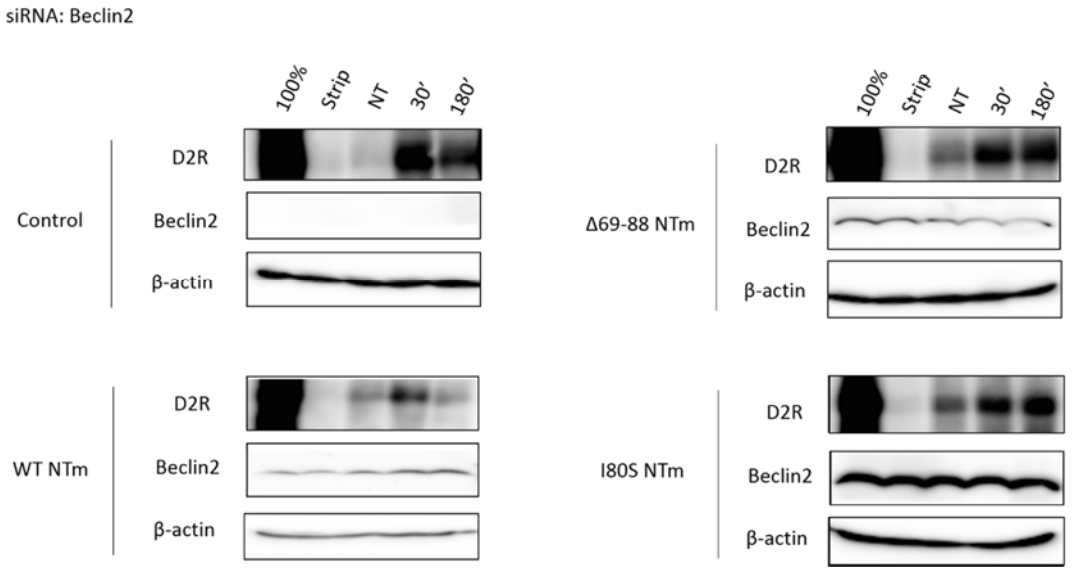

Figure 6.8 Effects of indicated Beclin2 NTm plasmids transfection on biotin-mediated protection of flag-D2R after siRNA knockdown endogenous Beclin2 in HEK-D2R cells. "100%" represents total biotinylated GPCR prior to cell-surface biotin stripping; "Strip" represents the remaining biotinylated GPCR after cell-surface stripping; "NT" represents the level of internalized biotinylated receptor with vehicle treatment after stripping; "30', 180'" represent levels of internalized biotinylated receptor with agonist treatment for 30 min or 180 min, respectively, after stripping. "Control" group: no rescue plasmid was transfected after siRNA Beclin2. "WT": wild-type.

Collectively, efforts to evaluate the association of Beclin2 N-terminal fragment and GASP1 AR failed to observe the direct interaction *in vitro*. Given the positive result in yeast two-hybrid and co-IP assays(He et al., 2013), whether special mechanisms, or additional protein co-factors are required to facilitate this Beclin2-GASP1 assembly remains to be investigate. Nevertheless, the Beclin2 mutation

constructs that abolished the Beclin2-GASP1 interaction exert negative regulation in D2R degradation, suggesting a role of Beclin2 in GPCR degradation through interacting with GASP1. Further work is required to investigate the underlying molecular machinery of Beclin2-GASP1 interaction.

6.2.6 Designed stapled peptides enhance endolysosomal degradation of GPCR

Using the structural findings of Beclin1 coiled coil domain as guidance, we conducted mechanism-based rational design to obtain a series of chemically modified peptides that can serve as potent modulators of autophagy (partially listed in Table 6.1). These peptides mimic residues 191-205 of Beclin1 (N-terminal of CC domain), thus would interacts with the corresponding C terminal part of Beclin1 CC domain (residues 231-245) according to its anti-parallel packing pattern. Furthermore, the targeted binding region (residues 231-245) of these peptides would not interfere the Beclin1- Atg14L/UVRAG interaction, because we already clarified that the Atg14L/UVRAG interacting regions are mainly located on the N-terminal part of Beclin1 CC (residues 174-223). On the contrary, the interactions between these peptides and Beclin1 are expected to disrupt the metastable dimerization of Beclin1 CC, render it monomeric, and facilitate the interaction of Beclin1 and Atg14L/UVRAG.

Table 6.1 Summary of the designed stapled peptides.

	Sequence
Beclin1 (191-205)	RLIQELEDVEKNRKV
SP4	RLISEL(R8)DREKQR(S5)A
SP9	LLISEL(R8)DREKQR(S5)A
SP12	LLISQL(R8)DREKQR(S5)A

Considering the structure nature of Beclin1 CC domains, chemical hydrocarbon links were applied to mimic the helical secondary structure. This kind of hydrocarbon link intends to “staple” amino acids together to stabilize their α-helical structure, and multiple studies have reported hydrocarbon stapled peptide as an effective approach to modulate protein-protein interactions (Cromm et al., 2015; Walensky and Bird, 2014). Specifically, the hydrocarbon staple of 13-carbon length was added to link residues 197 and 204 (Figure 6.9).

After computational screening, the stapled peptide SP4 with higher potential to interact with Beclin1 were selected for chemical synthesis, and the computational model illustrating the binding mode of SP4 and Beclin1 is showed in Figure 6.9. In addition, the Tat sequence (GRKKRRQRRRPQ) was added at the N-terminal to

enhance solubility and improve cell penetration capacity. Actually, a manuscript reporting the biological efficacy of Tat-SP4 in Beclin1 homodimerization and autophagy modulation is currently in preparation for submission. In this thesis, we mainly focus on its potency in promoting endolysosomal sorting of GPCR. Interestingly, although no cross-association between Beclin1 and Belcin2 was observed as described previously, the peptide which mimic the defined Beclin1 fragment would also interacts with Beclin2 as determined by ITC assay. As shown in Figure 6.10, Tat-SC4, a peptide with scrambled sequence of Tat-SP4, acts as the control here, does not interact with Beclin2. Tat-SP4 binds with Beclin2 CC directly in an exothermic manner, with the K_d value of 4.8 μM.

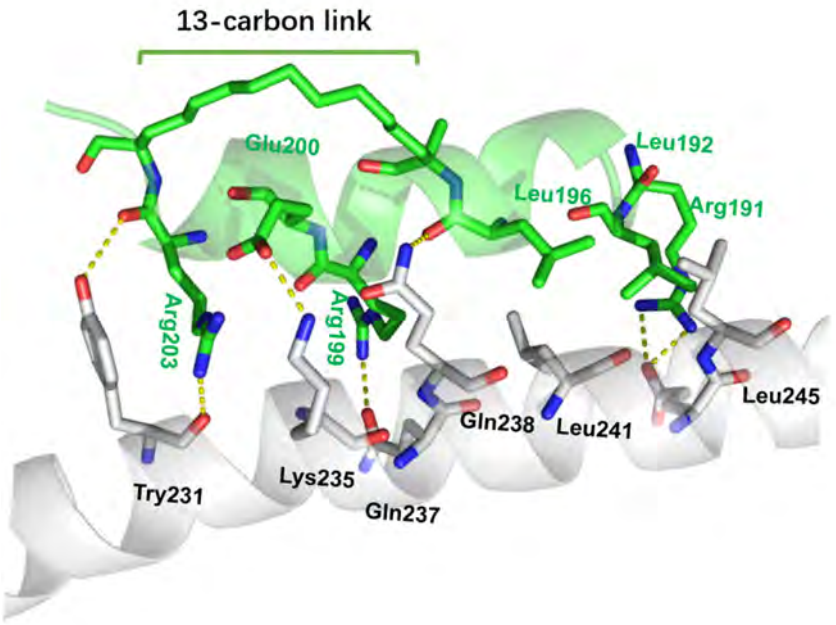

Figure 6.9 The computational model of SP4 binding to Beclin1. The 13-carbon length hydrocarbon link bridging residues R197 (8-carbon) and S204 (5-carbon) is labelled as indicated.

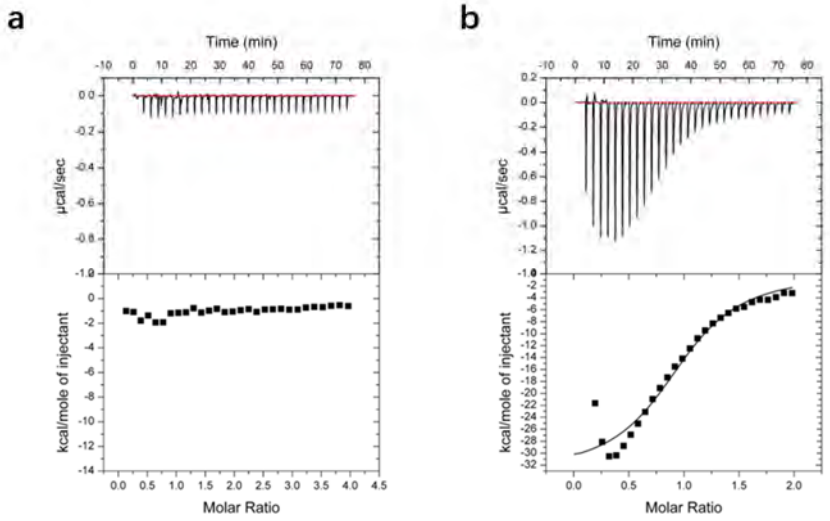

Figure 6.10 Determination of the interaction between Tat-SP4 and Beclin2 CC. **a & b**, ITC profiles of Tat-SC4 and Tat-SP4 titrated Beclin2 CC.

Competitive co-IP experiments were then performed to assess the impact of the stapled peptide on Beclin2 homodimerization. 20 µM Tat-SC4 or Tat-SP4 was applied to Hela cells one hour before co-transfection of flag-Beclin2 and myc-Beclin2 plasmids. Our results indicate that in presence of Tat-SP4, the self-association of Beclin2 was impeded. For Tat-SC4 control, it pulled down similar amount of myc-Beclin2 in comparison with the non-treated sample (Figure 6.11). We then further investigate the efficacy of Tat-SP4 in promoting endolysosomal trafficking of D2R using biotin-protection degradation assay. In HEK-D2R cells, Tat-SP4 accelerates the degradation of D2R at 150 minutes upon dopamine treatment, in contrast, Tat-SC4 induces no change in D2R degradation at the same concentration (Figure 6.12).

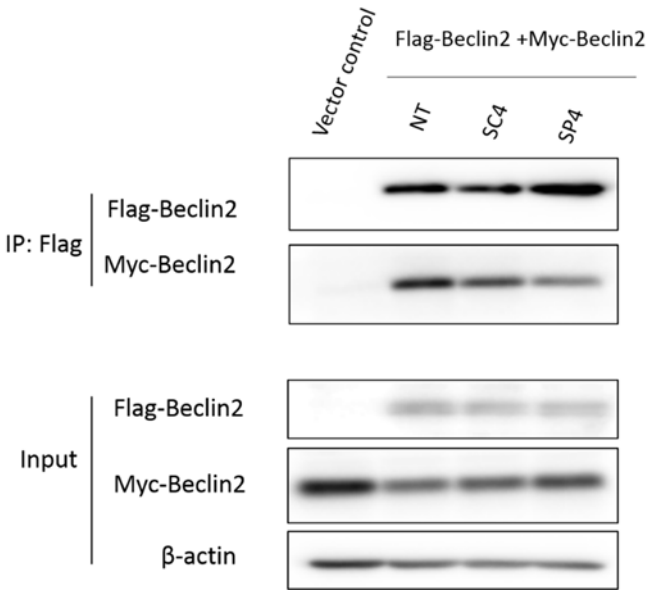

Figure 6.11 Co-immunoprecipitation and immunoblot analysis of Beclin2 self-association. NT: non-treated; SC4 and SP4: treated with 20 μM Tat-SC4 or Tat-SP4 before transfection, respectively.

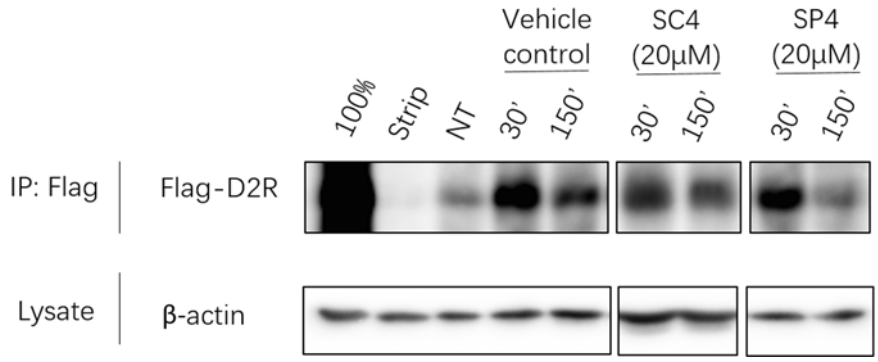

Figure 6.12 Effects of the indicated peptides on flag-D2R degradation in HEK-D2R cells. "Ctrl" group: vehicle control treatment. "30', 150'" represent levels of internalized biotinylated receptor with agonist treatment for 30 min or 150 min, respectively, after stripping.

Inspired by the result of Tat-SP4 in stimulating D2R degradation, two other stapled peptides, SP9 and SP12, were selected for chemical synthesis after computational screening. Likewise, Tat-SP9 and Tat-SP12 interact with Beclin2 CC in

an exothermic manner, with K_d values of 6.8 μM and 4.6 μM, comparable to that of Tat-SP4 (Figure 6.13). Strikingly, Tat-SP9 and Tat-SP12 fail to interact with Beclin1 CC as stated in the manuscript (to be submitted).

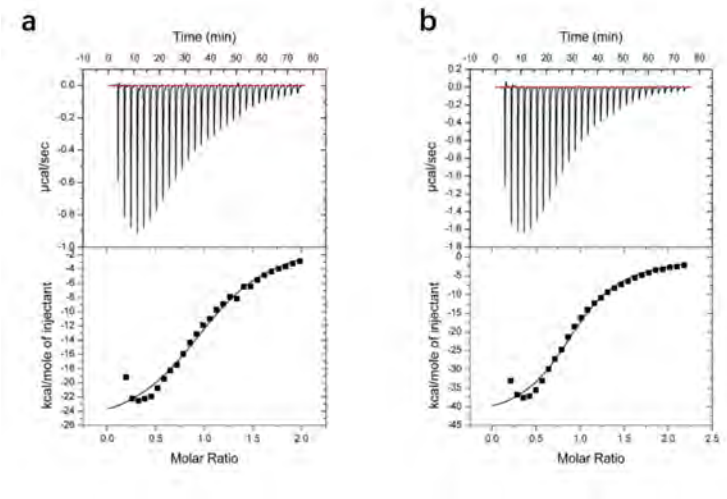

Figure 6.13 Determination of the interaction between stapled peptides and Beclin2 CC. a & b, ITC profiles of Tat-SP9 and Tat-SP12 titrated Beclin2 CC.

The potency of these two peptides on D2R degradation were then examined via biotin-protection degradation assay. The D2R degradation was robustly enhanced in the presence of Tat-SP12, while such enhancement was not observed for Tat-SP9 at the same concentration (Figure 6.14). To further evaluate the efficacy of stapled peptides in promoting D2R degradation, various concentrations of peptides, 10 μM, 20 μM and 40 μM, were applied in the assays. The results suggest that Tat-SP12 stimulates D2R degradation in a concentration dependent manner (Figure 6.15 a&b), however, Tat-SP9 induces no change in D2R degradation even at the concentration

of 40 μM (Figure 6.15a).

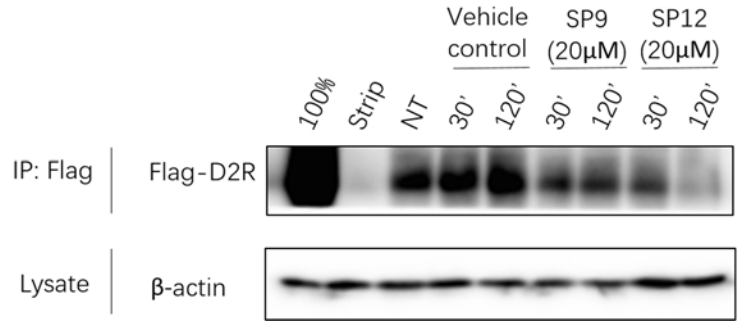

Figure 6.14 Effects of the indicated peptides on flag-D2R degradation in HEK-D2R cells. "Ctrl" group: vehicle control treatment. "30', 120'" represent levels of internalized biotinylated receptor with agonist treatment for 30 min or 120 min, respectively, after stripping.

a

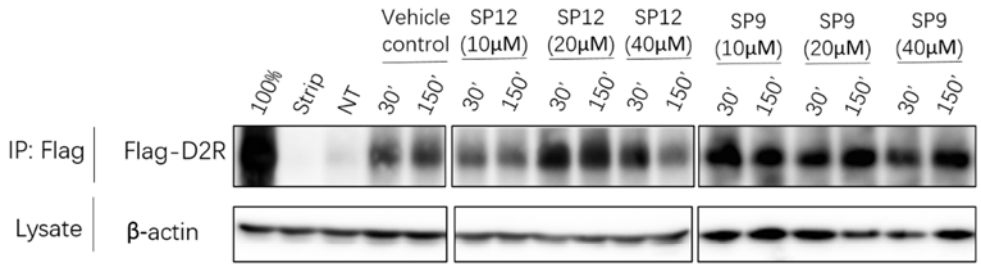

b

	Ctrl	SP12 (10 μM)	SP12 (20 μM)	SP12 (40 μM)
D2R/β-actin(150') / D2R/β-actin(30')	1.09	1.02	0.87	0.57

Figure 6.15 Effects of the indicated peptides with different concentration on flag-D2R degradation in HEK-D2R cells. "Ctrl" group: vehicle control treatment. **a**, Tat-SP12 stimulates D2R degradation in a concentration dependent manner. **b**, Quantification of the ratio of D2R levels at 150 min versus 30 min in each concentration of Tat-SP12.

In summary, these data suggest that the rationally designed peptides are potent Beclin2 interactors. Among which, Tat-SP4 and Tat-SP12 are promising inducers in endolysosomal sorting of GASP1-associated GPCRs such as D2R. These exciting results imply that Beclin2-targeting peptides may have the potential to serve as therapeutic agents for diseases that can benefit from faster GPCR internalization such as metabolic disorders and schizophrenia.

Chapter Seven: Discussion and Future Studies

Using a combination of biochemical, structural and molecular biology methods, we have obtained significant amount of results to help delineate the functional role of Beclin2 in autophagy and GPCR trafficking.

For the first objective to assess the biochemical and structural differences between Beclin1 and Beclin2, we conducted a series of ITC experiments to characterize the binding affinities of Beclin2 to Atg14L and UVRAG. We also used competitive ITC assays to compare Beclin2 and Beclin1 in terms of binding affinity to Atg14L and UVRAG. Interestingly, our results show that Beclin2 binds to Atg14L with stronger affinity while Beclin1 preferentially binds to UVRAG. The functional significance of such differences is not clear.

We also determined the structure of the Beclin2 CC domain and compared it carefully with that for Beclin1 CC domain. Similar to Beclin1, Beclin2 CC domain forms an anti-parallel metastable homodimer. While a few canonical hydrophobic a-d' pairings at the CC interface serve to stabilize the dimer assembly, multiple "imperfect" a-d' pairings with polar or charged residues render it only metastable. While the Beclin1 and Beclin2 structures are highly similar, our detailed structural analysis reveals that small yet distinct sequence differences at the CC interface. On one hand, such difference leads to one fewer canonical hydrophobic a-d' pairing at the Beclin2

homodimer interface as compared to Beclin1 and renders Beclin2 homodimer less stable than Beclin1. On the other hand, such differences also ensure that Beclin1 and Beclin2 cannot cross-associate as confirmed by our *in vivo* co-IP experiments. Thus, Beclin1 and Beclin2 CC domains are biochemically and structurally distinct despite over 50% sequence identity.

Furthermore, using the structure of the Beclin1-UVRAG CC complex solved by our lab as template, we generated a model of the Beclin2-UVRAG complex. This model confirms that sequence complementarity between Beclin2 and UVRAG renders the heterodimeric Beclin2-UVRAG complex more stable than Beclin2 homodimer. Thus the “imperfect” feature of Beclin2 CC domain is necessary to enable its interaction with UVRAG so that the UVRAG-containing Beclin2-Vps34 complex can be readily formed to mediate autophagy. Furthermore, our model reveals that the Beclin2-UVRAG CC interface has one fewer electrostatically favorable interaction in comparison with that of Beclin1-UVRAG, likely accounting for less sensitivity of Beclin2-UVRAG interaction to high salt conditions.

Additionally, we also conducted biochemical and structural studies of the Beclin2-Atg14L interaction. So far, no structural information is available for Atg14L CC domain. It is not clear how Atg14L interacts with Beclin1 or Beclin2 to form the Atg14L-containing Beclin1/Beclin2-Vps34 complex to promote autophagy. Toward this goal, we first conducted extensive biochemical mapping to identify the most

critical region within Beclin2 and Atg14L that would be responsible for their interaction. Our results show that, similar to the Beclin1-UVRAG CC complex, the N-terminal region of Beclin2 and Atg14L CC domains are the most critical sites. Following this lead, we carried out extensive crystallization trials and construct optimization. Finally, we managed to obtain crystals of diffraction quality with resolution to 2.5 Å, and finally solve the structure by *ab initio* phasing using "Arcimbodol lite" program. This structure, to our knowledge, is the first piece of atomic structural information for Atg14L.

The structure of Beclin2-Atg14L complex reveals a parallel coiled coil heterodimer. In comparison with Beclin2 homodimer, this heterodimer retains the perfect hydrophobic pairings and gains additional stabilizing interactions at the interface. For example, Beclin2 residue E173 poses the destabilizing effect in Beclin2 homodimer because of its charged side chain. In Beclin2-Atg14L complex, however, this residue form electrostatically favorable interaction with Atg14L residue R119. Such sequence complementarity converts imperfect destabilizing factors into favorable stabilizing elements, rendering Beclin2-Atg14L interaction notably stable.

Based on the structural models obtained, we not only delineate molecular determinants that enable the strong interactions of Beclin2 and Atg14L/UVARG, but also reveal the molecular mechanism by which Atg14L and UVRAG bind to Beclin2 as competitors in mutually exclusive manner.

For the second objective of identifying the molecular determinants that enable GASP1's specific binding to Beclin2, we have focused on the C-terminal armadillo repeats (AR) domain of GASP1 and the N-terminal region of Beclin2. Both these regions have been shown to be responsible for their association by previous co-IP results. We purified recombinant protein for the GASP1 AR domain and Beclin2 N-terminal region. However, no direct interaction can be detected between these two by either ITC or pull-down studies. In addition, we used peptide arrays to scan for short GASP1-binding motifs within the Beclin2 N-terminal region but failed to identify any leads. Lastly, we used mass spectrometry based proteomics approach to look for binding partners for Beclin2 N-terminal region, with the possibility that the interaction between GASP1 and Beclin2 may require a third protein as mediator. However, our preliminary data so far didn't reveal any new binding partners to Beclin2 N-terminal region. In fact, even GASP1 was not readily identified.

For the third objective of designing peptide mimetics to target Beclin2 and modulate GPCR signaling, this is to continue our lab's standing interest in structure-based rational design of autophagy modulators as therapeutic agents for autophagy-related diseases like cancer, diabetes and neurodegeneration. In our previous work, we designed a Beclin1-specific stapled peptide that can bind to the C-terminal part of the Beclin1 CC domain outside of the UVRAG binding site. As a result, such a peptide can disrupt the functionally inactive Beclin1 homodimer, promote the

Beclin1-UVRAG interaction and enhance the abundance of the UVRAG-containing Beclin1-Vps34 complex.

In my thesis we applied this design idea to Beclin2. A series of stapled peptides have been designed and synthesized following the same principle. Their binding affinity to Beclin2 CC domain has been confirmed by ITC experiments. For the stapled peptide with the strongest binding affinity to Beclin2, we carried out co-IP experiments to confirm that it can reduce the self-association of Beclin2 *in vivo*. Additionally, we carried out GPCR internalization assay to demonstrate that this peptide can indeed promote the internalization influx of GASP1-associated GPCRs such as D2R. These exciting results imply that Beclin2-targeting peptides may have the potential to serve as therapeutic agents for diseases that can benefit from faster GPCR internalization such as metabolic disorders and schizophrenia.

For future work, the following aspects are worth for further exploration.

For the first objective of biochemical and structural study of the Beclin2 CC domain, we intend to conduct structure-based functional studies to test how mutational perturbation of Beclin2-Atg14L interaction would compromise its competitional advantage over UVRAG, and the related functional alterations, especially in terms of autophagy. Such studies will provide new insight into the functional significance of the stronger interaction of Beclin2-Atg14L in comparison of

Beclin2-UVRAG, and help us gain an understanding of how Beclin2 regulate autophagy distinctly from Beclin1.

For the second objective of delineating the molecular mechanism of the GASP1-Beclin2 interaction, our results so far fail to confirm direct physical interaction between GASP1 and Beclin2. Our preliminary proteomics studies also couldn't validate GASP1 in the precipitated lysate pulled down by Beclin2. These preliminary results raise concern that Beclin2 and GASP1 may not directly interact each other as previously suggested. For future studies we plan to first repeat the co-IP experiments as described in previous publications to confirm Beclin2-GASP1 association. Once we have positive results, we will then use mass spectrometry method to identify all proteins in the co-IP lysate to search for additional proteins that might facilitate the Beclin2-GASP1 interaction. If candidates can be identified, we will then use siRNA method to temporarily knockdown these candidates and assess how the Beclin2-GASP1 interaction can be affected. If indeed we can identify additional candidates we will then proceed to carry out biochemical and possible structural studies of all proteins involved, including Beclin2, GASP1 and the candidates we identify. Understanding the Beclin2-GASP1 interaction at molecular and atomic levels will greatly enhance our knowledge about GASP1-assocaited GPCR signaling.

Lastly for the third objective of designing Beclin2-specific peptides to enhance GPCR internalization, our future work is to further optimize the potency and

specificity of the designed peptides in terms of Beclin2 binding so that its effect in modulating GPCR internalization can be enhanced. For this goal we will go through iterative cycles of computational design, chemical synthesis, *in vitro* screening and *in vivo* functional characterization, with the *in vitro* and *in vivo* data serving as feedback for computational optimization. For especially promising peptides, we envision to eventually carry out animal-based studies to validate their efficacy.

In summary, my thesis work has focused on biochemical and structural studies of Beclin2. By focusing on its coiled coil domain and N-terminal region, we have gained significant amount of data that offer further insight into the functional distinction between Beclin2 and its homolog Beclin1 in modulating autophagy. In addition, our designed Beclin2-targeting peptides show positive effect in stimulating agonist-induced GPCR trafficking, which may hold therapeutic potential for certain GPCR-related diseases.

Reference

Abu-Helo, A., and Simonin, F. (2010). Identification and biological significance of G protein-coupled receptor associated sorting proteins (GASPs). Pharmacology & therapeutics *126*, 244-250.

Adams, P.D., Grosse-Kunstleve, R.W., Hung, L.W., Ioerger, T.R., McCoy, A.J., Moriarty, N.W., Read, R.J., Sacchettini, J.C., Sauter, N.K., and Terwilliger, T.C. (2002). PHENIX: building new software for automated crystallographic structure determination. Acta Crystallogr D Biol Crystallogr *58*, 1948-1954.

Aebersold, R., and Mann, M. (2003). Mass spectrometry-based proteomics. Nature *422*, 198-207.

Aissani, B., Perusse, L., Lapointe, G., Chagnon, Y.C., Bouchard, L., Walts, B., and Bouchard, C. (2006). A quantitative trait locus for body fat on chromosome 1q43 in French Canadians: Linkage and association studies. Obesity *14*, 1605-1615.

Aissani, B., Wiener, H., and Zhang, K. (2013). Multiple Hits for the Association of Uterine Fibroids on Human Chromosome 1q43. Plos One *8*.

Antonioli, M., Di Rienzo, M., Piacentini, M., and Fimia, G.M. (2017). Emerging Mechanisms in Initiating and Terminating Autophagy. Trends Biochem Sci *42*, 28-41.

Aslanidis, C., and Dejong, P.J. (1990). Ligation-Independent Cloning of Pcr Products (Lic-Pcr). Nucleic Acids Res *18*, 6069-6074.

Bartlett, S.E., Enquist, J., Hopf, F.W., Lee, J.H., Gladher, F., Kharazia, V., Waldhoer, M., Mailliard, W.S., Armstrong, R., Bonci, A.*, et al.* (2005). Dopamine responsiveness is regulated by targeted sorting of D2 receptors. P Natl Acad Sci USA *102*, 11521-11526.

Baskaran, S., Carlson, L.A., Stjepanovic, G., Young, L.N., Kim, D.J., Grob, P., Stanley, R.E., Nogales, E., and Hurley, J.H. (2014). Architecture and Dynamics of the Autophagic Phosphatidylinositol 3-Kinase Complex. Elife *3*.

Battye, T.G.G., Kontogiannis, L., Johnson, O., Powell, H.R., and Leslie, A.G.W. (2011). iMOSFLM: a new graphical interface for diffraction-image processing with MOSFLM. Acta Crystallogr D *67*, 271-281.

Behrends, C., Sowa, M.E., Gygi, S.P., and Harper, J.W. (2010). Network organization of the human autophagy system. Nature *466*, 68-76.

Bordoli, L., Kiefer, F., Arnold, K., Benkert, P., Battey, J., and Schwede, T. (2009). Protein structure homology modeling using SWISS-MODEL workspace. Nat Protoc *4*, 1-13.

Chen, X., Zaro, J.L., and Shen, W.C. (2013). Fusion protein linkers: property, design and functionality. Adv Drug Deliv Rev *65*, 1357-1369.

Cheng, X.W., Ma, X.L., Ding, X.M., Li, L., Jiang, X., Shen, Z.R., Chen, S., Liu, W., Gong, W.H., and Sun, Q.M. (2017). Pacer Mediates the Function of Class III PI3K and HOPS Complexes in Autophagosome Maturation by Engaging Stx17. Mol Cell *65*, 1029-+.

Choi, A.M., Ryter, S.W., and Levine, B. (2013). Autophagy in human health and disease. N Engl J Med *368*, 1845-1846.

Chude, C.I., and Amaravadi, R.K. (2017). Targeting Autophagy in Cancer: Update on Clinical Trials and Novel Inhibitors. Int J Mol Sci *18*.

Collaborative Computational Project, N. (1994). The CCP4 suite: programs for protein crystallography. Acta Crystallogr D Biol Crystallogr *50*, 760-763.

Cromm, P.M., Spiegel, J., and Grossmann, T.N. (2015). Hydrocarbon Stapled Peptides

as Modulators of Biological Function. Acs Chem Biol *10*, 1362-1375.

Decuypere, J.P., Parys, J.B., and Bultynck, G. (2012). Regulation of the autophagic bcl-2/beclin 1 interaction. Cells *1*, 284-312.

Diao, J., Liu, R., Rong, Y., Zhao, M., Zhang, J., Lai, Y., Zhou, Q., Wilz, L.M., Li, J., Vivona, S*., et al.* (2015). ATG14 promotes membrane tethering and fusion of autophagosomes to endolysosomes. Nature *520*, 563-566.

Dores, M.R., and Trejo, J. (2014). Atypical regulation of G protein-coupled receptor intracellular trafficking by ubiquitination. Curr Opin Cell Biol *27*, 44-50.

Drozdetskiy, A., Cole, C., Procter, J., and Barton, G.J. (2015). JPred4: a protein secondary structure prediction server. Nucleic Acids Res *43*, W389-W394.

Eglen, R.M., Bosse, R., and Reisine, T. (2007). Emerging concepts of guanine nucleotide-binding protein-coupled receptor (GPCR) function and implications for high throughput screening. Assay and drug development technologies *5*, 425-451.

Emsley, P., and Cowtan, K. (2004). Coot: model-building tools for molecular graphics. Acta Crystallogr D Biol Crystallogr *60*, 2126-2132.

Feng, Y.C., He, D., Yao, Z.Y., and Klionsky, D.J. (2014). The machinery of macroautophagy. Cell Res *24*, 24-41.

Fimia, G.M., Di Bartolomeo, S., Piacentini, M., and Cecconi, F. (2011). Unleashing the Ambra1-Beclin 1 complex from dynein chains Ulk1 sets Ambra1 free to induce autophagy. Autophagy *7*, 115-117.

Funderburk, S.F., Wang, Q.J., and Yue, Z.Y. (2010). The Beclin 1-VPS34 complex - at the crossroads of autophagy and beyond. Trends Cell Biol *20*, 355-362.

Galluzzi, L., Baehrecke, E.H., Ballabio, A., Boya, P., Pedro, J.M.B.S., Cecconi, F., Choi, A.M., Chu, C.T., Codogno, P., Colombo, M.I., *et al.* (2017). Molecular definitions of autophagy and related processes. Embo J *36*, 1811-1836.

Ge, L., Baskaran, S., Schekman, R., and Hurley, J.H. (2014). The protein-vesicle network of autophagy. Curr Opin Cell Biol *29*, 18-24.

Greenfield, N.J. (2006). Using circular dichroism spectra to estimate protein secondary structure. Nat Protoc *1*, 2876-2890.

Grigoryan, G., and Keating, A.E. (2008). Structural specificity in coiled-coil interactions. Current opinion in structural biology *18*, 477-483.

Guo, B., Liang, Q., Li, L., Hu, Z., Wu, F., Zhang, P., Ma, Y., Zhao, B., Kovacs, A.L., Zhang, Z., *et al.* (2014). O-GlcNAc-modification of SNAP-29 regulates autophagosome maturation. Nat Cell Biol *16*, 1215-1226.

Hadley, E.B., Testa, O.D., Woolfson, D.N., and Gellman, S.H. (2008). Preferred side-chain constellations at antiparallel coiled-coil interfaces. Proc Natl Acad Sci U S A *105*, 530-535.

Haun, R.S., Serventi, I.M., and Moss, J. (1992). Rapid, Reliable Ligation-Independent Cloning of Pcr Products Using Modified Plasmid Vectors. Biotechniques *13*, 515-518.

He, C.C., and Levine, B. (2010). The Beclin 1 interactome. Curr Opin Cell Biol *22*, 140-149.

He, C.C., Wei, Y.J., Sun, K., Li, B.H., Dong, X.N., Zou, Z.J., Liu, Y., Kinch, L.N., Khan, S., Sinha, S., *et al.* (2013). Beclin 2 Functions in Autophagy, Degradation of G Protein-Coupled Receptors, and Metabolism. Cell *154*, 1085-1099.

Heydorn, A., Sondergaard, B.P., Ersboll, B., Holst, B., Nielsen, F.C., Haft, C.R., Whistler, J., and Schwartz, T.W. (2004). A library of 7TM receptor C-terminal tails. Interactions with the proposed post-endocytic sorting proteins ERM-binding phosphoprotein 50 (EBP50), N-ethylmaleimide-sensitive factor (NSF), sorting nexin 1 (SNX1), and G protein-coupled receptor-associated sorting protein (GASP). J Biol Chem *279*, 54291-54303.

Huang, W.J., Choi, W.Y., Hu, W.Q., Mi, N., Guo, Q., Ma, M.S., Liu, M., Tian, Y., Lu, P.L., Wang, F.L*., et al.* (2012). Crystal structure and biochemical analyses reveal Beclin 1 as a novel membrane binding protein. Cell Res *22*, 473-489.

Hurley, J.H., and Schulman, B.A. (2014). Atomistic autophagy: the structures of cellular self-digestion. Cell *157*, 300-311.

Itakura, E., Kishi-Itakura, C., and Mizushima, N. (2012). The hairpin-type tail-anchored SNARE syntaxin 17 targets to autophagosomes for fusion with endosomes/lysosomes. Cell *151*, 1256-1269.

Itakura, E., Kishi, C., Inoue, K., and Mizushima, N. (2008). Beclin 1 Forms Two Distinct Phosphatidylinositol 3-Kinase Complexes with Mammalian Atg14 and UVRAG. Mol Biol Cell *19*, 5360-5372.

Itakura, E., and Mizushima, N. (2009). Atg14 and UVRAG Mutually exclusive subunits of mammalian Beclin 1-PI3K complexes. Autophagy *5*, 534-536.

Itakura, E., and Mizushima, N. (2010). Characterization of autophagosome formation site by a hierarchical analysis of mammalian Atg proteins. Autophagy *6*, 764-776.

Johnson, W.C. (1988). Secondary Structure of Proteins through Circular-Dichroism Spectroscopy. Annu Rev Biophys Bio *17*, 145-166.

Karanasios, E., Stapleton, E., Manifava, M., Kaizuka, T., Mizushima, N., Walker, S.A., and Ktistakis, N.T. (2013). Dynamic association of the ULK1 complex with omegasomes during autophagy induction. J Cell Sci *126*, 5224-5238.

Levine, B., and Kroemer, G. (2008). Autophagy in the pathogenesis of disease. Cell *132*, 27-42.

Li, X., He, L., Che, K.H., Funderburk, S.F., Pan, L., Pan, N., Zhang, M., Yue, Z., and Zhao, Y. (2012). Imperfect interface of Beclin1 coiled-coil domain regulates homodimer and heterodimer formation with Atg14L and UVRAG. Nature communications *3*, 662.

Liang, C., Lee, J.S., Inn, K.S., Gack, M.U., Li, Q., Roberts, E.A., Vergne, I., Deretic, V., Feng, P., Akazawa, C.*, et al.* (2008). Beclin1-binding UVRAG targets the class C Vps complex to coordinate autophagosome maturation and endocytic trafficking. Nat Cell Biol *10*, 776-787.

Liang, X.H., Jackson, S., Seaman, M., Brown, K., Kempkes, B., Hibshoosh, H., and Levine, B. (1999). Induction of autophagy and inhibition of tumorigenesis by beclin 1. Nature *402*, 672-676.

Liang, X.H., Kleeman, L.K., Jiang, H.H., Gordon, G., Goldman, J.E., Berry, G., Herman, B., and Levine, B. (1998). Protection against fatal Sindbis virus encephalitis by Beclin, a novel Bcl-2-interacting protein. J Virol *72*, 8586-8596.

Maiuri, M.C., Criollo, A., Tasdemir, E., Vicencio, J.M., Tajeddine, N., Hickman, J.A., Geneste, O., and Kroemer, G. (2007). BH3-only proteins and BH3 mimetics induce autophagy by competitively disrupting the interaction between Beclin 1 and Bcl-2/Bcl-X-L. Autophagy *3*, 374-376.

Manic, G., Obrist, F., Kroemer, G., Vitale, I., and Galluzzi, L. (2014). Chloroquine and

hydroxychloroquine for cancer therapy. Mol Cell Oncol *1*, e29911.

Marchese, A., Paing, M.M., Temple, B.R.S., and Trejo, J. (2008). G protein-coupled receptor sorting to endosomes and lysosomes. Annu Rev Pharmacol *48*, 601-629.

Martini, L., Waldhoer, M., Pusch, M., Kharazia, V., Fong, J., Lee, J.H., Freissmuth, C., and Whistler, J.L. (2007). Ligand-induced down-regulation of the cannabinoid 1 receptor is mediated by the G-protein-coupled receptor-associated sorting protein GASP1. Faseb J *21*, 802-811.

Matsunaga, K., Morita, E., Saitoh, T., Akira, S., Ktistakis, N.T., Izumi, T., Noda, T., and Yoshimori, T. (2010). Autophagy requires endoplasmic reticulum targeting of the PI3-kinase complex via Atg14L. J Cell Biol *190*, 511-521.

Matsunaga, K., Saitoh, T., Tabata, K., Omori, H., Satoh, T., Kurotori, N., Maejima, I., Shirahama-Noda, K., Ichimura, T., Isobe, T*., et al.* (2009). Two Beclin 1-binding proteins, Atg14L and Rubicon, reciprocally regulate autophagy at different stages. Nat Cell Biol *11*, 385-U369.

Mei, Y., Su, M., Sanishvili, R., Chakravarthy, S., Colbert, C.L., and Sinha, S.C. (2016). Identification of BECN1 and ATG14 Coiled-Coil Interface Residues That Are Important for Starvation-Induced Autophagy. Biochemistry *55*, 4239-4253.

Mizushima, N., and Komatsu, M. (2011). Autophagy: Renovation of Cells and Tissues. Cell *147*, 728-741.

Mizushima, N., Yoshimori, T., and Ohsumi, Y. (2011). The role of Atg proteins in autophagosome formation. Annu Rev Cell Dev Biol *27*, 107-132.

Morris, D.H., Yip, C.K., Shi, Y., Chait, B.T., and Wang, Q.J. (2015). Beclin 1-Vps34

Complex Architecture: Understanding the Nuts and Bolts of Therapeutic Targets. Front Biol (Beijing) *10*, 398-426.

Noda, T., Matsunaga, K., and Yoshimori, T. (2011). Atg14L recruits PtdIns 3-kinase to the ER for autophagosome formation. Autophagy *7*, 438-439.

Obara, K., and Ohsumi, Y. (2011). Atg14: a key player in orchestrating autophagy. International journal of cell biology *2011*, 713435.

Obara, K., Sekito, T., and Ohsumi, Y. (2006). Assortment of phosphatidylinositol 3-kinase complexes-Atg14p directs association of complex I to the pre-autophagosomal structure in Saccharomyces cerevisiae. Mol Biol Cell *17*, 1527-1539.

Ohsumi, Y. (2014). Historical landmarks of autophagy research. Cell Res *24*, 9-23.

Parmeggiani, F., Pellarin, R., Larsen, A.P., Varadamsetty, G., Stumpp, M.T., Zerbe, O., Caflisch, A., and Pluckthun, A. (2008). Designed armadillo repeat proteins as general peptide-binding scaffolds: Consensus design and computational optimization of the hydrophobic core. J Mol Biol *376*, 1282-1304.

Petibone, D.M., Majeed, W., and Casciano, D.A. (2017). Autophagy function and its relationship to pathology, clinical applications, drug metabolism and toxicity. J Appl Toxicol *37*, 23-37.

Pierce, M.M., Raman, C.S., and Nall, B.T. (1999). Isothermal titration calorimetry of protein-protein interactions. Methods *19*, 213-221.

Rodriguez, D.D., Grosse, C., Himmel, S., Gonzalez, C., de Ilarduya, I.M., Becker, S., Sheldrick, G.M., and Uson, I. (2009). Crystallographic ab initio protein structure solution below atomic resolution. Nat Methods *6*, 651-U639.

Rostislavleva, K., Soler, N., Ohashi, Y., Zhang, L.F., Pardon, E., Burke, J.E., Masson, G.R., Johnson, C., Steyaert, J., Ktistakis, N.T*., et al.* (2015). Structure and flexibility of the endosomal Vps34 complex reveals the basis of its function on membranes. Science *350*.

Sammito, M., Millan, C., Rodriguez, D.D., de Ilarduya, I.M., Meindl, K., De Marino, I., Petrillo, G., Buey, R.M., de Pereda, J.M., Zeth, K*., et al.* (2013). Exploiting tertiary structure through local folds for crystallographic phasing. Nat Methods *10*, 1099-1101.

Sarkar, S., and Rubinsztein, D.C. (2008). Small molecule enhancers of autophagy for neurodegenerative diseases. Mol Biosyst *4*, 895-901.

Shevchenko, A., Tomas, H., Havlis, J., Olsen, J.V., and Mann, M. (2006). In-gel digestion for mass spectrometric characterization of proteins and proteomes. Nat Protoc *1*, 2856-2860.

Simonin, F., Karcher, P., Boeuf, J.J., Matifas, A., and Kieffer, B.L. (2004). Identification of a novel family of G protein-coupled receptor associated sorting proteins. Journal of neurochemistry *89*, 766-775.

Sinha, S., and Levine, B. (2008). The autophagy effector Beclin 1: a novel BH3-only protein. Oncogene *27 Suppl 1*, S137-148.

Slobodkin, M.R., and Elazar, Z. (2013). The Atg8 family: multifunctional ubiquitin-like key regulators of autophagy. Essays Biochem *55*, 51-64.

Sun, Q.M., Fan, W.L., Chen, K.L., Ding, X.J., Chen, S., and Zhong, Q. (2008). Identification of Barkor as a mammalian autophagy-specific factor for Beclin 1 and class III phosphatidylinositol 3-kinase. P Natl Acad Sci USA *105*, 19211-19216.

Sun, Q.M., Fan, W.L., and Zhong, Q. (2009). Regulation of Beclin 1 in autophagy. Autophagy *5*, 713-716.

Sun, Q.M., Westphal, W., Wong, K.N., Tan, I., and Zhong, Q. (2010). Rubicon controls endosome maturation as a Rab7 effector. P Natl Acad Sci USA *107*, 19338-19343.

Suzuki, K., and Ohsumi, Y. (2010). Current knowledge of the pre-autophagosomal structure (PAS). Febs Lett *584*, 1280-1286.

Terwilliger, T.C., Grosse-Kunstleve, R.W., Afonine, P.V., Moriarty, N.W., Zwart, P.H., Hung, L.W., Read, R.J., and Adams, P.D. (2008). Iterative model building, structure refinement and density modification with the PHENIX AutoBuild wizard. Acta Crystallogr D *64*, 61-69.

Thoresen, S.B., Pedersen, N.M., Liestol, K., and Stenmark, H. (2010). A phosphatidylinositol 3-kinase class III sub-complex containing VPS15, VPS34, Beclin 1, UVRAG and BIF-1 regulates cytokinesis and degradative endocytic traffic. Experimental cell research *316*, 3368-3378.

Tschische, P., Moser, E., Thompson, D., Vischer, H.F., Parzmair, G.P., Pommer, V., Platzer, W., Schwarzbraun, T., Schaider, H., Smit, M.J.*, et al.* (2010). The G-protein Coupled Receptor Associated Sorting Protein GASP-1 Regulates the Signalling and Trafficking of the Viral Chemokine Receptor US28. Traffic *11*, 660-674.

Velazquez-Campoy, A., Leavitt, S.A., and Freire, E. (2004a). Characterization of protein-protein interactions by isothermal titration calorimetry. Methods in molecular biology *261*, 35-54.

Velazquez-Campoy, A., Ohtaka, H., Nezami, A., Muzammil, S., and Freire, E. (2004b). Isothermal titration calorimetry. Current protocols in cell biology / editorial board,

Juan S Bonifacino [et al] *Chapter 17*, Unit 17 18.

Walensky, L.D., and Bird, G.H. (2014). Hydrocarbon-Stapled Peptides: Principles, Practice, and Progress. J Med Chem *57*, 6275-6288.

Wei, Y.J., Zou, Z.J., Becker, N., Anderson, M., Sumpter, R., Xiao, G.H., Kinch, L., Koduru, P., Christudass, C.S., Veltri, R.W.*, et al.* (2013). EGFR-Mediated Beclin 1 Phosphorylation in Autophagy Suppression, Tumor Progression, and Tumor Chemoresistance. Cell *154*, 1269-1284.

Whistler, J.L., Enquist, J., Marley, A., Fong, J., Gladher, F., Tsuruda, P., Murray, S.R., and von Zastro, M. (2002). Modulation of postendocytic sorting of G-protein coupled receptors. Science *297*, 615-620.

Yang, Z., and Klionsky, D.J. (2010). Eaten alive: a history of macroautophagy. Nat Cell Biol *12*, 814-822.

Zhang, W.R., and He, C.C. (2014). Regulation of plasma membrane receptors by a new autophagy-related BECN/Beclin family member. Autophagy *10*, 1472-1473.

Zhong, Y., Wang, Q.J., Li, X.T., Yan, Y., Backer, J.M., Chait, B.T., Heintz, N., and Yue, Z.Y. (2009). Distinct regulation of autophagic activity by Atg14L and Rubicon associated with Beclin 1-phosphatidylinositol-3-kinase complex. Nat Cell Biol *11*, 468-U262.